



FEI

Pizero and direct photon production at high transverse momenta

George Zioulas

Physics Department

McGill University, Montreal

November, 1990

A Thesis submitted to the Faculty of Graduate Studies and Research
in partial fulfillment of the requirements for the degree of
Doctor of Philosophy

© G. Zioulas, 1990

Abstract

The inclusive pizero and direct photon productions by 300 GeV/c π^- and π^+ beams on a lithium target, were measured using the E705 spectrometer at Fermilab. The cross sections were determined by analyzing a fraction (20%) of the data recorded by the experiment during the 1987-1988 running period. The photons were measured by a high resolution electromagnetic calorimeter which consisted of scintillation and lead glass blocks. A fast trigger was designed and implemented to select events with high transverse energy depositions in the calorimeter.

The invariant cross sections are presented as a function of the transverse momentum and the Feynman-x in the range between 4 to 7 GeV/c and -0.25 to 0.35 respectively. The results are compared to the measurements made by other experiments and to theoretical predictions within the framework of Quantum ChromoDynamics.

FERMILAB

FEB 14 1989

LIBRARY

Sommaire

La production inclusive de pizero et de photons directs par un faisceau de π^- et π^+ incident à 300 GeV/c sur une cible de lithium a été mesurée utilisant le spectromètre de l'expérience E705 à Fermilab. Les sections efficaces ont été déterminées par l'analyse d'une portion (20%) des événements enregistrés par l'expérience au cours des années 1987-1988. Les photons ont été mesurés par un calorimètre électromagnétique composé de blocs de verre au plomb et de verre scintillant. Pour sélectionner les événements qui déposaient une grande quantité d'énergie transverse dans le calorimètre, un système de déclenchement rapide a été mis en fonction.

Les sections efficaces sont présentées en fonction de l'impulsion transverse et de la variable x de Feynman dans l'intervalle 4 à 7 GeV/c et -0.25 à 0.35 respectivement. Les résultats obtenus sont comparés avec les distributions obtenues par les autres expériences et avec les prédictions théoriques dans le cadre de la théorie ChromoDynamique Quantique.

Original Material

My principal contributions to the accomplishment of the E705 experiment, in chronological order were:

- Participated in the chamber construction. Tested and applied the electrolysis technique to deactivate the central regions of the proportional and drift chambers.
- Debugged and timed muon counters and wrote diagnostic programs for online studying of the proportional chamber efficiencies and the pedestal stability of the calorimeter ADC's.
- Wrote the Monte Carlo simulation of the experiment and studied the acceptances for J/Ψ , χ and high transverse momentum pizero and direct photon productions.
- Demonstrated the possibility of adding a high mass diphoton trigger processor for the 1987-88 run of the experiment and contributed to its design.
- Debugged the electronics of the Single Photon and Diphoton triggers. Made modifications in the design, to ensure proper performance of the system. Wrote the diagnostic and monitor programs and maintained the system during the 1987-88 run.
- Participated in first (1985) and second (1987-88) runs of E705. Took shifts and assured the proper operation of the apparatus.
- Worked on the analysis and the code development for the electromagnetic calorimeter, extracted the high p_T pizero and direct photon signals and derived their absolute cross sections.

Acknowledgements

First I wish to apologize to anyone who I may have forgotten to mention in my acknowledgements.

The realization of a high energy experiment involves the direct or indirect participation of many people. The help given by all members of the E705 collaboration was essential for the accomplishment of the present work. I would like to thank the professors, the scientists and the students of E705, and in particular Spyros Tzamarias, Alberto Marchionni, Leonard Spiegel and Stephen Delchamps for their valuable advice, encouragement and for the great time we spent together trying to setup and run the experiment. I appreciate the support and friendship of my colleague Marzia Rosati.

I especially would like to thank my supervisor, Sergio Conetti, for his continuous assistance, and his careful and numerous readings of this thesis.

Special thanks should also be given to the technicians and the Electronics Support Group for their assistance in designing, assembling and debugging the apparatus.

I would also like to thank Patrick Aurenche for providing us with an algorithm to compare our data to QCD predictions.

Finally, I would like to thank my parents, Christos and Lia Zioulas, for their support and self sacrifice which helped me to achieve my goals, and my wife, Rachel, for her support and understanding.

Table of contents

Abstract.....	i
Sommaire.....	ii
Original Material.....	iii
Acknowledgements.....	iv
Table of contents.....	v
List of figures.....	viii
List of tables.....	xii
Chapter 1: Introduction.....	1
1.1 Overview.....	1
1.2 Quantum ChromoDynamics (QCD).....	2
1.3 Pizero inclusive cross section.....	4
1.4 Direct photons.....	7
1.5 Experimental difficulties.....	10
1.6 Previous and new experiments.....	12
Chapter 2: The experimental apparatus.....	22
2.1 The Tevatron.....	22
2.2 The Proton West beamline.....	23
2.3 The E705 spectrometer.....	26
2.4 The beam chambers, beam and veto counters.....	28
2.5 The Target.....	29
2.6 The Multiwire Proportional chambers.....	29

2.7	The analysis magnet (Rosie).....	30
2.8	The Drift chambers.....	30
2.9	The charged particle hodoscopes.....	31
2.10	The Main Array.....	33
2.10.1	The Precision Charge cards.....	36
2.10.2	The TDC system.....	37
2.10.3	LED pulser system.....	38
2.11	The photon converter.....	38
2.11.1	The Active Converter (AC).....	38
2.11.2	The Lead Gas Chamber (LGC).....	39
2.12	The Gas Tube Hodoscope (GTH).....	41
2.13	The Muon detector.....	42
2.14	The Data Acquisition system.....	42
	Chapter 3: Triggering.....	45
3.1	General.....	45
3.2	The Interaction Trigger.....	47
3.3	The Photon Trigger (the Cluster Finder).....	50
3.3.1	General.....	50
3.3.2	Functional Description and Implementation.....	54
3.3.3	ICON Circuit.....	56
3.3.4	DAC Calibration.....	59
3.3.5	Monitoring.....	61
3.3.6	Trigger efficiency.....	62
	Chapter 4: Calibration and Event reconstruction.....	67
4.1	Introduction.....	67
4.2	Calibration of the calorimeter.....	67
4.3	Energy resolution.....	74

4.4	Position resolution.....	78
4.5	Separation efficiency.....	82
4.6	Shower reconstruction.....	86
4.7	Tracking.....	92
4.8	Electron studies.....	93
Chapter 5: Data Analysis.....		99
5.1	Overview.....	99
5.2	Hadron rejection.....	103
5.3	Timing cuts.....	109
5.4	Muon rejection.....	112
5.5	Neutral mesons.....	113
5.6	Single photons.....	116
Chapter 6: Monte Carlo.....		120
6.1	General.....	120
6.2	Neutral meson geometrical acceptance and reconstruction efficiency.....	121
6.3	Single photon background from neutral meson decays.....	127
6.4	Single photon acceptance and reconstruction efficiency.....	128
Chapter 7: Results and conclusion.....		132
7.1	Cross section normalizations.....	132
7.2	Systematic errors.....	135
7.3	Pizero inclusive cross section.....	136
7.4	Direct photon cross section.....	148
7.5	Conclusion.....	149
References.....		154

List of figures

1.1	Feynman diagrams contributing to the pizero cross section.....	6
1.2	Leading order diagrams for direct photon production.....	9
1.3	Examples of higher order diagrams, contributing to the direct photon cross section.	9
1.4	The Omega spectrometer of WA70 experiment.....	17
1.5	The WA70 direct photon invariant cross sections.....	17
1.6	The NA3 spectrometer.....	18
1.7	The NA3 direct photon invariant cross sections.....	18
1.8	The NA24 spectrometer.....	19
1.9	The NA24 direct photon invariant cross sections.....	19
1.10	The UA6 spectrometer.....	20
1.11	The UA6 direct photon invariant cross section.....	20
1.12	The E706 spectrometer.....	21
1.13	The preliminary E706 direct photon invariant cross sections	21
2.1	Schematic of the Fermilab accelerator complex and the beam lines.....	23
2.2	Proton West Beamline and E705 experimental hall.....	25
2.3	The E705 spectrometer.....	27
2.4	The two types of drift chambers.....	31
2.5	The Main Array.....	34
2.6	Top view of the calorimeter.....	40
2.7	Front view of the active converter.....	40
2.8	The data acquisition system.....	44
3.1	The beam logic. Pion and proton definitions.....	48

3.2	Beam and Interaction rates as a function of the tape number.....	51
3.3	Cluster definition in the Main Array.....	52
3.4	Energy to transverse momentum conversion.....	53
3.5	Schematic diagram of modules and connections of the Cluster Finder.....	54
3.6	Interchannel comparison circuit and summation resistors.....	57
3.7	Summing and energy to transverse momentum conversion circuits.....	57
3.8	PT threshold comparison and PT bits latching circuits.....	57
3.9	Cluster Finder strobe and reset logic.....	60
3.10	Digital to Analog Converter calibration.....	60
3.11	Raw p_T distributions as seen from the Cluster Finder.....	66
3.12	Trigger Efficiency for negative and positive data.....	66
4.1	Energy distributions of electron beams.....	69
4.2	Active converter versus total energy for 31.5 GeV electrons.....	73
4.3	Percentage gain difference between the gains determined from the August and February calibrations.....	73
4.4	Energy distributions of electron beams and Gaussian fits for SF5 blocks.....	76
4.5	Energy resolutions for the SF5, the small SCG1-C behind the LGC and the large SCG1-C behind the active converter.....	77
4.6	Position resolutions for the tubes and strips of the LGC, and for the tubes and strips of the GTH.....	80
4.7	Energy correlation between the strips and the tubes of the LGC and ADC counts correlation for the GTH, for 30 GeV electron showers.....	81
4.8	Efficiency for separating two 30 GeV electron showers in the various regions of the two hodoscopes as a function of the distance between their projections.....	84
4.9	Distributions of the separation distance Δr between the two photons of $p_T > 3 \text{ GeV}/c$ pizeros on the hodoscopes.....	85
4.10	E/p distribution of showers on the calorimeter.....	96

4.11	Gaussian fits to E/p distributions for electrons	97
4.12	Positions of electron and positrons on the glass, their energy distribution and E/p distribution for $p > 20$ GeV.....	98
5.1	Energy distributions for 60 GeV pions measured by the calorimeter.....	106
5.2	Comparison between 60 GeV electrons and pions at the LGC region.....	107
5.3	γ/π^0 ratio for fake photons coming from hadronic showers versus p_T	108
5.4	Time distribution for 30 GeV electron calibration events.....	111
5.5	Time distribution of highest p_T shower for photon triggers.....	111
5.6	p_T versus x_F of single photon candidates before and after the muon cut.....	114
5.7	Muon bremsstrahlung event as seen by the E705 Display program.....	114
5.8	γ - γ invariant mass.....	118
5.9	Asymmetry distribution of pizero.....	119
6.1	Two photon showers of a pizero decay on the LGC.....	125
6.2	Comparison between the Monte Carlo predictions and the measured pizero distributions.....	126
6.3	Direct photon background from pizeros and etas.....	129
6.4	$\gamma_{\text{fake}}/\pi^0$ ratio for coalescing pizeros.....	130
6.5	Reconstruction efficiency for single photons as a function of p_T	131
7.1	Number of π^- and π^+ per spill versus the algebraic sum of the BY2 counters.....	134
7.2	Invariant cross section for $\pi^- + \text{Li} \rightarrow \pi^0 + X$ as a function of p_T averaged over the full x_F range.....	140
7.3	Invariant cross section for $\pi^- + \text{Li} \rightarrow \pi^0 + X$ as a function of x_F averaged over two ranges of p_T	141
7.4	Invariant cross section for $\pi^+ + \text{Li} \rightarrow \pi^0 + X$ as a function of p_T averaged over the full x_F range.....	142
7.5	Ratio of π^+/π^- invariant cross sections of pizero production versus p_T	143
7.6	Comparison of the E705 π -Li $\rightarrow \pi^0 X$ results with other published data.....	144

7.7	Comparison of the E705 $\pi^+\text{Li}\rightarrow\pi^0\text{X}$ results with other published data.....	145
7.8	Pizero cross sections as a function of x_T , for π^- interactions.....	146
7.9	Pizero cross sections as a function of x_T , for π^+ interactions.....	147
7.10	Production ratio of γ/π^0 for the $\pi^-\text{Li}$ data as a function of p_T	152
7.11	Direct photon inclusive invariant cross section for the $\pi^-\text{Li}$ data as a function of p_T averaged over x_F	153

List of tables

1-1	Recent fixed target experiments and their properties.	16
2-1	Beam chambers. All lengths in cm, angles in rad.....	28
2-2	Characteristics of Multiwire Proportional Chambers.....	32
2-3	Characteristics of Drift Chambers. All lengths in cm, angles in rad.....	32
2-4	Properties of SCG1-C scintillation and SF5 lead glass.	35
3-1	Percentage of various triggers recorded to tape.	46
4-1	Energy resolution constants for various types of blocks.....	75
4-2	Position resolution constants for the two views of the hodoscopes.	79
4-3	Shower widths in different regions of LGC and GTH.....	86
5-1	Percentage of events surviving first pass cuts.....	101
5-2	Number of photon triggers analyzed in each pass.	103
5-3	Hadron acceptance for various regions and cuts.....	109
5-4	Percentage of triggers surviving the out of time cut.	112
6-1	Pizero geometrical acceptance in bins of p_T and x_F	124
6-2	Pizero reconstruction efficiency in bins of p_T and x_F	124
7-1	Cross section normalization factors.	134
7-2	Inclusive cross section for $\pi^- + \text{Li} \rightarrow \pi^0 + X$ as a function of p_T and x_F	138
7-3	Inclusive cross section for $\pi^+ + \text{Li} \rightarrow \pi^0 + X$ as a function of p_T and x_F	139
7-4	Parameters of the fit of the pizero invariant cross section.....	148
7-5	γ/π^0 ratio and direct photon invariant cross section for $\pi^- \text{Li}$	151

Chapter 1

Introduction

1.1 Overview

This thesis describes the measurements of the production of pizeros and photons by high energy pion and proton beams hitting a target, as determined by E705, an experiment performed at the Fermi National Accelerator Laboratory (Fermilab). Partial results are then compared to corresponding measurements from other experiments and to theoretical predictions.

The measurement of the direct photon cross section is an important tool to investigate the validity of Quantum ChromoDynamics (QCD)^{[1],[2]}, the theory that describes the nuclear strong force in terms of interactions among quarks, believed to be the constituents of strongly interacting particles (generically referred to as "hadrons") and gluons, the actual carriers of the strong force.

In the next sections of this chapter a short description of the QCD theory and the theoretical determinations of the pizero and direct photon cross sections within the framework of the theory are given. At the end of this chapter the problems that appear in

direct photon experiments and the ways that other experiments have approached them are described.

1.2 Quantum ChromoDynamics (QCD)

The last years have seen a tremendous advance in the understanding elementary particles. The main steps have consisted of the introduction of the quark model, which clarified the reality underlying the complex features of hadron spectroscopy, and the development of the theory of QCD.

Quarks were proposed by Gell-Mann^[3] in 1964 as spin 1/2 particles with fractional electric charge, which represented the basic building blocks of mesons (consisting of quark-antiquark pairs) and baryons (three quarks). Experimental evidence shows that there are six types (flavors) of quarks: up (u), down (d), strange (s), charm (c), beautiful or bottom (b) and top (t). The six quarks are grouped in three families or "generations" (ud), (sc) and (bt), in analogy to the three lepton families ($e\nu_e$), ($\mu\nu_\mu$), ($\tau\nu_\tau$). Although the top quark has not been detected up to now, its existence is strongly implied by the detection of the bottom quark in order to complete the third generation. In addition to the flavor quantum number, the study of hadron behavior showed the necessity of introducing another quark quantum number, color^[4], which can appear in three varieties. The three colors specify the "strong" charges similarly to the "+" and "-" classification of electric charges.

The breakthrough on the way to a theory for the description of the hadronic structure and the dynamics of the strong interactions was the result of experiments studying inelastic scattering^[5] of very high energy electrons off protons. The interpretation of the experimental results, which seemed to indicate the presence of some internal structure in the proton, was put forward by Bjorken^[6] and Feynman^[7] who introduced the parton model, setting the basis for the QCD theory. The hadrons were viewed as sets of freely moving point-like

constituents, the partons. These constituents of hadrons are quarks and electrically neutral gluons, which are responsible for keeping the quarks together inside hadrons. Strong indirect evidence for the presence of gluons is the experimental fact^[8] that the charged constituents carry only 50% of the nucleon's momentum while gluons account for the rest.

Quantum ChromoDynamics describes the strong color interactions between quarks, which interact with each other by exchanging gluons, in a similar way that charged particles interact electromagnetically by exchanging photons, as described by the theory of Quantum ElectroDynamics (QED). In analogy with QED, interactions in QCD can also be described by Feynman diagrams. The main difference is that gluons carry the strong charge (color), while the photons do not carry electromagnetic charge.

Another essential and distinguishing feature of QCD is that the strong coupling constant α_s , the QCD equivalent of QED's fine-structure coupling constant α , depends on a scale, usually referred to as Q^2 , which characterizes the "hardness" of the parton-parton interaction. Q^2 is defined as the 4-momentum transfer characteristic of the process that is examined. At infinite Q^2 the partons can be considered as free, since the coupling constant α_s is believed to approach zero as $Q^2 \rightarrow \infty$. This principle is called "asymptotic freedom", and it allows the calculation of the cross sections for the interactions assuming the constituents as free inside the hadrons. On the other hand, for small values of Q^2 (corresponding to interactions at large distances) the coupling constant and the forces between quarks increase, keeping them always bound inside hadrons (confinement). For large values of Q^2 , α_s can be small enough so that perturbation methods can be applied to the cross section calculations. Up to first order term, the coupling constant can be written as:

$$\alpha_s(Q^2) = \frac{12\pi}{[33 - 2N_f] \ln \frac{Q^2}{\Lambda^2}}$$

where N_f is the number of flavors (and for the energies of the experiments considered here $N_f=3$). In the case of lepton-nucleon scattering, Q^2 is the 4-momentum transfer squared of

the lepton. In hadronic collisions Q^2 is not well defined because of the large number of subprocesses that contribute to the final cross section. It is usually taken as:

$$Q^2 = \frac{2\hat{s}\hat{t}\hat{u}}{\hat{s}^2 + \hat{t}^2 + \hat{u}^2}$$

where $\hat{s}, \hat{t}, \hat{u}$ are the Mandelstam variables for the parton scattering. The parameter Λ appears in the theory as controlling the scaling and it is determined experimentally.

1.3 Pizero inclusive cross section

Within the framework of QCD, the cross section for an interaction among hadrons of the type $A+B \rightarrow C+\dots$, where only the inclusive production of particle C is measured among the final states, can be described in terms of the elementary processes among the fundamental constituents. For such a process the cross section can be written as^[9]:

$$E \frac{d\sigma}{d^3p} = \sum \int dx_a dx_b dz_c G_{a/A}(x_a, Q^2) G_{b/B}(x_b, Q^2) D_{C/c}(z_c, Q^2) \frac{\hat{s}}{z_c^2 \pi} \frac{d\sigma}{d\hat{t}}(ab \rightarrow cd) \delta(\hat{s} + \hat{t} + \hat{u})$$

where the sum is over all the two-body $ab \rightarrow cd$ parton scattering subprocesses that can contribute to the final state under question. The functions $G_{a/A}$ and $G_{b/B}$ are the structure functions of the partons a and b in the hadrons A and B divided by x_a and x_b respectively. The structure functions denote the probability of finding a parton a in a hadron A with momentum fraction lying between x_a and x_a+dx_a . The function $D_{C/c}$ denotes the probability of obtaining a hadron C with a momentum fraction between z_c and z_c+dz_c from a parton c, and it is called fragmentation function. z_c is the fraction of the momentum of the parton c that is carried by the final state hadron C. $\hat{s}, \hat{t}, \hat{u}$ are the Mandelstam variables and the delta function ensures energy conservation. The fact that the partons can also have transverse momentum inside hadrons (intrinsic momentum k_T) is neglected in this approach.

Structure and fragmentation functions cannot be calculated within the framework of perturbative QCD but may be experimentally determined. Two methods have mainly been used in the last years to measure structure functions: the deep inelastic scattering of leptons from a nucleon and the Drell-Yan process in hadronic interactions. In the former, a lepton interacts with a quark through a “space-like” virtual photon or a W or a Z boson and in the latter, a quark of one hadron annihilates with an antiquark of another hadron to a “time-like” massive virtual photon, which then materializes into a lepton-antilepton pair. If these reactions are studied for values of the square of the virtual photon's mass ($=Q^2$) much greater than 1 GeV^2 , then perturbative QCD can be applied. Although these two methods have produced a large number of measurements of the quark structure functions in the nucleon and have been important tests of QCD, they have the disadvantage of providing no direct information on the gluon constituent of the hadrons, since the gluons only appear in higher order Feynman diagrams. The study of hard hadron-hadron scattering can remedy such a deficiency.

The study of hadron inclusive cross section allows one in principle to get information on all the partonic subprocesses, but it involves considerable complications. Quarks and gluons must “fragment” into hadrons of lower p_T and the resulting hadrons have to be associated with their parents partons before any information can be extracted. The fragmentation function is an additional unknown appearing in the expression for the cross section. The large number of Feynman diagrams (see figure 1.1), 127 if three flavors are used, makes the calculations complicated and hard. As will be seen in the next section, direct photon production is an excellent tool to both measure gluon structure functions and to test QCD theory.

The measurement of the pizero inclusive cross section, while interesting on its own merit, is also very important for a direct photon experiment, since the π^0 's are the major source of background to the direct photon signal, as it will be discussed in section 1.5.

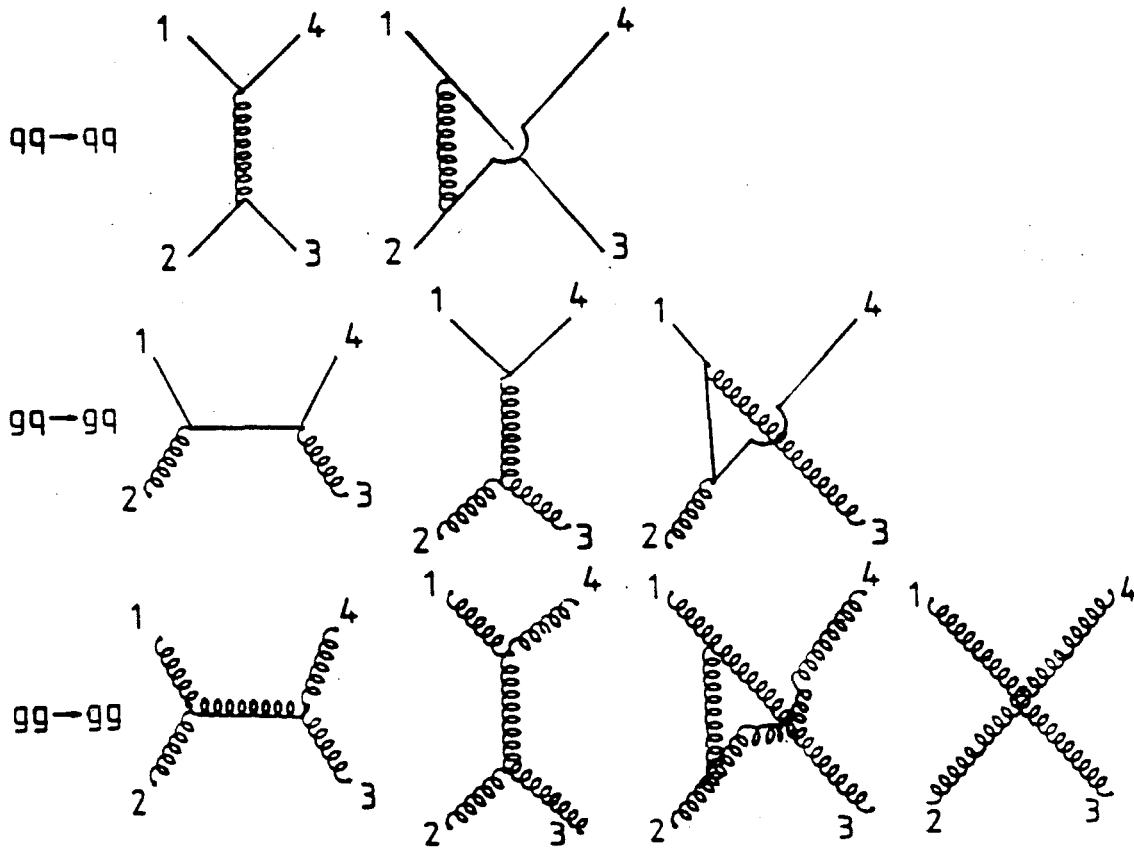


Figure 1.1 Feynman diagrams contributing to the pizero cross section.

1.4 Direct photons

Direct photons are defined as photons originating from the direct result of an interaction between partons and not as the product of the decay of a hadron produced in the interaction or some other secondary process. Consequently, direct photons carry information directly associated to the kinematics of the parent parton: Immediate consequences are the simplicity of the first order in α_s expression for the cross section and the ease of comparison between theory and experiment.

To first order there are two diagrams which contribute to direct photon production: Quark-antiquark "annihilation" and gluon "Compton" scattering (figure 1.2). It can be seen that gluons appear in both diagrams, in the final and initial states respectively. The Compton diagram provides, in principle, information about the gluon structure function of the colliding hadron, while the annihilation diagram provides, in principle, information about the gluon fragmentation function. In planning an experiment, an important consideration is the choice of the beam and the target. In the case of direct photons produced by π^- (\bar{p}) and π^+ (p) beams on a target consisting of equal number of protons and neutrons (isoscalar target), the Compton term contributes equally to the cross sections for either nucleon. A subtraction of the π^+N (pp) from the π^-N ($\bar{p}p$) cross section can then isolate the contribution of the annihilation term. Moreover, when studying differences of cross sections, the use of an isoscalar target will allow the elimination of any background to the direct photon signal due to strong π^0 or η production, since the background contribution is the same for either process. However, direct photon production is easier to interpret for interactions of hadrons with only protons (H_2 target).

The invariant inclusive cross section for direct photon production in the interaction $A+B \rightarrow \gamma+X$ can be written as:

$$E \frac{d\sigma}{d^3p} = \sum \int dx_a dx_b G_{a/A}(x_a, Q^2) G_{b/B}(x_b, Q^2) \frac{\hat{s}}{\pi} \frac{d\sigma}{dt} (ab \rightarrow cd) \delta(\hat{s} + \hat{t} + \hat{u})$$

where the \hat{s} , \hat{t} , \hat{u} are the Mandelstam variables and $d\sigma/d\hat{t}$ is the cross section of the subprocess $ab \rightarrow \gamma d$. In the above expression, $x_a G_{a/A}$ and $x_b G_{b/B}$ are the structure functions of partons a and b in the hadrons A and B . The sum is over all the possible diagrams. The cross sections of the two subprocesses are:

$$\frac{d\sigma}{d\hat{t}}(gq \rightarrow \gamma q) = -\frac{\pi\alpha\alpha_s}{3\hat{s}^2} e_q^2 \left(\frac{\hat{u}}{\hat{s}} + \frac{\hat{s}}{\hat{u}} \right)$$

and

$$\frac{d\sigma}{d\hat{t}}(q\bar{q} \rightarrow \gamma g) = \frac{8\pi\alpha\alpha_s}{9\hat{s}^2} e_q^2 \left(\frac{\hat{u}}{\hat{t}} + \frac{\hat{t}}{\hat{u}} \right)$$

Unfortunately, the first order diagrams are not enough to fully calculate the direct photon cross section. There is a large number of higher order diagrams (see figure 1.3) which complicate the calculation of the cross sections. In addition, the Q^2 scale introduces an uncertainty, since the theory does not restrict it to any particular form. There have been different approaches in attacking this problem.

The second order calculations of the direct photon cross section done by P. Aurenche et al.^[10] use a scaling based on an optimization procedure determined from the Principle of Minimal Sensitivity (MS)^{[11],[12],[13]}. Such a procedure, where Q^2 is chosen as to minimize the variation of the cross section with small changes in the scale, results in scales that are complicated functions of p_T .

A more "natural" choice of scale was done by A. Contogouris et al.^[14] using $Q^2 = M^2 = p_T^2$ and the leading logarithm approximation. The corrections to the next-to-leading order were done taking into account the structure function dependence on the intrinsic transverse momentum (k_T) of the partons and contributions from second order bremsstrahlung diagrams and higher twist effects. The steep falling of the cross sections with p_T makes the dependence on k_T very important, particularly at lower p_T values ($p_T < 5$ GeV/c). The higher order corrections were applied as K factors, determined from loop graphs in the soft gluon limit and from certain collinear gluon bremsstrahlung configurations.

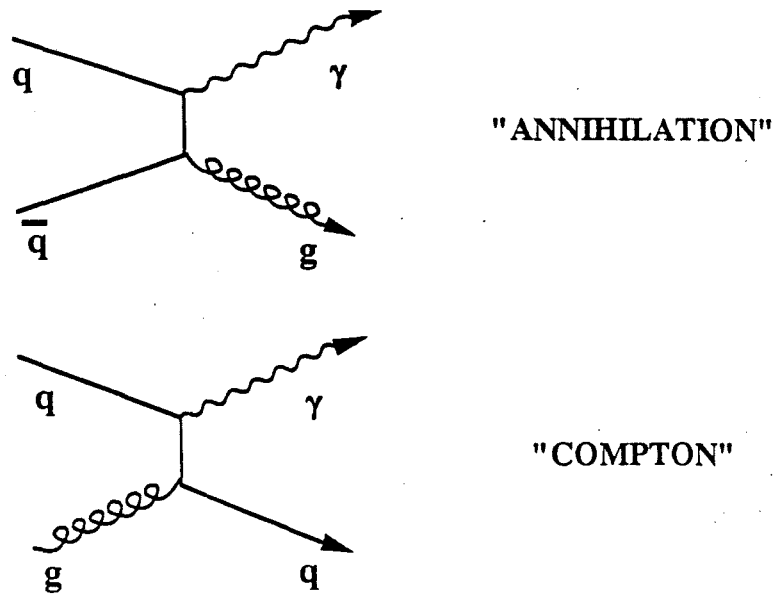


Figure 1.2 Leading order diagrams for direct photon production.

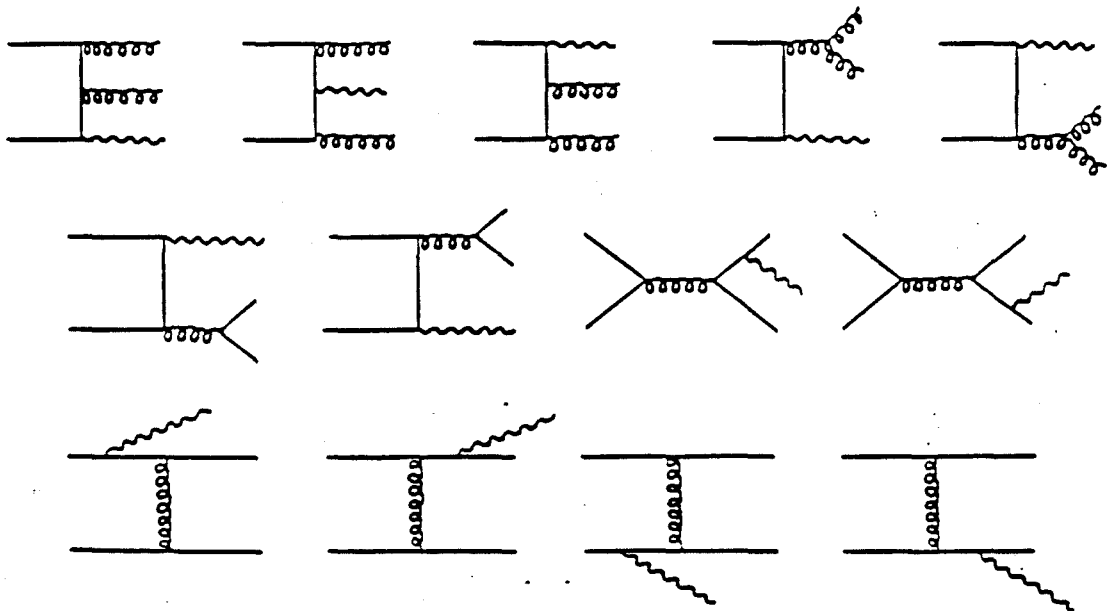


Figure 1.3 Examples of higher order diagrams, contributing to direct photon production.

A comparison of the two methods can be found in reference 15. A comparison with the data of the most recent experiments is shown in the figures 1.5 to 1.11 appearing at the end of this chapter.

The experimentally measured kinematical variables of the hadroproduced direct photon are the transverse momentum p_T , the Feynman x_F and/or the rapidity y . The last two are defined as:

$$x_F = \frac{2p_z^*}{\sqrt{s}} \quad y = \frac{1}{2} \ln \left[\frac{E + p_z}{E - p_z} \right]$$

where p_z^* , \sqrt{s} are the longitudinal momentum of the photon and the total energy in the center of mass of the interaction, while p_z and E are the total momentum and the energy of the photon in the laboratory frame .

1.5 Experimental difficulties

From what was said so far, direct photon production appears to be an excellent tool to study hadronic structure and to test QCD predictions. However, the small cross section, a consequence of the electromagnetic vertex introducing a factor α_s/α with respect to a pure hadronic process, make the experimental detection difficult. The photon signal is buried under a large background from the electromagnetic decays of neutral mesons, which are produced in much larger numbers than direct photons.

The problem of small cross sections can be solved by designing a high luminosity experiment, but the problems of selecting the signal (triggering) from the large number of interactions and of extracting the signal from the background in the recorded data still remain. A good trigger is necessary in order to reduce the number of events collected and consequently the number of hours (or better, years) of computer time needed to analyze them and extract a signal.

The major background to direct photon signals comes from pizeros and etas, whose branching ratios into two photons are 98.8% and 38.9% respectively. If one of the two decay photons is lost, either because of the limited geometrical acceptance of the detector, or due to off-line reconstruction problems, then the other photon will appear as a single (direct) photon candidate. Another loss of photons is their conversion to e^+e^- pairs in the material between the interaction point and the photon detector, and the subsequent loss of an electron or a positron or both. If both photons are detected and their energies and positions are measured, then a calculation of the invariant mass of the pair can identify their parentage.

Large solid-angle coverage helps to minimize the loss due to geometrical acceptance. The apparatus has to be able to perform in high beam intensities (because of the small cross sections) and to detect charged and neutral particles. For the determination of the photon's energy, one typically uses a calorimeter, which must have enough radiation lengths to contain the whole electromagnetic shower and a minimum of interaction lengths, to reduce the probability of hadron interaction and contamination of the photon sample. The calorimeter must be capable of measuring high energy showers as well as low energy ones, so that asymmetrically decaying pizeros can be detected. In the high p_T region, pizeros have high energies which correspond to small opening angles ($\theta_{\text{OPEN}} \geq 1/\gamma\pi^0$) between the two photons. This requires the calorimeter to be far enough from the interaction point for the photons to be well separated, which obviously introduces problems of size and solid angle coverage. The required distance of the calorimeter from the target is somewhat dictated by the spatial resolving power of the former. A highly segmented calorimeter can distinguish between a single photon shower and two overlapping showers coming from a pizero decay, even when their separation becomes very small. On the other side, size and segmentation of the detector increase its cost and introduce technical difficulties of construction. The combination of all these factors makes the search for direct photons challenging.

1.6 Previous and new experiments

Over the past fifteen years, a large number of fixed target and collider experiments have taken data, to study the direct photon production with a variety of beam types and energies.

The first experiment^[16] to see direct photons, although it was not designed for this purpose, was performed at the Intersecting Storage Rings (ISR) of the Center of European Nuclear Research (CERN). Photons were detected by a lead glass block array located at 90° in the center-of-momentum of the proton-proton system. The measured γ/π^0 ratio, corrected for all instrumental effects, had a non-zero value in the p_T range between 1 and 3.6 GeV/c, suggesting a direct production of photons. The systematic uncertainties were large and the group presented their results only as a suggestion of direct photon production.

The second reported result^[17] came from another CERN ISR experiment, using similar apparatus. Their photon detector consisted of a 9×15 array of lead glass blocks, each with $10 \times 10 \text{ cm}^2$ cross section. It was operated at two distances from the interaction point, 4.7 m, 1.47 m, and covered a p_T range between 2 and 5 GeV/c. The results confirmed the existence of direct photons with lower systematic uncertainties than the previous experiment.

Subsequent “second generation” experiments, using better apparatus and recording higher luminosities, provided more detailed measurements of the inclusive cross sections in different regions of the phase space. A short description of the latest fixed target experiments and their techniques is given here. A more detailed experimental review can be found in references 18 and 19. Table 1-1 shows a selection of fixed target experiments and their properties.

Experiment WA70^[20] was performed at the CERN Super Proton Synchrotron (SPS) with 280 GeV/c π^- , π^+ and p beams on a 1 m long liquid hydrogen target, using the Omega Spectrometer (figure 1.4). A fine-grained electromagnetic calorimeter consisting of lead and liquid scintillator was positioned 10.9 m downstream of the center of the target. The

calorimeter, $4 \times 4 \text{ m}^2$ in area and 24 radiation lengths deep, provided a large p_T and x_F acceptance, electromagnetic shower separation down to 2 cm (corresponding to $p_T=12 \text{ GeV/c}$ for $x_F=0$) and efficient photon reconstruction for energies greater than 500 MeV. The data collection reached integrated luminosities for π^-p , π^+p and pp , of 10.8 pb^{-1} , 1.3 pb^{-1} and 5.2 pb^{-1} respectively. The measured invariant cross sections for γ production from π^- and π^+ as a function of p_T for various x_F ranges are shown in figures 1.5a,b. The solid and dashed lines correspond to the second order QCD calculations using the optimized scale with the Duke and Owens (D.O.) sets 1 and 2 structure functions^[21] respectively. The data seem to favor the set 1 over the set 2 in almost all p_T intervals.

Experiment NA3^[22] was performed at the CERN SPS with 200 GeV/c π^- , π^+ and p beams on a Carbon target, consisting of three cylinders, each 2 cm long, mounted along the beam direction. The NA3 spectrometer is shown in figure 1.6. The electromagnetic calorimeter was made of a lead scintillator sandwich of 25 radiation lengths and it was positioned about 14 m downstream of the target. A $4 \times 2 \text{ m}^2$ proportional chamber was added between the first and the second segment of the calorimeter to give the position of the showers. The two shower minimum separation was about 3 cm (corresponding to $p_T=12 \text{ GeV/c}$ for $x_F=0$) and the smallest measurable energy was 1 GeV. Figures 1.7a,b show the measured invariant cross sections for π^-C and π^+C integrated over the rapidity range as a function of p_T . The solid and dashed lines are the QCD calculations with optimized scale and $Q^2=p_T^2$ respectively, using the D.O. set 1 structure functions.

Experiment NA24^[23] was performed at the CERN SPS with 300 GeV/c π^\pm and p beams on a 1 m long liquid hydrogen target. Figure 1.8 shows the NA24 spectrometer. The calorimeter consisted of a fine-grained photon position detector of 9.6 radiation lengths made from alternate layers of lead sheet and proportional tubes, followed by a 240-cell ring calorimeter consisting of 16 radiation lengths of lead/scintillator sandwich. It was located 8.12 m downstream of the center of the H_2 target and covered an area of $3 \times 3 \text{ m}^2$. The separation resolution was 3 cm (corresponding to $p_T=5.8 \text{ GeV/c}$ for $x_F=0$) and the minimum

reconstructed photon energy 2 GeV. The accumulated luminosities for the π^-p , π^+p and the pp interactions were 1.33, 0.19 and 0.45 pb^{-1} respectively. Figure 1.9 shows the invariant cross sections for the inclusive direct photon production of the three beam types versus p_T . The solid and dashed lines are the QCD calculations with optimized scale and the D.O. structure functions sets 1 and 2 respectively. The dashed-dotted curves are the results of a fixed scale $Q^2=4p_T^2$ and set 1.

Experiment UA6^[24] was also performed at the CERN SPS with 315 GeV/c \bar{p} and p beams on a hydrogen jet internal target followed by a double arm spectrometer (figure 1.10). Each electromagnetic calorimeter consisted of 30 lead plates, 0.8 radiation lengths thick, interleaved with alternating layers of horizontal and vertical proportional tubes. It was positioned about 10 m downstream of the center of the target. The minimum resolved two-shower separation was 2.8 cm (corresponding to $p_T=7.4$ GeV/c for $x_F=0$) and the minimum measurable photon energy, 2 GeV. The accumulated luminosities for the $\bar{p}p$ and the pp interactions were 3.5 and 6.1 pb^{-1} respectively. Figures 1.11a,b show the measured γ/π^0 ratio and the invariant cross section for direct photon production at an average rapidity of 0.4 as a function of p_T . The QCD predictions for optimized scale and D.O. set 1 (solid line) and set 2 (dashed line) and for the scale $Q^2=p_T^2$ (dashed-dotted line) are shown. The plots represent a subsample of the data collected.

Experiment E706^[25] is performed at Fermilab with 530 GeV/c π^\pm , K^- and p beams on two Cu targets 0.08 cm thick followed by twenty Be targets 0.2 cm thick. The E706 spectrometer is shown in figure 1.12. It uses a large (3m in diameter) liquid-argon calorimeter consisting of electromagnetic and hadronic components located 9 m downstream of the target. The electromagnetic section consists of 66 layers of 0.2 cm lead sheet and fiberglass (G-10) anode boards having radial and azimuthal segmentation. Longitudinally, it is read out in two sections of about 10 and 20 radiation lengths. The fine granularity, about 0.55 cm in r , is enough to resolve two photons separated by 0.8 cm at the calorimeter (corresponding to $p_T=18$ GeV/c for $x_F=0$). The experiment accumulated about 1 pb^{-1} of total

luminosity from the first run and is due to take more data in the 1990-91 fixed target period at Fermilab. Preliminary results are shown in figure 1.13.

TABLE 1-1 Recent fixed target experiments and their properties.

Experiment	Beam	Target	p_{LAB} (GeV/c)	p_{T} (GeV/c)	rapidity range
E705	π^{\pm} , p, \bar{p}	Li	300	$4 \rightarrow 7$	$-0.6 \rightarrow 0.8$
E706	π^{\pm} , K^{-} , p	Be, Cu	530	$3 \rightarrow 10$	$-0.9 \rightarrow 0.9$
WA70	π^{\pm} , p	H ₂	280	$4 \rightarrow 7$	$-1.0 \rightarrow 1.0$
NA3	π^{\pm} , p	H ₂	200	$3 \rightarrow 6$	$-0.4 \rightarrow 1.2$
NA24	π^{\pm} , p	C	300	$2.75 \rightarrow 7$	$-0.8 \rightarrow 0.8$
UA6	p, \bar{p}	H ₂	315	$3 \rightarrow 7$	$-0.4 \rightarrow 1.25$

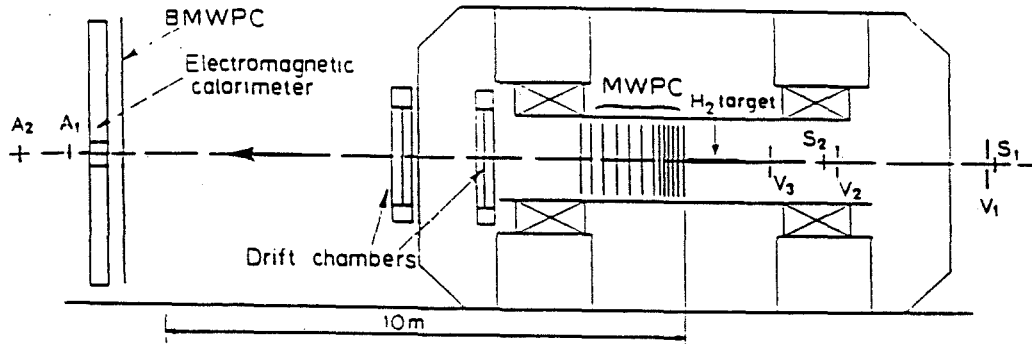


Figure 1.4 The Omega spectrometer of WA70 experiment.

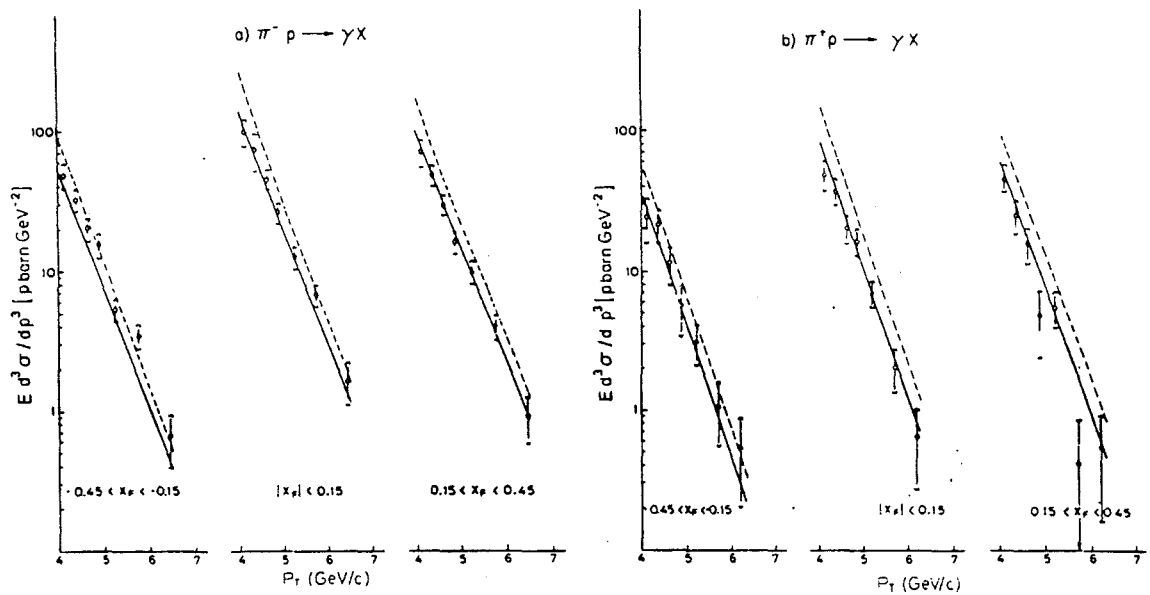


Figure 1.5 The WA70 direct photon invariant cross sections from π^- (a) and π^+ (b) as a function of p_T for various x_F ranges. The solid and dashed lines correspond to the second order QCD calculations using the optimized scale with the D.O. sets 1 and 2 structure functions respectively.

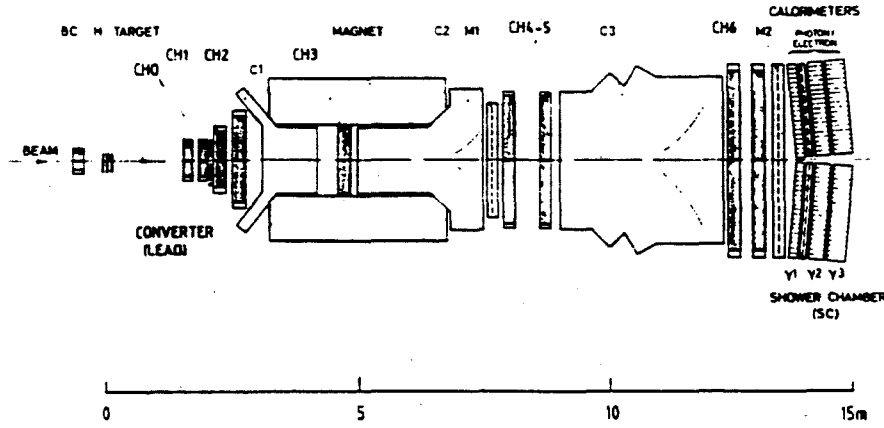


Figure 1.6 The NA3 spectrometer.

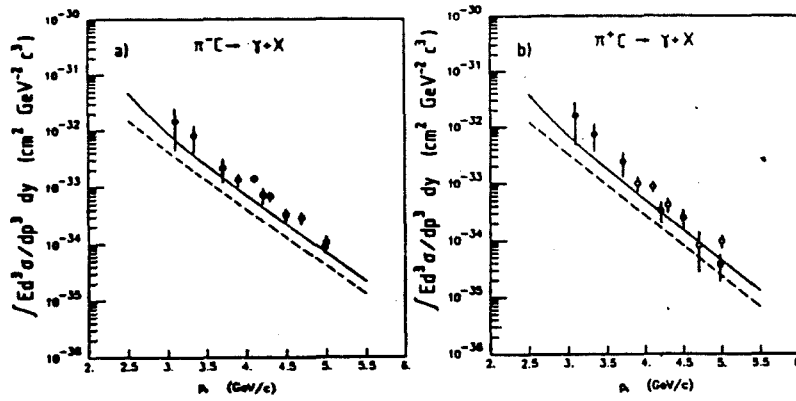


Figure 1.7 The NA3 direct photon invariant cross sections from π^- (a) and π^+ (b) as a function of p_T , integrated over the rapidity. The solid and dashed lines correspond to the QCD calculations using the optimized and natural scales respectively with the D.O. set 1 structure functions.

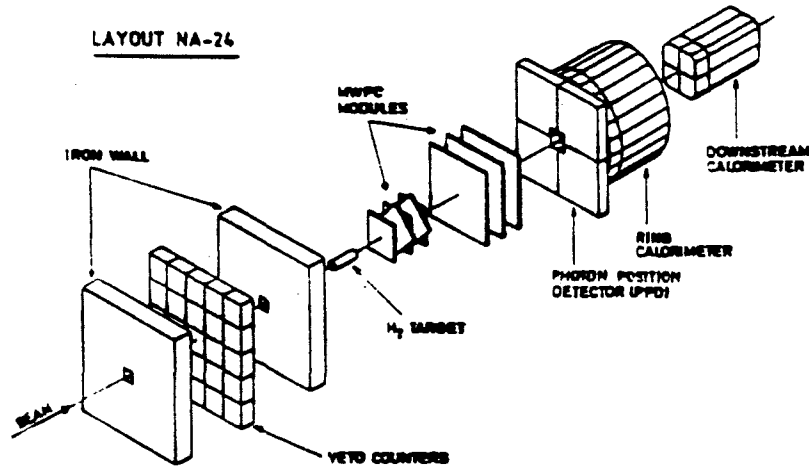


Figure 1.8 The NA24 spectrometer.

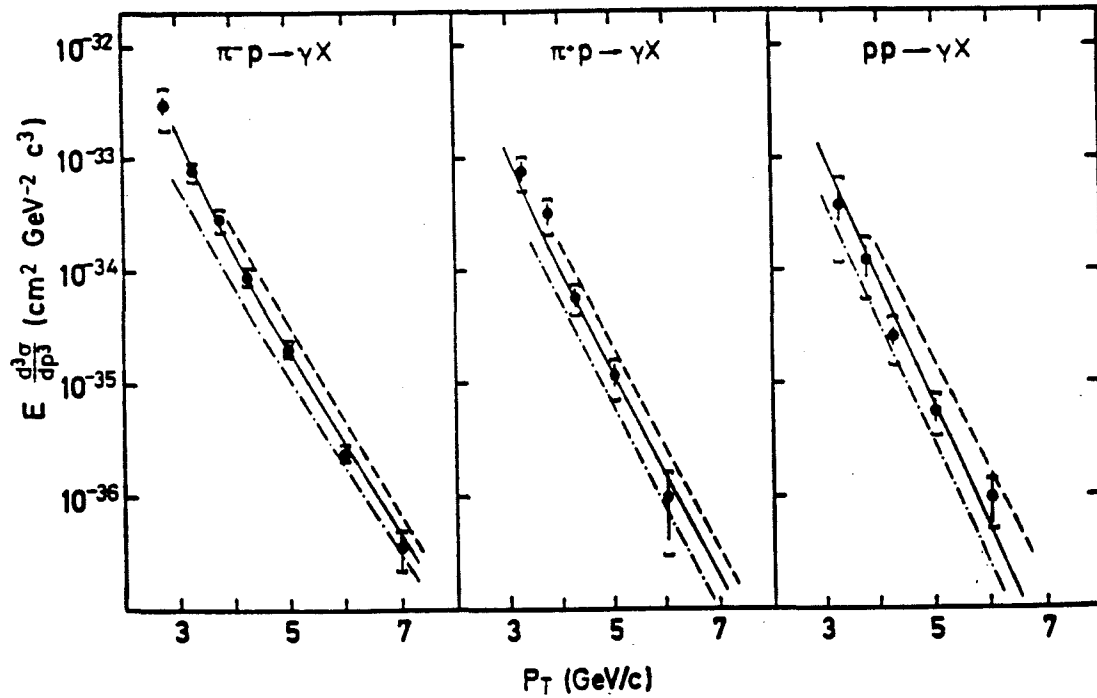


Figure 1.9 The NA24 direct photon invariant cross sections from π^- , π^+ , p as a function of p_T . The solid and dashed lines correspond to the second order QCD calculations using the optimized scale with the D.O. sets 1 and 2 structure functions respectively. The dashed-dotted line are from the natural scale and set 1.

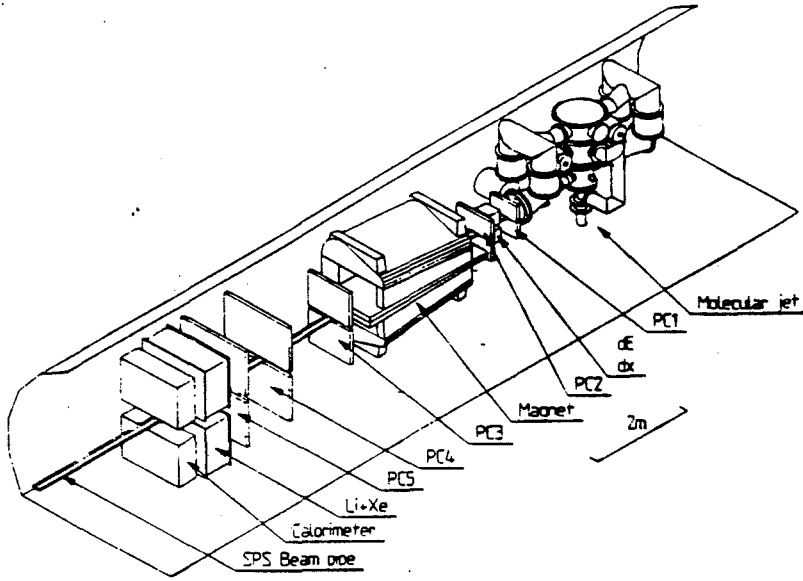


Figure 1.10 The UA6 spectrometer.

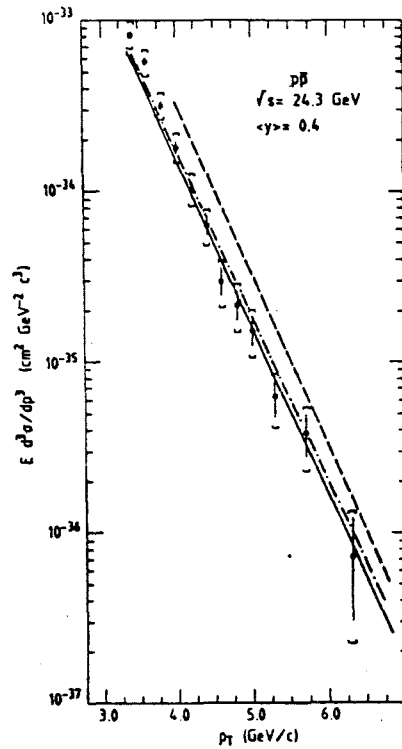


Figure 1.11 The UA6 direct photon invariant cross section as a function of p_T at an average rapidity 0.4. The solid and dashed lines correspond to the second order QCD calculations using the optimized scale with the D.O. sets 1 and 2 structure functions respectively. The dashed-dotted line is from the natural scale and set 1.

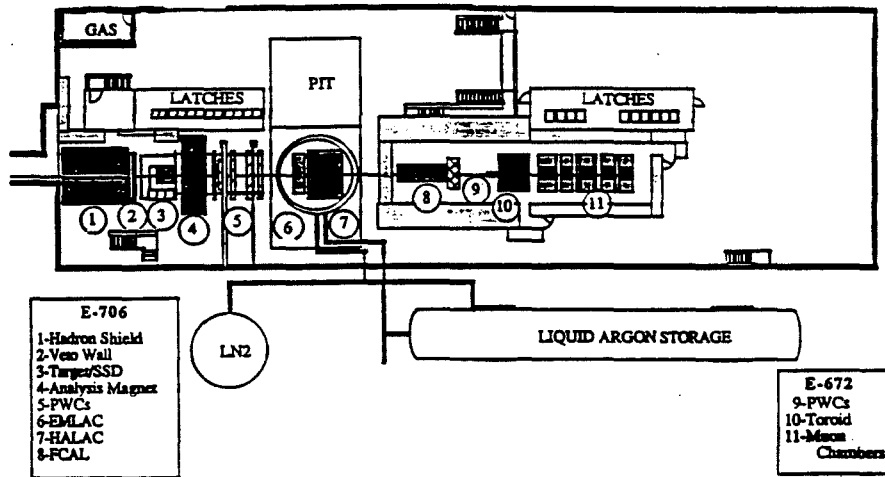
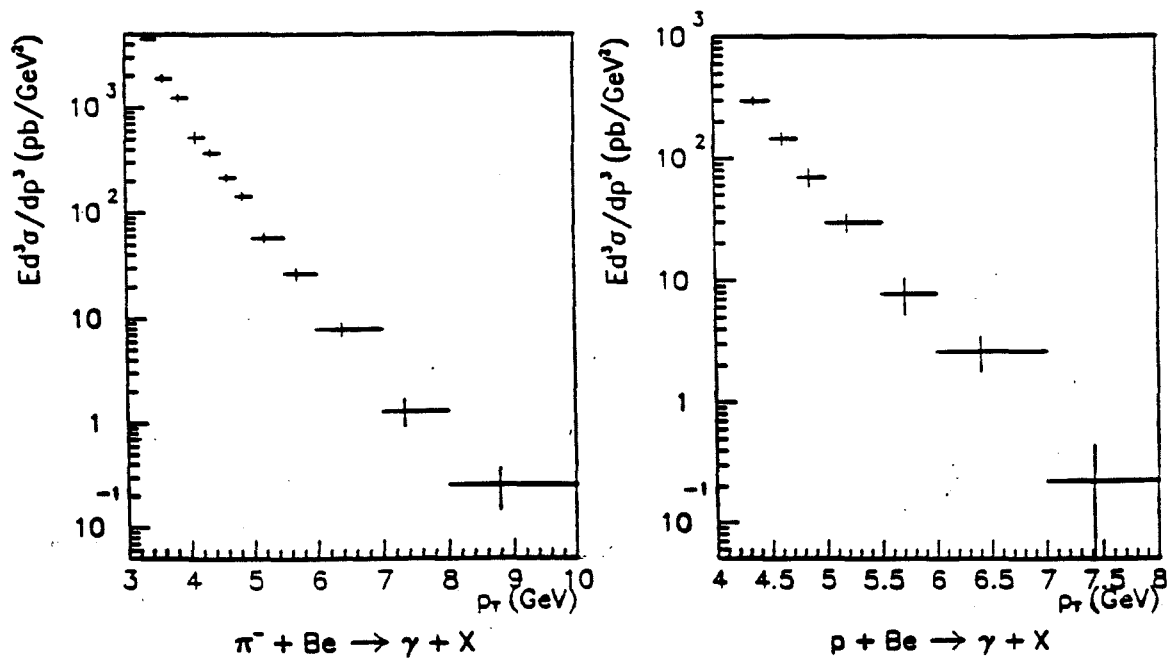


Figure 1.12 The E706 spectrometer.

Figure 1.13 The preliminary E706 direct photon invariant cross sections for π^- and p beams as a function of p_T .

Chapter 2

The experimental apparatus

2.1 The Tevatron.

The experiment which is the subject of this thesis, FNAL E-705, took place in the Proton West area of the Fermi National Accelerator Laboratory. The Fermilab accelerator complex (figure 2.1), capable of accelerating extractable proton beams up to 800 GeV, consists of an 800 keV Cockroft-Walton pre-accelerator followed by a 200 MeV LINAC, an 8 GeV booster synchrotron, the 150 GeV Main ring conventional synchrotron and finally the 800 GeV Tevatron, a 1 km radius ring of superconducting magnets. The proton beam is extracted from the Tevatron for 20 sec out of every minute and is split several ways enabling different experiments to run simultaneously.

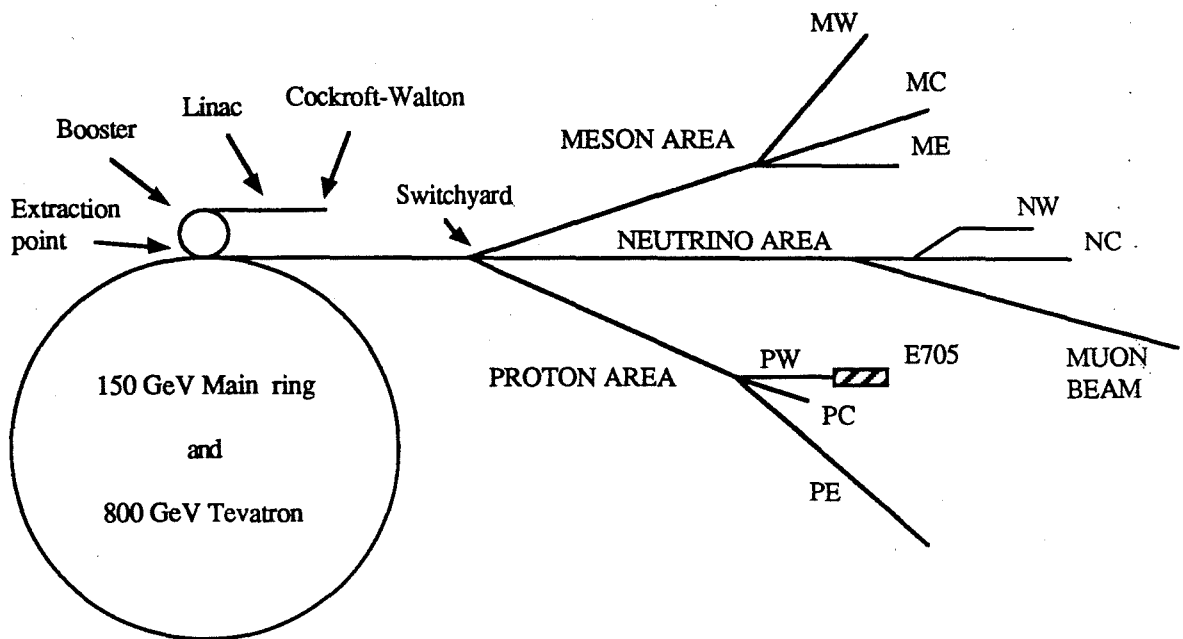


Figure 2.1 Schematic of the Fermilab accelerator complex and the beam lines.

2.2 The Proton West beamline

The Proton West beamline consisted of a series of dipole and quadrupole magnets (figure 2.2) which bend and focus the beam respectively. The accelerator delivered the beam particles as a train of equally spaced bunches (referred to as "buckets"). The separation between buckets was about 19 nsec which corresponds to the accelerator 53.1 MHz RF cavity tune.

Secondary negative and positive beams were produced in two different modes, referred to as *charged* and *neutral*. In the charged mode, the primary 800 GeV proton beam was directed onto a Be target at an angle, producing positive and negative particles, mostly pions and protons. The PW6W2 magnet selected negatively charged tracks while diverting

to a dump the positively charged tracks. The derived momentum (300 GeV/c) pions and protons were selected by the combination of the PW6W3 dipole magnet and a set of collimators: the Momentum Slit. In the neutral mode, the primary beam hit the target at 0^0 with respect to the beamline, and the PW6W2 magnet running full power swept away most charged tracks including the non-interacting primary beam, letting through only the neutral tracks. The final (negative) beam, consisting of \bar{p} 's and π^- 's, was produced from the decays of $\bar{\Lambda}$'s and \bar{K}^0 's into $\bar{p}\pi^+$'s and $\pi^-\pi^+$'s respectively. This way, the beam had a lower yield than in the charged mode (5×10^{-6} particles/primary proton, as opposed to 3×10^{-4} for the charged mode) but it was enriched in \bar{p} , with a ratio \bar{p}/π^- about 8% and no K contamination, while such a ratio when running the negative beam in "charged" mode was about 1.5%.

Another type of beam which could be generated was an electron beam useful for the purpose of calibrating the electromagnetic detector. This was achieved by making use of the EMAKER, a lead plate inserted in the neutral beam to convert the photons to electron-positron pairs. The momentum of the electron (positron) beam was selectable by the combination of PW6W3 and the momentum slit. Electron beams of momenta of 2, 6, 10, 30, 60 and 100 GeV/c were used periodically for the calibration of the electromagnetic calorimeter.

The beam was tracked by a set of three multiwire proportional chambers, described in the beam chambers section.

In normal 300 GeV/c running a beam particle was tagged either as a pion or (anti)proton by a set of two threshold Cerenkov counters. The counters were filled with helium at pressure of 1.8 psi, chosen to discriminate pions from protons. Ideally, both counters gave light for pions going through them, and no light for protons. A distinction between pions and electrons was also done for the electron beams, by adjusting the pressure according to the different beam energies.

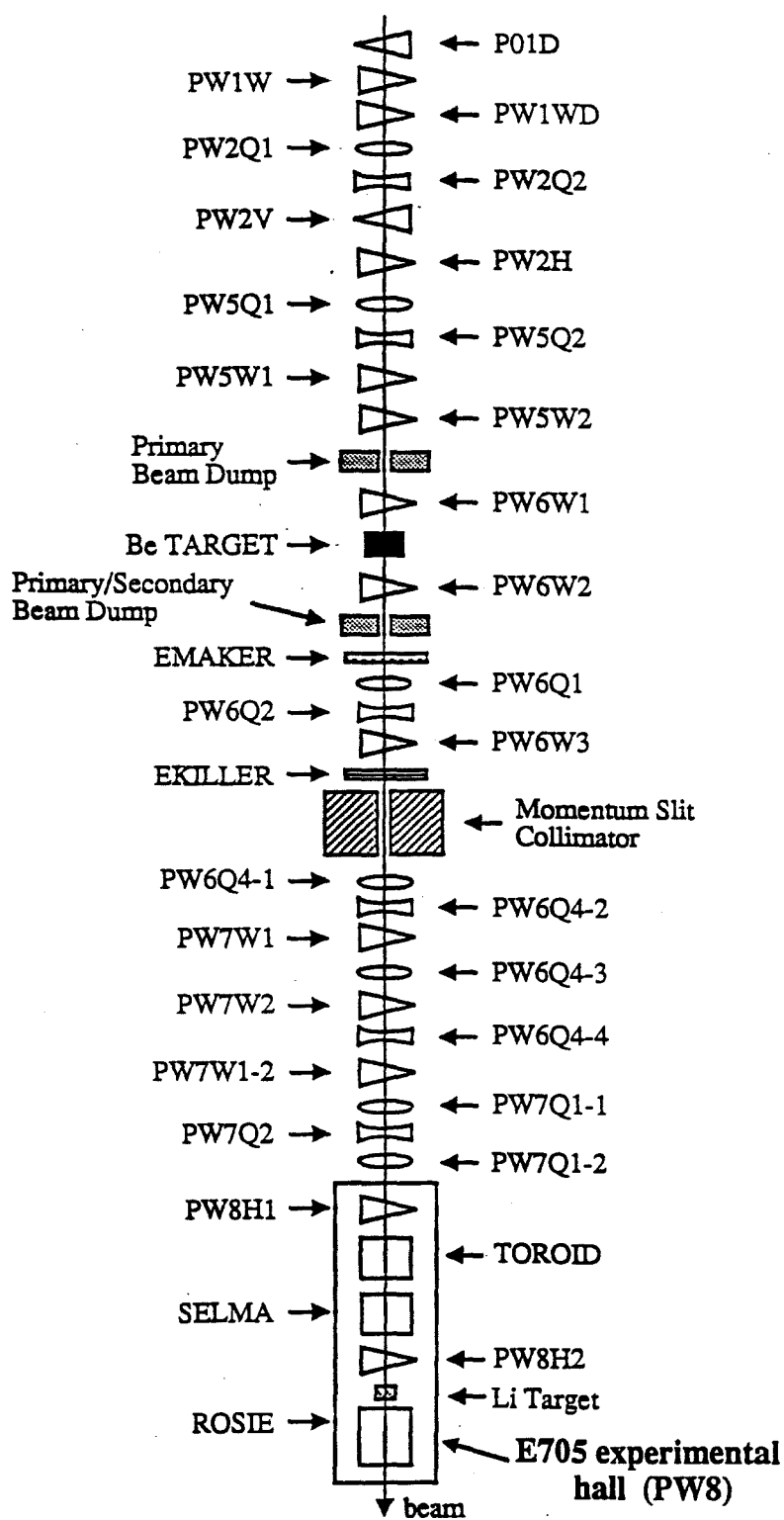


Figure 2.2 Proton West Beamline and E705 experimental hall.

2.3 The E705 spectrometer

The E705 spectrometer (figure 2.3) consisted of a set of multiwire proportional and drift chambers for the tracking of the charged particles, an analysis magnet ("Rosie"), an electromagnetic calorimeter for the position and energy measurement of photons and electrons, and a muon detector made of scintillation counters alternating with blocks of steel and concrete.

The target was positioned about 5.33 m before the center of the analysis magnet.

The segments of the charged particle trajectories between the target and the magnet ("upstream" tracking) were tracked by a set of 19 proportional and 9 drift wire planes. After the magnet, particles were tracked by a set of 12 drift wire planes ("downstream" tracking). A set of vertical and horizontal scintillation counters followed the chamber system. Its signals were used for track verification and as an input to a fast trigger.

The electromagnetic calorimeter was next, located about 4.6 m downstream of Rosie. It consisted of an array of glass blocks (Main Array) stacked on a table to form a wall perpendicular to the beam direction. An active converter was positioned in front of the Main Array. Its central part was occupied by a Lead Gas Chamber (LGC) which consisted of layers of lead sheets and aluminum extrusion tubes, each tube having a wire stretched along it. The two sides of the LGC were occupied by an array of glass bars positioned vertically (Active Converter). The position of the showers was measured in the central region by the LGC while in the wings was measured by a Gas Tube Hodoscope (GTH), consisting of two planes of plastic tubes with wires stretched inside them. The GTH was positioned between the Active Converter and the Main Array.

Finally, the muon detector consisted of four planes of scintillation counters, one set of horizontal counters and three vertical, positioned 11.16 m (MUY), 11.81 m (MU1), 12.72 m (MU2) and 14.36 m (MU3) downstream of Rosie. Between the calorimeter and MUY there were 40.64 cm of Cu and 309.88 cm of steel to absorb the hadrons while letting

through the muons. Another 60.96 cm of steel followed, between the MU1 and MU2, and 91.44 cm of concrete between MU2 and MU3. The total thickness of the hadron absorber was about 27 absorption lengths.

In the next sections the elements of the spectrometer and their electronics are described in more detail.

FERMILAB HIGH INTENSITY LAB SPECTROMETER
E705

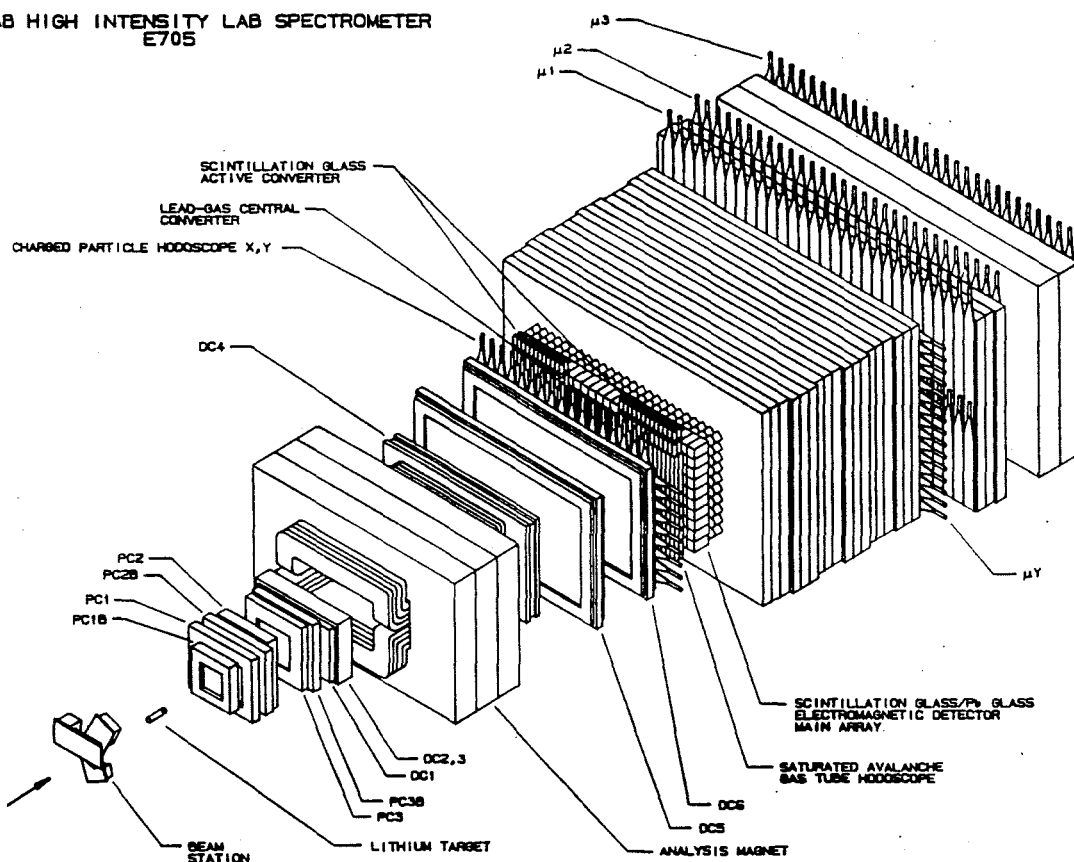


Figure 2.3 The E705 spectrometer.

2. 4 The beam chambers, beam and veto counters

The beam trajectories upstream of the target were determined by using a set of proportional chambers, referred to as Beam Chambers.

The beam chambers were part of the beamline and gave a profile of the beam hitting the target. The characteristics of the BC's are shown in table 2-1. The Y planes of the BC's have their wires stretched across the x-axis. The angle θ_{xy} is the angle between the wires and the horizontal x-axis.

The signals were recorded by a home built readout system.

Another component of the beam tracking and triggering was represented by the beam and veto counters. Upstream of the target there were three sets (beam stations BY1, BY2 and BY3), consisting of 8 scintillation counters each, positioned parallel to the x-axis and with a width gradually increasing from the center to the sides, to equalize the rate of beam particles seen by each counter. Each BY set covered $13 \times 13 \text{ cm}^2$. The veto walls VX and VY consisted of 22 and 16 scintillation counters and covered an area of $408 \times 147 \text{ cm}^2$ and $306 \times 153 \text{ cm}^2$ respectively. The VX counters were positioned parallel to the y-axis while the VY counters were positioned parallel to the x-axis. Each wall had a hole in the middle, $25.4 \times 8.8 \text{ cm}^2$ for VX and $8.8 \times 25.4 \text{ cm}^2$ for VY. The purpose of the veto walls was to signal the presence of a halo muon.

TABLE 2-1 Beam chambers. All lengths in cm, angles in rad.

Chamber	Plane	Nr of wires	Z-position	Spacing	Length	θ_{xy}
BC1	Y	128	-6714.6348	0.1000	12.70	0.0000
	U	128	-6729.8748	0.1000	6.35	-1.0472
	V	128	-6722.2548	0.1000	6.35	1.0472
BC2	Y	128	-4260.3801	0.1000	12.70	0.0000
	U	128	-4252.7601	0.1000	6.35	-1.0472
	V	128	-4245.1401	0.1000	6.35	1.0472
BC3	Y	128	-1029.5941	0.1000	12.70	0.0000
	U	128	-1021.9741	0.1000	6.35	-1.0472
	V	128	-1014.3541	0.1000	6.35	1.0472

2.5 The Target

The target was a cylinder of ^7Li , 33 cm long and 5 cm in radius. The choice of ^7Li as a target came from the following set of considerations:

- It is nearly an isoscalar target. That is, it has about the same amount of protons and neutrons.

- It has a favorable ratio of interaction to radiation lengths. Interaction length, λ , and radiation length, X_0 , represent respectively the probability for a hadron to interact in the target or for an electron to radiate a high energy photon (related to the probability for a photon to convert to an e^+e^- pair). In the case of Lithium, one has $\lambda=188.13$ cm (for 300 GeV/c pions) and $X_0=155$ cm, which, for a 33 cm target, correspond to 16% probability for an interaction and 15.2% probability for a conversion.

- It is a solid at room temperature and easy to handle.

2.6 The Multiwire Proportional chambers.

The proportional chambers were part of the tracking system between the target and the analysis magnet. They consisted of three planes each (four in the case of PC1), referred to as X, V, U according to the angle, θ_{xy} , of the wires with the vertical y-axis. The wires were made from tungsten and had a diameter of approximately 12, 20, 20 μm for PC1, 2 and 3 respectively. The chambers ran with a conventional "magic gas" mixture of 70% argon, 29.6% isobutane and 0.4% freon. Their characteristics (number of wires, position on z-axis, spacing, length of wires and orientation angle) are shown in table 2-2.

The chambers had their central regions de-sensitized to minimize the high occupancy rate due to the beam. The dead area was a circle of radius 5.08 cm for PC1 and 2 and 6.35

cm for PC3. The deadening was accomplished by electroplating the wires with a solution of CuS and doubling their diameter according to the formula :

$$Ah = F \times A \times T$$

where Ah are the Ampere-hours required, F is a factor characteristic of the plating solution, A is the area of the surface to be plated and T is the thickness of deposit desired. The electric field around a wire is inversely proportional to the radius of the wire. Therefore, by doubling the radius of the wire, the electric field is decreased by a factor of two. Three more proportional chambers (PCB) of fine wire spacing^[26] were used to cover the deadened area of the upstream chambers.

The signal of every wire was amplified by a commercial (Nanometric company) N-277D amplifier and then was recorded by a N-278 latch. The PCBs were readout with "Sippach" latches of the same type as the ones used for the beam chambers.

2.7 The analysis magnet (Rosie)

The analysis magnet was a large aperture (182 x 91 cm²) dipole magnet. The field integral along the beam line was determined to be 25.55 KG·m which corresponds to a transverse momentum "kick" of 0.776 GeV/c.

To reduce the fringe field downstream of the magnet, in the calorimeter area, an iron "mirror plate", 22 cm thick, was mounted at the downstream end of Rosie.

2.8 The Drift chambers

The drift chambers were part of the upstream and downstream tracking systems. There were three drift chambers (DC1, DC2 and DC3) upstream of Rosie, and three (DC4, DC5, and DC6) downstream .

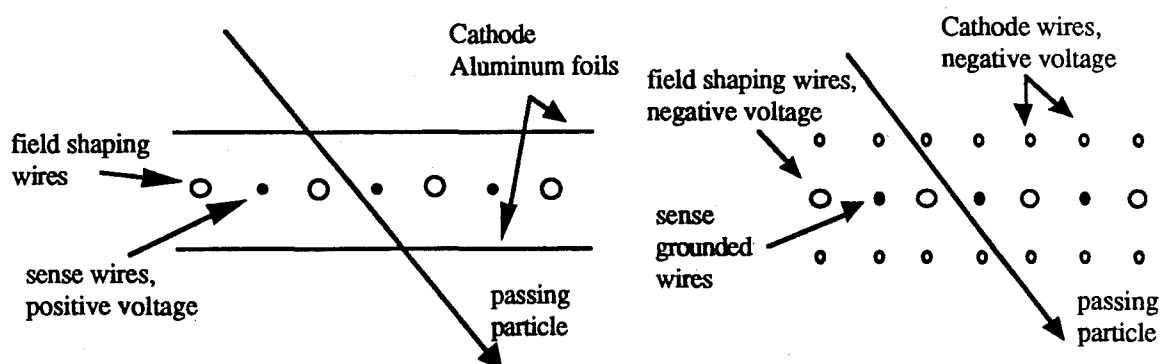


Figure 2.4 The two types of drift chambers.

The DC2-4 chambers consisted of three or four planes of parallel stretched anode (sense) wires at positive voltage alternating with field shaping grounded wires, sandwiched between cathode aluminum foils, also at ground. The other drift chambers had cathode wire planes, at negative voltage (like the field shaping wires), while the sense wires were grounded (fig. 2.4). The signal from each wire was amplified and converted to ECL by the LeCroy 7790 amplifiers and then sent to a LeCroy Time-to-Digital Converter (TDC) which recorded the drift time, which is proportional to the distance of the passing particle from the nearest anode wire. All the chambers were filled with a mixture of 50/50 Argon-Ethane.

The drift chambers, like the proportional ones, had a deadened region in the center. For the upstream chambers it was a circle of radius 6.35 cm and for the downstream a rectangle of 30.48 x 15.24 cm². The drift chamber characteristics are shown in table 2-3.

2.9 The charged particle hodoscopes

The two charged particle hodoscopes CPX and CPY consisted of 184 vertical and 48 horizontal scintillation counters respectively.

TABLE 2-2 Characteristics of Multiwire Proportional Chambers.

Chamber	Plane	Nr of wires	Z-position(cm)	Spacing (cm)	Length (cm)	θ_{xy} (rad)
PCB1	V	176	-427.7970	0.0850	30.0	-0.4899
	X	176	-427.1975	0.0750	30.0	0.0000
	U	176	-426.5955	0.0850	30.0	0.4899
PC1	P	352	-406.4254	0.1514	29.0	0.0000
	V	348	-405.1554	0.1581	29.0	-0.2915
	X	352	-403.8854	0.1514	29.0	0.0000
	U	349	-402.6154	0.1581	29.0	0.2915
PCB2	V	176	-380.5428	0.0850	40.0	-0.4899
	X	176	-379.9434	0.0750	40.0	0.0000
	U	176	-379.3414	0.0850	40.0	0.4899
PC2	U	480	-334.9600	0.1588	39.4	0.2915
	X	480	-333.6900	0.1507	39.4	0.0000
	V	480	-332.4200	0.1588	39.4	-0.2915
PC3	V	512	-266.7991	0.2088	50.0	-0.2915
	X	512	-265.5799	0.2000	50.0	0.0000
	U	512	-264.3607	0.2088	50.0	0.2915
	V	160	-244.9398	0.1133	50.0	-0.4899
	X	160	-244.3404	0.1000	50.0	0.0000
	U	160	-243.7384	0.1133	50.0	0.4899

TABLE 2-3 Characteristics of Drift Chambers. All lengths in cm, angles in rad.

Chamber	Plane	Nr of wires	Z-position	Spacing	Length	θ_{xy}
DC1	U	192	-216.3521	0.600	50.80	0.2915
	X	192	-215.7171	0.600	50.80	0.0000
	V	192	-215.0821	0.600	50.80	-0.2915
DC2	V	92	-194.8307	1.270	49.80	-0.2915
	X	93	-193.5607	1.270	49.80	0.0000
	U	93	-192.2907	1.270	49.80	0.2918
DC3	U	93	-180.8607	1.270	50.80	0.2915
	X	92	-179.5907	1.270	50.80	0.0000
	V	92	-178.3207	1.270	50.80	-0.2915
DC4	V	124	171.9910	1.905	99.06	-0.2915
	X	124	173.8960	1.905	99.06	0.0000
	U	123	175.8010	1.905	99.06	0.2915
	P	123	177.7060	1.905	99.06	0.0000
DC5	P	176	273.8806	1.905	167.64	0.0000
	V	192	275.7856	1.905	167.64	-0.2915
	X	176	277.6906	1.905	167.64	0.0000
	U	192	279.5956	1.905	167.64	0.2915
DC6	P	176	378.5895	1.905	167.64	0.0000
	V	192	380.4945	1.905	167.64	-0.2915
	X	176	382.3995	1.905	167.64	0.0000
	U	192	384.3045	1.905	167.64	0.2915

These hodoscopes had two purposes: first, to provide fast signals in order to be used in a fast multiplicity trigger, and second, to be used as verification points for the track reconstruction in order to remove false combination of hits. The CPY and CPX were located 417.15 cm and 423.18 cm downstream of the center of Rosie. The CPY counters were arranged in two columns of 24 counters each. Their dimensions were 1 cm thick, 7.5 cm wide and 200 cm long, resulting in a $400 \times 180 \text{ cm}^2$ wall with a $30 \times 15 \text{ cm}^2$ hole around the beam line. The CPX counters were arranged in two rows of 92 counters each. They were 1 cm thick, 3.8 cm wide and 100 cm long, resulting in a $350 \times 200 \text{ cm}^2$ wall with a $30 \times 15 \text{ cm}^2$ hole around the beam line.

2.10 The Main Array

The Main Array (figure 2.5) was the major component of the electromagnetic calorimeter. It consisted of 392 scintillation and lead glass blocks covering an area of $371 \times 195 \text{ cm}^2$. The blocks were arranged to leave a $30 \times 15 \text{ cm}^2$ hole in the center in order to avoid interactions of very energetic hadrons, produced at small angles with respect to the beam.

The scintillation glass blocks were Ohara Optical SCG1-C and they covered the central area of the detector (shaded area in figure 2.5). Two different sizes of blocks, the smaller blocks being installed in the most busy region of the detector; their cross sections were $7.5 \times 7.5 \text{ cm}^2$ and $15 \times 15 \text{ cm}^2$ respectively; their length was 89 cm, corresponding to 20.5 radiation lengths.

The lead glass blocks were SF5 and surrounded the scintillation glass blocks. Their cross section was $15 \times 15 \text{ cm}^2$ and their length was 41.45 cm, corresponding to 18 radiation lengths. The SCG1-C and SF5 properties are shown in table 2-4.

E705 ELECTROMAGNETIC CALORIMETER

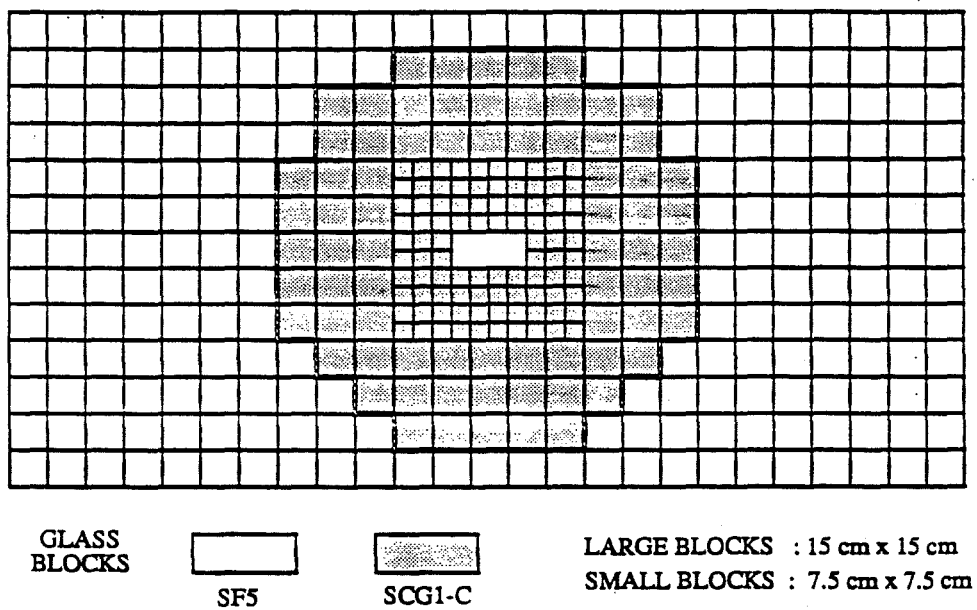


Figure 2.5 The Main Array.

TABLE 2-4 Properties of SCG1-C scintillation and SF5 lead glass.

	SCG1-C		SF5	
Composition (by weight)	BaO	43.4%	PbO	55%
	SiO ₂	42.5%	SiO ₂	38%
	Li ₂ O	4.0%	K ₂ O	5%
	MgO	3.3%	Na ₂ O	1%
	K ₂ O	3.3%		
	Al ₂ O ₃	2.0%		
	Ce ₂ O ₃	1.5%		
Density	3.36 g/cm ³		4.08 g/cm ³	
Radiation Length	4.25 cm		2.47 cm	
Absorption Length (for 30-200 GeV π 's)	45.6 cm		42.0 cm	

The mixture of scintillation and lead glass blocks represented a compromise between energy resolution and financial limitation. In lead glass light represents Cerenkov radiation produced by relativistic shower electrons and positrons. Compared to scintillating glass, lead glass has a more favorable ratio of radiation length to interaction length. Thus, for a given number of radiation lengths, there is a smaller probability for a hadron to interact in the lead glass. On the other hand, lead glass has two serious drawbacks. First, it is more vulnerable to radiation damage, which results in a darkening of the glass and a consequent degradation of the energy resolution. Second, the energy resolution is limited by the amount of light generated, which is rather small. These reasons lead to the choice of the more expensive scintillation glass. The SCG1-C is more resistant to radiation damage (about 150 times more than the SF5) which makes it unique for the high intensity region of the detector around the beam hole. Moreover, the amount of light produced in the SCG1-C is 5 times larger than in

the SF5, since in addition to the Cerenkov light there is also scintillation light due to the Ce_2O_3 scintillator. This in principle results in better energy resolution than for SF5 glass.

The calorimeter rested on a table inside a climate controlled house, whose temperature was kept constant within $\pm 0.06^\circ \text{C}$. The whole house could move up-down, left-right, so every Main Array block could be centered on the beam. The table could be run either locally or remotely via CAMAC.

The large blocks and small glass blocks were read out by EMI 9791KB and RCA 6342A photomultipliers respectively, which were attached to their back faces. The high voltage to the photomultipliers was supplied by LeCroy 1440 power supplies. Signals originating from the glass array/phototube system were carried by RG-8 cables, 200 nsec long, to the inputs of custom made Precision Charge Cards, where the charge was integrated and sent to ADCs and to TDCs, as described in more detail in the next sections.

2.10.1 The Precision Charge cards

The precision Charge Amplifier/ADC cards^[27] were specially made for E705 in order to perform in high rates and to cover a large dynamic range of energies with high accuracy.

Each card consisted of 16 channels continuously integrating the input signals. The charge pulses from the glass block phototubes entered the cards from their back panels and were split into high and low frequency components in order to prevent the low frequency noise from contributing at the integration-shaping stage. The high frequency component was amplified and integrated by a resistor-capacitor circuit. The values of the capacitors were chosen in a way to optimize the energy range digitized by the ADCs. The integrated pulses went to multi-tap delay lines, where a copy of the signal was delayed by 160 nsec and subtracted from the originals in differentiating amplifiers, transforming the integrated levels into square pulses. Two copies of these pulses were produced, one being sent to the Cluster Finder trigger (see section 3.3), the other to LeCroy 4290 TDCs.

Another copy of the pulses was delayed by 400 nsec to wait for trigger decision, and then was sent to the digitization section of the cards. There, the voltage pulse charged two sample-and-hold capacitors C1 and C2 via two JFET switches. When a trigger occurred, one switch opened, just before the signal of interest appeared at the delay line output, so that the C1 voltage level reflected the state of the charge integrating amplifier output just "before" the event of interest was integrated. The other switch then opened 250 nsec later, so that the voltage on C2 reflected the state of the integrator output "after" the interaction of the event of interest. A differential amplifier then subtracted the "before" from the "after" level. In this way, the tails of previously occurring pulses were properly subtracted.

After subtraction, the resulted pulses were sent to a single 5200 Analog Devices 12-bit ADC. Before reaching the ADC they were amplified by a factor of 8 if the level was such that the digitized value would have been less than $1/8$ of the full scale, or by 1 otherwise. This provided an effective sensitivity of 15-bits, increasing the maximum range to 32760 counts. The voltage level of capacitor C1 was also digitized in 3 bits, giving information about the "before" state of the charge integrating amplifier. A 16-bit word was formed by the 12 bits of the digitized difference, the 3 "before" bits, and one bit set to 1 when the analog output had been multiplied by 8. The digitized values for the 16 channels were then sent to a FIFO to await read-out through CAMAC.

2.10.2 The TDC system

The signals from the front output of the Charge Cards were sent to a LeCroy 4290 TDC system. The TDCs operated in a common stop mode, using the ADC signals as a start and the trigger pulse as a stop. The TDCs were used to identify glass blocks with energy deposition not associated with the interaction of interest.

2.10.3 LED pulser system

The gains of the photomultiplier tubes were monitored with a light pulser system. The light source consisted of an array of 96 green Hewlett Packard HLMP-3950 light emitting diodes (LED). Optical filters were used to vary the light intensity from 0-100%. Bundles of optical fibers brought the light from the LED array to the glass blocks. For the Main Array blocks, each fiber was attached to the block surface opposite to the photomultiplier, while for the active converter blocks it was mounted in the middle of the block. Three Litronix BPX 66 PIN diodes were used to monitor the LED light level.

The pulser was operated during the run of the experiment at about a 2 Hz rate.

2.11 The photon converter

The photon converter was located in front of the Main Array and it was used to initiate the electromagnetic showers, so that the shower centroids could be measured in the tube hodoscopes. The converter also gave useful information on the longitudinal development of the shower which was used as a basis for rejecting hadrons.

The converter consisted of three parts: a central region covered by a Lead Gas Chamber (LGC) and two outer regions covering the left and right sides and made from vertically stacked SCG1-C scintillation glass blocks (Active Converter). Figure 2.6 shows the top view of the calorimeter, the main array and the active converters.

The next sections give a description of the two converters.

2.11.1 The Active Converter (AC)

The Active Converter consisted of two layers of vertically arranged SCG1-C scintillation glass blocks as shown in figure 2.7. Each block had a cross section of 7.5 x 7.5

cm² and was 97.5 cm long. An RCA 6342A photomultiplier was mounted on the free end of each block. The signals from the phototubes were sent to the Charge Cards for charge integration and digitization.

2.11.2 The Lead Gas Chamber (LGC)

The LGC^[28] was an 8-layered sampling device with each sampling section consisting of 1.2 mm lead, 10 mm aluminum extrusion proportional tubes, copper-clad horizontal strips, and 1.6 mm fiberglass board. A 1.3 cm sheet of steel, followed by 8 mm of lead were positioned in front of the whole LGC assembly. The total thickness of the device, which spanned an area of 1.03 x 1.95 m², was 4.2 radiation lengths. A 30 x 15 cm² hole in the center matched the hole of the Main Array.

The LGC was used both as an active converter and as a shower position detector. The x-coordinate was given by the proportional tubes and the y by a copper-clad printed circuit board of horizontal strips, picking up capacitively the signals in the tubes.

There were two planes of tubes: a top and a bottom, each having 104 tubes. Each tube had a 50 micron gold-plated W wire stretched inside it, biased at about 1850 volts. The wire-to-wire spacing was 9.92 mm. The gas inside the tubes was a mixture of 50/50 Argon Ethane.

The cathode strips were 1.25 cm wide and they were arranged in two groups. The boundaries of these two groups are indicated in figure 2.7 by the "S" shaped line.

The eight wires at the same x position and at different depths were ganged together, as were the eight corresponding strips. The wire and strip signals were brought by RG8 coaxial cables to LeCroy 2280 ADCs. Pedestals were subtracted on-line, and only clusters of channels above a preset threshold were written to tape.

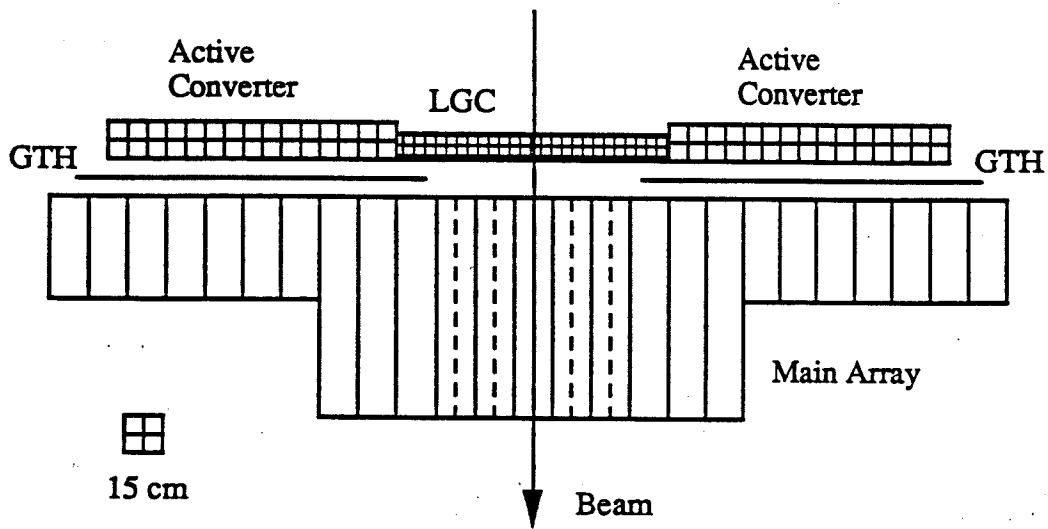


Figure 2.6 Top view of the calorimeter.

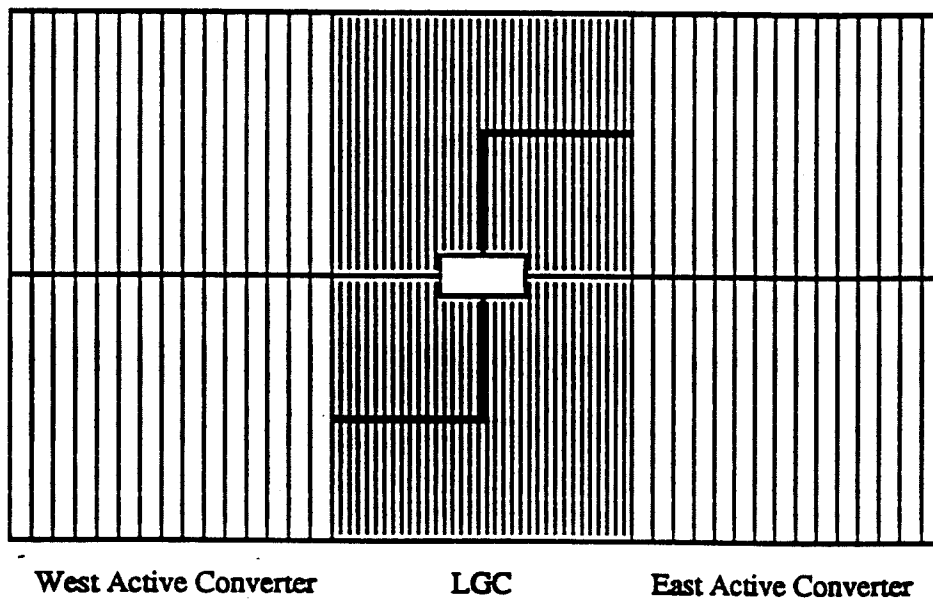


Figure 2.7 Front view of the active converter.

The choice of the relative dimensions of the LGC and the Active Converter was made to balance two conflicting factors: the energy resolution of the calorimeter and the ease of pattern recognition. Being a sampling device, the LGC has worse resolution than the Active Converter. On the other hand, the larger segmentation of the glass blocks of the Active Converter increases the probability for two showers to hit the same block, particularly at the center of the detector. The choice of the LGC as a central device solves the problem of segmentation, while offering an acceptable degradation of the energy resolution, since the central region is hit by more energetic photons for which energy resolution is less critical. In addition, the LGC provides a better hadron rejection because of the shorter absorption length, a factor which is particularly important in the central region of the calorimeter.

2.12 The Gas Tube Hodoscope (GTH)

The Gas Tube Hodoscope^[29] was built to determine the position of the electromagnetic showers in the region not covered by the LGC.

The GTH consisted of two panels $156 \times 197 \text{ cm}^2$ each, positioned at the two sides of the LGC and in the space between the Active Converter and the Main Array (figure 2.6). Each panel had a 10 cm overlap with the LGC, and consisted of two planes of 216 conducting polystyrene tubes, vertically arranged and sandwiched between three sheets of 1.6 mm copper-clad G-10. The outer two copper layers, adjacent to the tube planes, were etched into horizontal strips 0.86 cm wide and served as a y read-out. The tubes were of single and double width, with a wire stretched along their center, set at a 2100 volts positive voltage. The wire-to-wire spacing was respectively 0.88 cm and 1.76 cm for the single and double width tubes. The boundary between the single and double width tubes was at $\pm 85 \text{ cm}$ from the center of the calorimeter. The tubes were filled with a gas mixture of 50/50 Argon/Ethane.

The two layers of tubes were ganged together, as were the two layers of strips. The signals were carried by RG8 cables to LeCroy 2280 ADCs.

2.13 The Muon detector

The muon detector followed the calorimeter and consisted of four planes of scintillation counters, positioned within three shields of copper, steel and concrete.

The MUY and MU1 planes were located behind the first shield. The MUY consisted of 96 horizontally arranged counters in four columns of 24 counters each, covering a total area of $620 \times 285 \text{ cm}^2$, with a $40.6 \times 40.6 \text{ cm}^2$ hole in the center. The dimensions of the counters were $129 \times 13 \text{ cm}^2$ for the inner columns and $187 \times 13 \text{ cm}^2$ for the outer, with 1 cm thickness. The MU1 plane consisted of 60 counters vertically arranged in two rows of 30 counters each, covering a total area of $618 \times 290 \text{ cm}^2$ with a $40.6 \times 40.6 \text{ cm}^2$ hole in the center. Each counter was $20.3 \times 145 \times 1 \text{ cm}^3$.

The MU2 and MU3 planes were located behind the second and third shield respectively. They consisted of 62 counters each, vertically arranged in two rows of 31 counters. The MU2 covered an area of $671 \times 315 \text{ cm}^2$, with a $40.6 \times 40.6 \text{ cm}^2$ hole in the center. Each counter was $23 \times 157 \times 1 \text{ cm}^3$. The MU3 covered an area of $723 \times 352 \text{ cm}^2$ with a $87.6 \times 40.6 \text{ cm}^2$ hole in the center. Each counter was $26.7 \times 176 \times 1 \text{ cm}^3$.

2.14 The Data Acquisition system

The data acquisition system of E705 is shown in figure 2.8.

The data was collected from the electronics by "Smart" Crate Controllers, which resided in standard CAMAC crates. The Controllers were designed specially for the experiment^[30] in order to achieve a high data collection rate. The Controllers executed lists

of special instructions in order to initialize, read and clear the modules that resided in their crates. The lists were loaded into the controllers from a VAX 11/780 computer via RS-232 lines.

The data from the controllers was sent to a VME-bus based system, containing a set of ACP (Fermilab Advanced Computer Project) modules, a Motorola 68020-based computers with 2 megabytes of memory. The ACP's were responsible for assembling together into a single event the data arriving in parallel from the smart crate controllers, and then store it in their memory until it was recorded to magnetic tapes.

From the VME-crate the data was sent to a PDP 11/44 computer via a CAMAC branch highway. The PDP wrote the data to tapes loaded on two tape drives. At the peak of running conditions a tape was written every 10 minutes. A fraction of events was also transferred from the VME-crate to the VAX. These events were accessed by monitoring programs that were checking the various devices during the data taking.

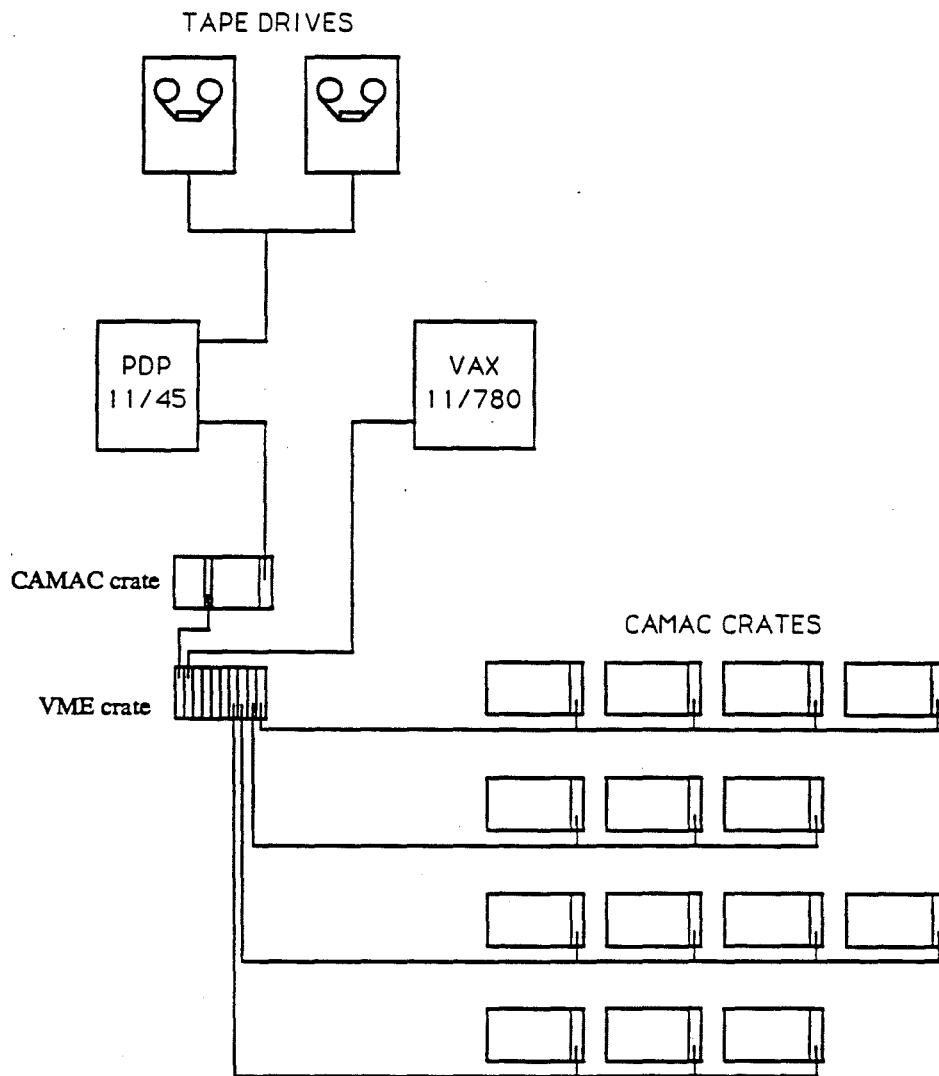


Figure 2.8 The data acquisition system.

Chapter 3

Triggering

3.1 General

During the process of data taking, in order to select only the interactions of interest and reduce the number of the events recorded to tape, special logics (triggers) were setup using fast electronics. The triggers used during the run of the experiment were:

- a) **The interaction trigger** (also called Cluster Finder strobe) which ensured that an interaction occurred in the target as a result of a pion or a proton from the beam.
- b) **The dimuon trigger**^[31] which was used to study events with heavy particles decaying to two muons. It was formed using the muon counter planes MU1, MU2, MU3 (first level) identifying events with two muons in two different quadrants of these planes. Then a trigger processor^[32] selected events for which the invariant mass of the two muons was greater than $2.4 \text{ GeV}/c^2$.
- c) **The photon trigger** which was used to select direct photon production. It first reconstructed the transverse energy of the showers in the glass calorimeter and then it selected events having showers of transverse energy greater than three different thresholds PT2, PT3 and PT4, resulting in three independent triggers.

d) **The diphoton trigger** which was used to study production of two prompt photons. It selected events with two high transverse energy showers in two opposite quadrants of the calorimeter.

e) **The two-vee trigger** which was used to select events with two "vee" decays occurring between PC2 and PC3.

f) **The LED trigger** which was used to track the gains of the glass blocks. It was active during the off-spill period, collecting events with the LED pulser.

Of the above triggers, the dimuon and the PT4 were the ones setup to accomplish the primary goals of E705. At the running beam rate of 6 MHz, these two triggers caused only 5% dead-time in the Data Acquisition system, so that more triggers, properly prescaled, could be added to study some secondary physics goals (diphoton, two "vee") as well as to bring information on the performance and the systematics of the detector (PT2, Interaction, LED). As the beam rate varied during the run, the prescaling factors were adjusted to keep the rate of dimuon and PT4 events to tape to the maximum, while maintaining the dead-time below the desired limit of 20%.

TABLE 3-1. Percentage of various triggers recorded to tape.

Trigger type	% to tape	Prescaling factor
Interaction (C.F.Strobe)	0.6	524288
Dimuon	78.0	1
Single photon PT2	2.2	512
Single photon PT3	4.4	8
Single photon PT4	4.0	1
Diphoton	10.2	8
Two Vee	0.6	256

The percentage of the various triggers that were recorded to tape for the part of the run corresponding to the data presented here is shown in table 3-1.

3.2 The Interaction Trigger

The interaction trigger was defined as the coincidence of a beam particle with at least two hits from the CPX hodoscope plane. A beam particle was defined in the following way:

The discriminated pulses from the BYi counters, set to a width of 10 nsec, were both ORed and summed together (fig. 3.1) to form six pulses, named BY1-BY3 and Σ BY1- Σ BY3 correspondingly. The BY1-3 signals were sent to an AND gate in coincidence with a T1 pulse, defining a beam particle. The requirement of the four pulses in coincidence was necessary to ensure the presence of a valid beam particle, following the proper beam trajectory. The resulting pulse was vetoed by HALO to form a useful beam particle (B). The vetoing was done to exclude interactions with an accompanying halo muon. The HALO pulse was defined as the coincidence of the two veto planes.

Due to the beam structure of the accelerator (see section 2.2), the secondary beam, could have more than one particles within a bucket. The multiple particle buckets had higher probability than the single particle to interact in the target which could cause errors in the normalization, if the interactions associated with these buckets were not removed from the data sample. To keep the useful beam rate as high as possible, only buckets with more than two particles were rejected and a normalization correction was done off-line to take into account the cases of double occupancy (see Normalization in chapter 7).

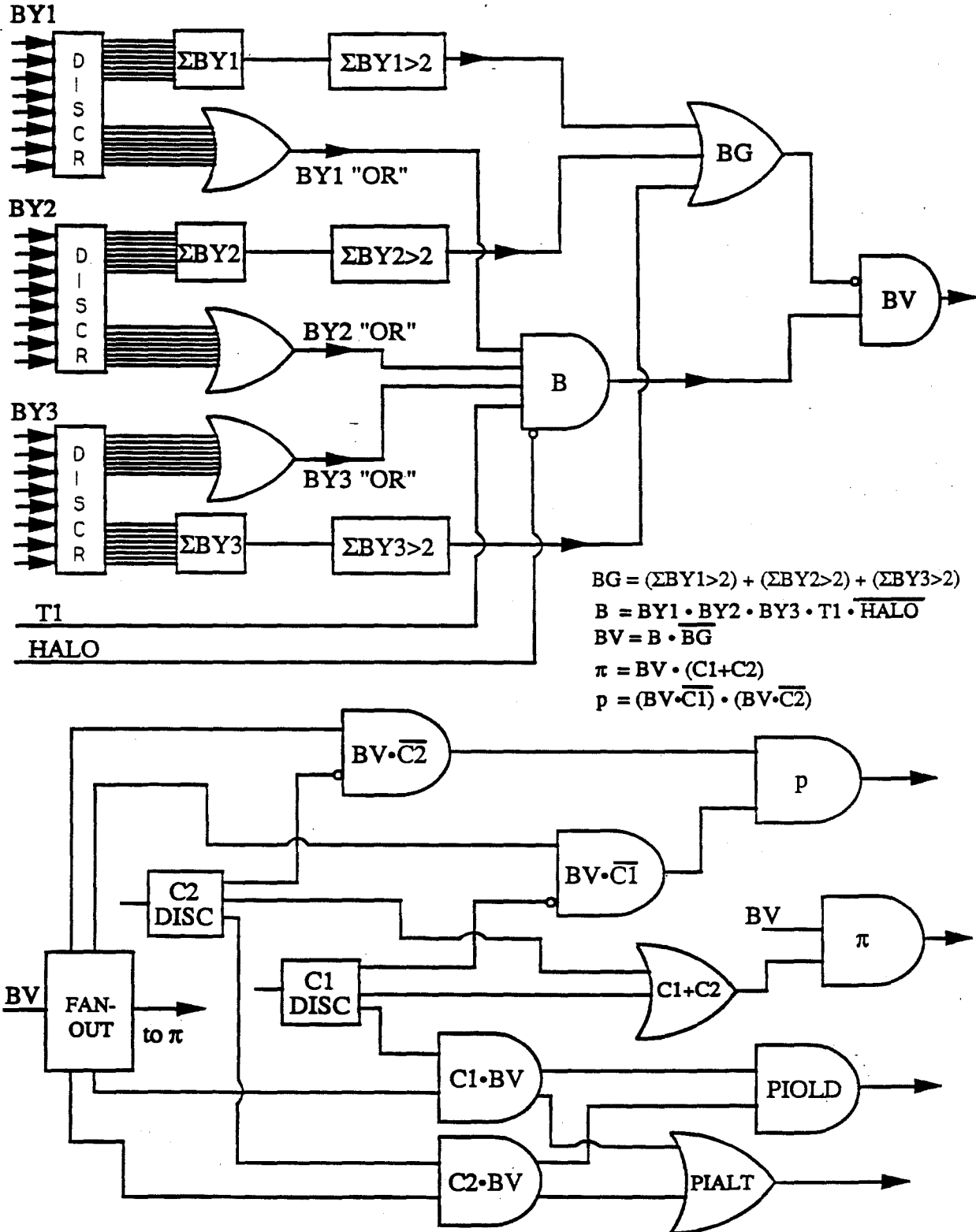


Figure 3.1 The beam logic. Pion and proton definitions.

The rejection of the unwanted buckets was done in the following way: The ΣBY_i pulses were sent to discriminators with thresholds set to select more than 2 particles. The discriminator outputs were ORed to form the BG pulse which then vetoed the beam pulse B, to produce the signal BV.

The next step was to identify the beam particle. The two Cerenkov counters were set to give pulses only when a particle with velocity β greater than a threshold β_T went through them. The threshold, adjusted by varying the gas pressure in the counters, corresponded, for fixed momentum $p=300$ GeV/c, to a mass threshold according to the formula:

$$m_T = p \frac{\sqrt{1 - \beta_T^2}}{\beta_T}$$

Thus, for the given momentum, the Cerenkov counters gave light only for particles with mass less than the threshold, which was set just below the proton mass. This procedure misidentified some kaons in the beam as pions, causing a contamination of the π signal. The fraction of non identified kaons was estimated to be about 10% of the number of positive pions^[33], which required a correction in the normalizations (see Normalization in chapter 7). Due to the special nature of the negative beam, the negative pions were minimally contaminated. The signals of the two Cerenkovs C1 and C2 passed through discriminators and the output pulses were ANDed with BV to define the identity of the beam particle. A pion was defined as the coincidence of a beam particle with at least one of the two Cerenkovs, while the proton was defined as the anticoincidence of BV with both Cerenkovs. In parallel the signals from the CPX counters were summed and the result was sent to a discriminator with a threshold set to two hits. The output of the discriminator was then sent to an AND gate, in coincidence with the pion or the proton signal, resulting in the interaction trigger.

In the first part of the run, the pion definition was stricter, requiring both Cerenkovs to be set (PIOLD, figure 3.1). The efficiencies of the Cerenkov counters were defined as the ratios of the following scaled quantities:

$$\varepsilon_1 = \frac{BV \cdot C1 \cdot C2}{BV \cdot C2} \quad \varepsilon_2 = \frac{BV \cdot C1 \cdot C2}{BV \cdot C1}$$

and they were measured to be 0.92 for C1 and 0.90 for C2. Since in the beginning of the run the pion was defined as $BV \cdot C1 \cdot C2$, the total efficiency of finding a pion was determined by the product of the individual Cerenkov efficiencies ($0.92 \times 0.90 = 0.828$) which resulted in a 17% loss of the pion sample. Therefore the pion definition was changed to $BV \cdot (C1 + C2)$, which gave a total inefficiency of $0.08 \times 0.1 = 0.008$ and increased the accepted pion rate. For a consistency check of the electronics, the OR of the individual coincidences of each Cerenkov with the BV was also scaled (PIALT). The data presented here were taken with the less strict definition of the pion.

At about 6 MHz beam rate, the halo rate was in average 2.8 MHz for the negative and 2 MHz for the positive beam. However the effect of the halo veto on the negative and positive beams resulted in a reduction of 9.15% and 8.7% respectively, since the presence of a halo beam particle was uncorrelated. The $\Sigma BY_i > 2$ veto condition caused an additional reduction of 3.4% for both beams. The measured unvetoes beam rate (particles/sec) for the negative and positive parts of the run are shown as a function of the tape number in figure 3.2. The resulting interaction rate (after the vetoes) is also shown in the same figure.

3.3 The Photon Trigger (the Cluster Finder)

3.3.1 General

The Cluster Finder was a fast trigger, built to select events containing photons with high transverse energies by using the information from the glass calorimeter. The term transverse momentum (p_T) is being used hereafter instead of transverse energy, since the particles of interest are photons, for which $p_T = E_T$.

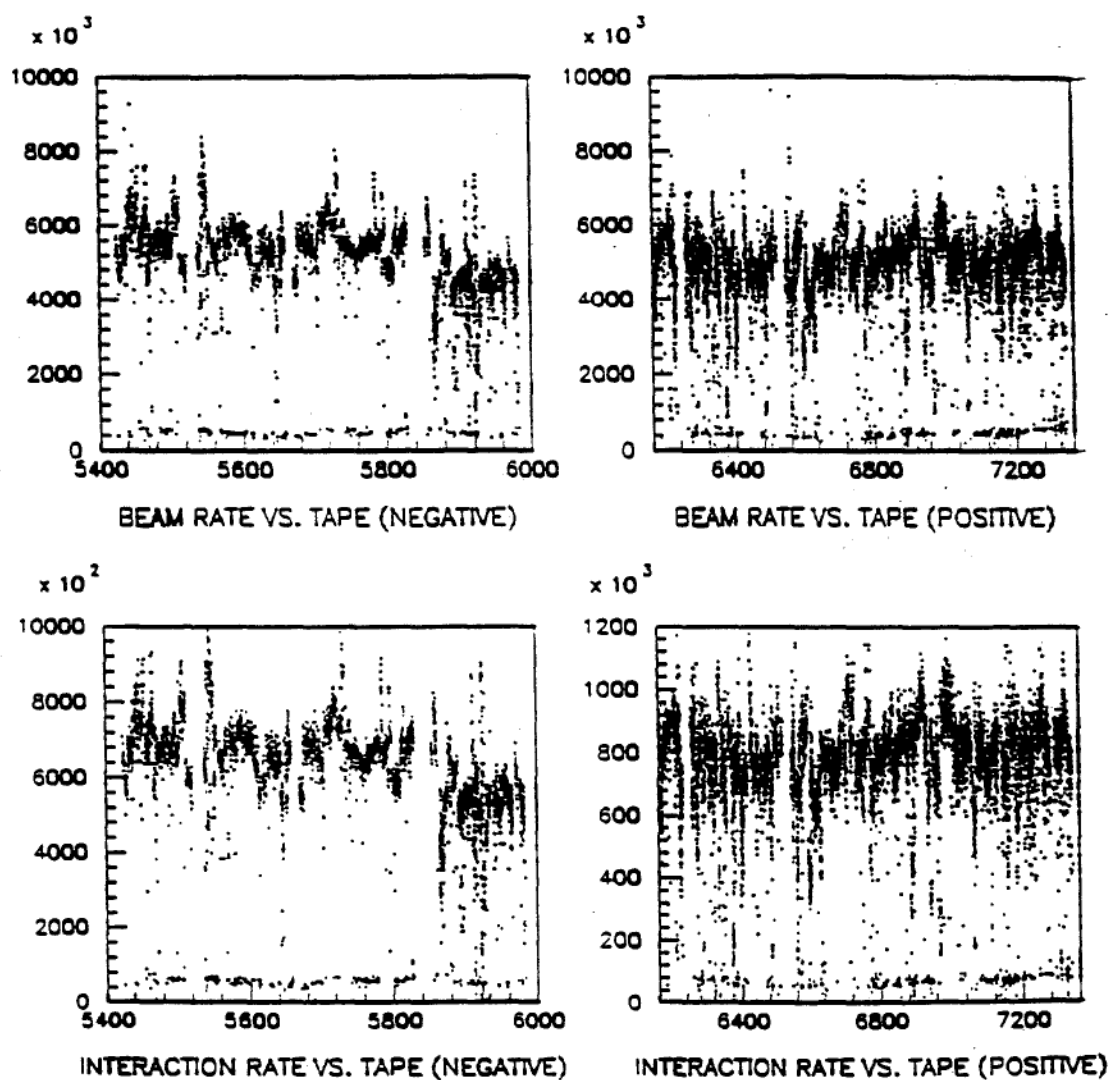


Figure 3.2 Beam and Interaction rates (particles/sec) as a function of the tape number.

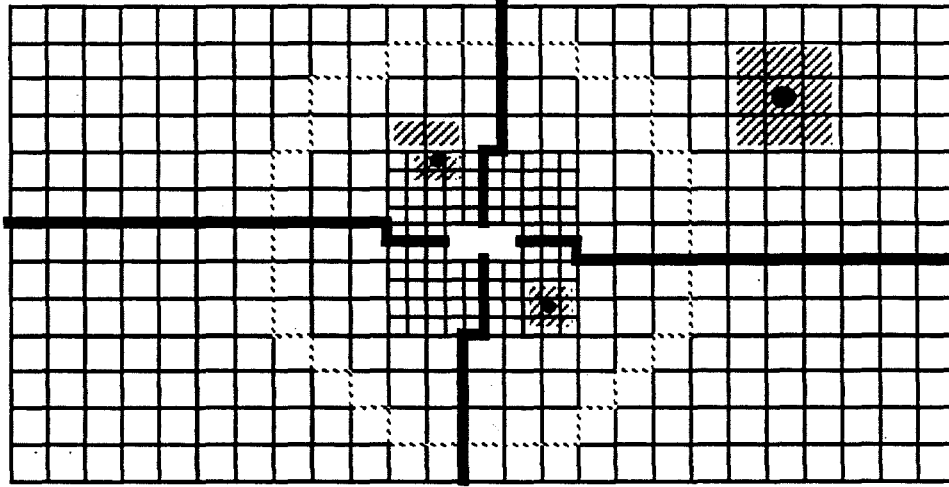


Figure 3.3 Cluster definition in the Main Array. The black dots are the peaks of the clusters (hatched areas) and the thick black lines the boundaries of the four quadrants.

In the Cluster Finder, the information from all the blocks was processed in parallel within an event; events were processed in a pipeline mode as they occurred. The p_T trigger was formed in three steps:

a) Cluster Finding

A *cluster* was defined as a pattern of energy deposition in a set of blocks satisfying the following criteria: the central block would not be an edge block (next to the hole or in the outer layer of the calorimeter) and the energy measured in this block would be greater than that measured in any of its neighbors, and also greater than a common noise rejection threshold, set at 25 mVolts (about 4 GeV). In such a case, the block was called a "Peak and Over Threshold" (POT) block. Figure 3.3 shows such clusters in different regions of the main array. The number of blocks in a cluster could vary from 7 to 10.

b) Energy Summation and P_T Conversion

The energies of all the blocks in a cluster with a POT block were added together and the sum was multiplied by a scaling factor in order to be converted to transverse energy

($=P_T$). This factor depended on the position of the cluster's central block, and was equal to the sine of the angle between the beam and the center of the block, as seen from the center of the target (figure 3.4).

c) Trigger Decision

The P_T of the cluster was compared to each of four thresholds (set to 1.7, 2.5, 3.5, 4.5 GeV/c respectively) and the results, in coincidence with an interaction trigger, formed four trigger levels P_{T1} , P_{T2} , P_{T3} , P_{T4} . The four levels were formed separately in the four quadrants (whose boundaries are noted in figure 3.3 with thick lines) and were then ORed together to form four P_T trigger signals, which were sent to the final steps of the trigger logics.

A diphoton trigger was also formed as the coincidence of two P_{T1} (or higher level) triggers from two opposite quadrants.

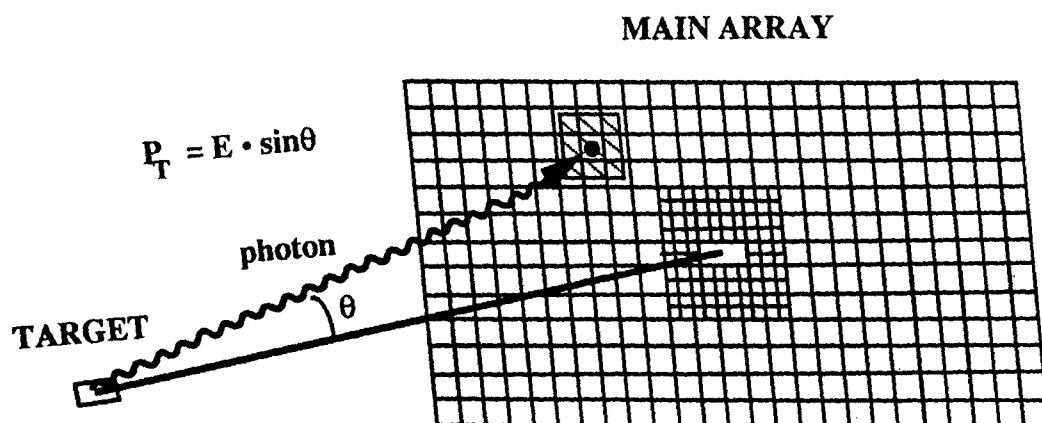


Figure 3.4 Energy to transverse momentum conversion.

3.3.2 Functional Description and Implementation^[34]

Figure 3.5 shows a schematic diagram of the modules and connections that formed the p_T trigger.

The 392 individual signals originating from the glass array/phototube system were carried by RG-8 cables, 53.5m long, to the inputs of charge integrating precision ADC cards. These cards provided analog pulses of 200 nsec duration and with an amplitude proportional to the charge integral of the input signals.

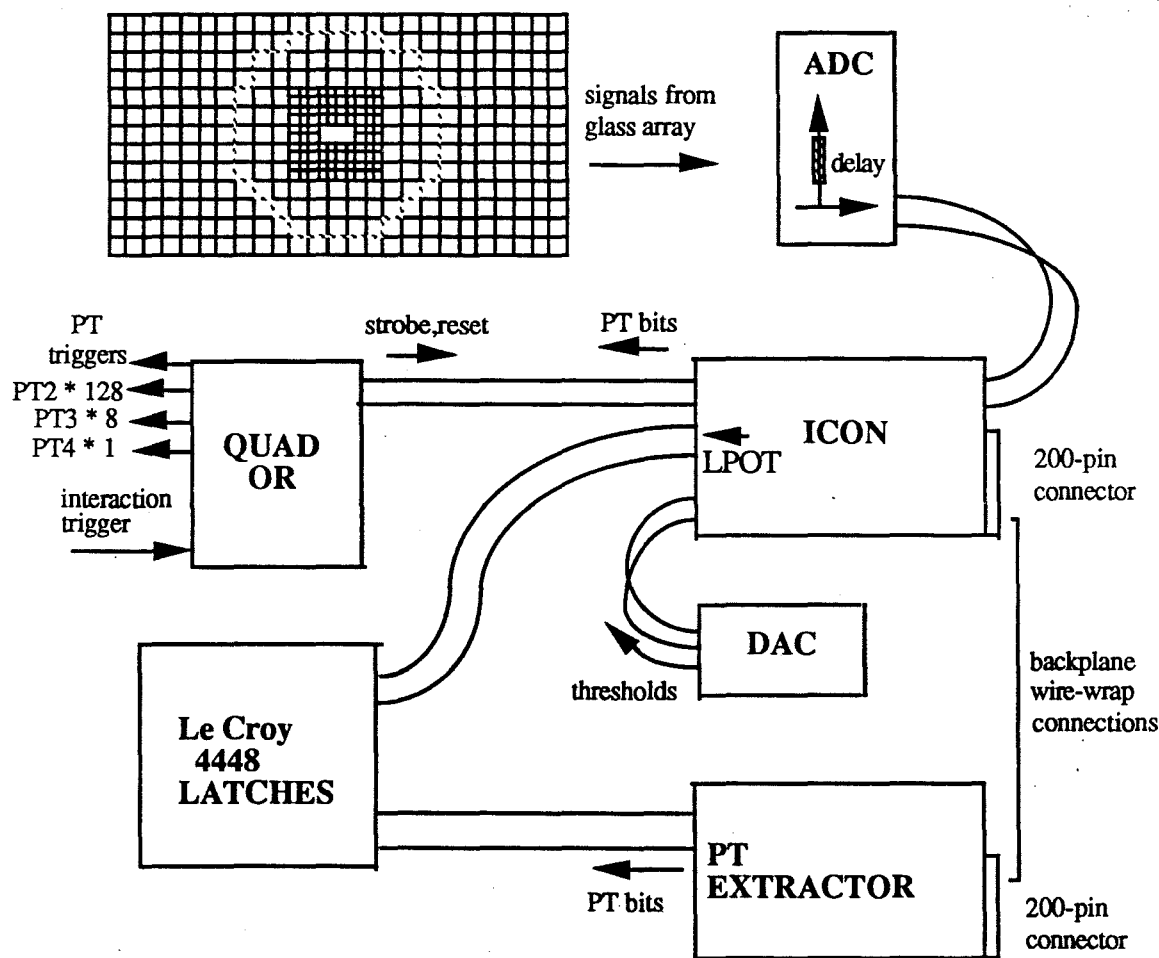


Figure 3.5 Schematic diagram of modules and connections of the Cluster Finder trigger.

Each integrated pulse was sent to the appropriate channel of an interconnected system of 54 ICON ("interconnective") modules, where it was input as a central signal and "exported" to other channels, to serve as a neighbor signal.

Every ICON module had eight channels, each of which was assigned to one block of the Main Array. These ICON modules resided in four custom made crates and were organized in four groups, corresponding to the four quadrants of the Main Array. All channels were processed in parallel in order to decide if they were POT channels, to sum their energies with the energies of their neighbors, to convert the total energies to transverse momenta, and to compare those with the four thresholds.

For each channel, the four bits resulting from these comparisons were latched by the interaction strobe and then fed simultaneously into the trigger pathway and (through backplane connections) the four P_T EXTRACTOR modules which collected the p_T information of every channel. The latched p_T bits were ORed with the corresponding bits of the other channels of each ICON module and the results were in turn ORed with all the other ICONs assigned to a detector quadrant. A ribbon cable, acting as a wire OR bus, was used for this purpose, and also brought the interaction strobe and the reset to the ICON modules.

The four OR cables from the four quadrants were sent to the trigger logic which was implemented in the QUAD OR module. In this module, the bits of the same p_T of the four quadrants were ORed together, in order to form the triggers which selected events with photons of transverse momentum greater than the four corresponding thresholds. In addition, all the P_{T1} bits of every two opposite quadrants were also ANDed and the results were ORed in order to form the diphoton trigger, which selected events with two photons of p_T greater than 1.7 GeV/c (P_{T1} threshold).

For monitoring purposes, the p_T information from the P_T EXTRACTOR modules was sent to LeCroy 4448 latches in order to be recorded among the event information. For the same purposes, a cluster flag bit (Latched Peak and Over Threshold, or LPOT) of each channel was also sent to another set of latches.

3.3.3 ICON Circuit

The ICON module processed signals that arrived via an 8-channel coaxial ribbon cable from a corresponding ADC card. These eight lines formed the inputs to eight Precision Monolithics BUF-03 buffers that drove the signal distribution on the large wire-wrapped backplane of the custom crates. On this backplane each channel was connected to neighbor channels via a network of wire-wrap connections. The assignment of channels was such that each board handled signals from pairs of neighboring blocks. The eight channels per card thus came as four channel pairs. This minimized the necessary number of wire-wrap connections.

All the signals from the ADC cards were input to the ICON modules via a 200-pin AMP connector whose mated connector was part of the backplane. The signals of the central block and its neighbors, within every cluster, were then parallel processed by both an interchannel comparison circuit and a summation Operational Amplifier (fig.3.6). The interchannel comparison circuitry sought to find if the signal of the central channel was above all of its neighbors (up to a maximum of nine) and above a Common Peak Threshold (CPT) DC signal that acted as noise rejector. LeCroy MVL407 quad comparators were used for this purpose. To AND the ten comparators (9 neighbors + 1 threshold) together, the ten low true outputs were wired together to form a low true ECL wire AND. This signal was called POT (Peak and Over Threshold).

At the same time, the central block and its neighbor signals were summed by a Harris 2539 Op Amp using ten $7.5\text{ K}\Omega$ summing input resistors and a $6.81\text{ K}\Omega$ feedback resistor. The summing circuitry, shown in figure 3.7, fed its output to a $2\text{ K}\Omega$ load (PT HEADER). The $2\text{ K}\Omega$ output load was part of the next stage processing, the conversion of energy to transverse momentum. The sum formed by the Op Amp was proportional to the energy deposited in the detector block and its neighbors. Conversion to transverse momentum

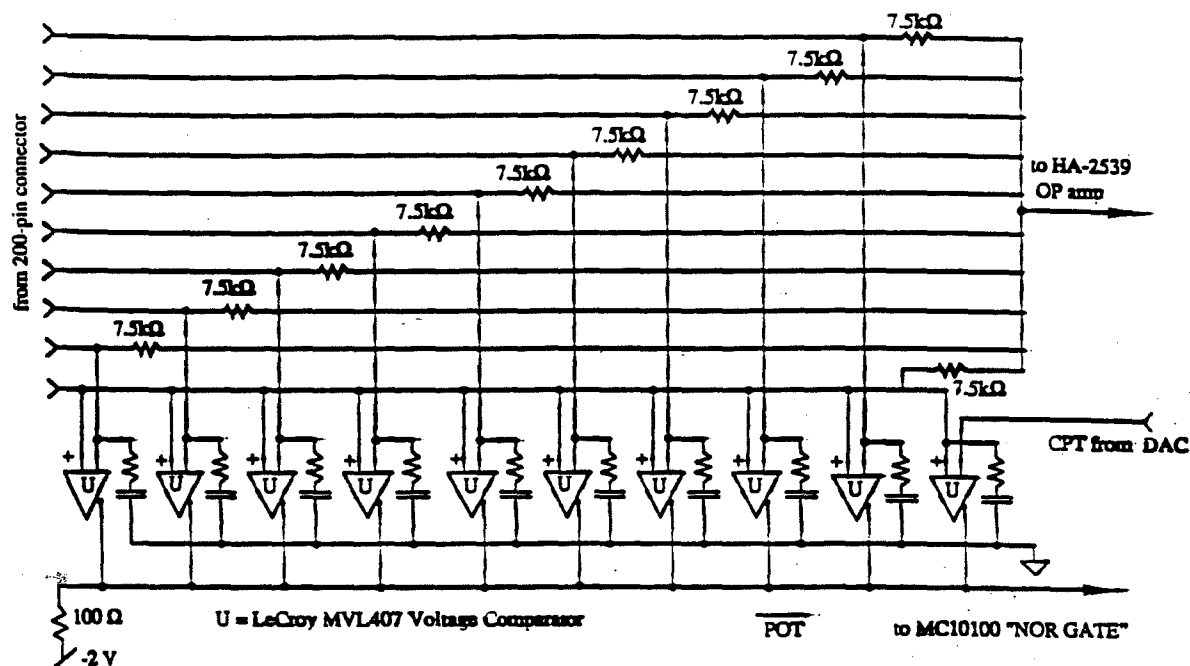


Figure 3.6 Interchannel comparison circuit and summation resistors

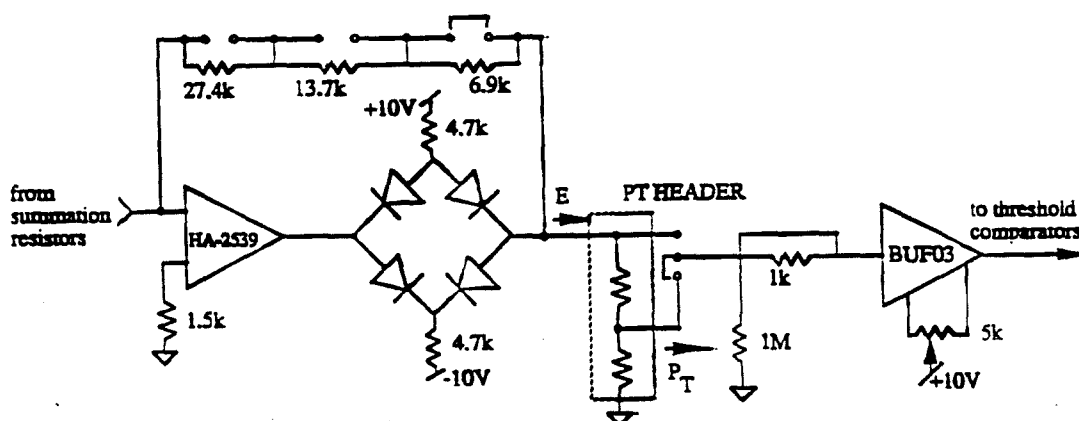


Figure 3.7 Summing, energy to transverse momentum conversion, and DC offset cancelling circuits

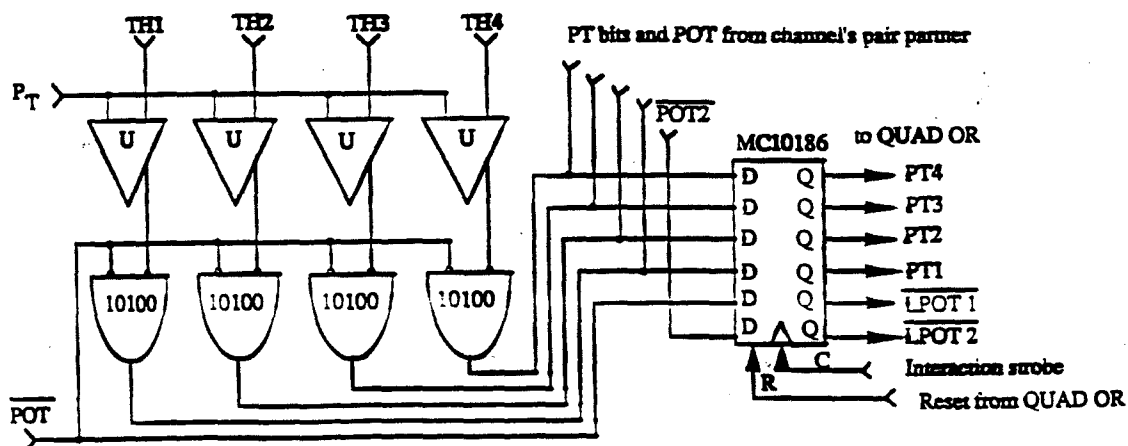


Figure 3.8 P_T threshold comparison and P_T bits latching circuits

meant multiplication by $\sin\theta$ (fig. 3.4), where θ is the angle between the beam and the line connecting the center of the block with the center of the target. The $2\text{ K}\Omega$ load was a voltage divider, whose output was the input voltage times a factor equal to $\sin\theta/\sin\theta_{\max}$, where θ_{\max} was the angle between the beam and the center of the farthest trigger block, as seen from the target's center. The two resistors of the voltage divider were on an 8-pin Augat DIP header and their values varied from channel to channel. As a result, each ICON card was unique. The E to p_T conversion was optional; a jumper on each channel selected between the voltage divided and undivided signal. This option of accessing the raw energy data made it easier to debug the system.

Next, the p_T signals came to a BUF-03 which drove the p_T threshold comparators. The BUF-03 was connected to an offset canceling circuit, in order to adjust the DC offsets that could appear at the output of the buffer in every channel.

The p_T pulses then went to four LeCroy MVL407 comparators (fig.3.8), where they were compared with four DC levels (labeled TH1 through TH4) corresponding to the four p_T thresholds. The p_T and the CPT thresholds were derived from a 12 bit CAMAC DAC module, which was set by the host computer, and were sent to the ICON modules through a common bus.

The result pulses of the comparisons were sent to a set of four MC10100 NOR gates, which were acting as low true input AND gates. Each gate had another input which was common to the four gates of the MC10100. This common input was connected to POT, so that a gate would only fire if the corresponding ten cluster identifying comparators had found that this gate's channel was a POT channel.

At this point, each of the four AND outputs of the channel were ORed with the corresponding outputs of the channel's paired partner. As previously described in the first paragraph of this section, only adjacent detector blocks were members of a channel pair. Thus, only one member could assert POT.

Since every signal to the Cluster Finder could give a p_T trigger by crossing one of the thresholds, a selection had to be made in order to accept only the signals associated with interactions in the target. For this purpose, the four p_T bits and the two POT lines of the channel pair were sent to an MC10186 hex latch. The strobe to this latch was a copy of the interaction trigger and it set a level, which was reset by a CLEAR. The CLEAR was a delayed copy of the strobe. The circuit that defined the strobe and the reset (fig.3.9) introduced 94 nsec dead time for every strobe to the system. This resulted in inhibiting some of the triggers associated with interactions that occurred close in time. The leading edge of the strobe was timed to coincide with the midpoint of the p_T bit pulses. All four 10186s per ICON were driven from an MC10188 digital buffer that received the strobe and the reset from a ribbon cable bus going to a 20-pin connector on the front of each ICON.

The 16 latched P_T bits (4 thresholds x 4 quadrants) were distributed to four PT EXTRACTOR modules and to a set of MC10109 OR gates at the front of the ICON card. Each of these four gates ORed the four bits of a particular p_T threshold, producing four Fast Trigger output lines. These lines went out the 20-pin connector, from which the latch strobe and reset were input, to the QUAD OR module where they formed the four p_T and the Diphoton triggers, previously described.

The total time to form the trigger, as determined from the peak of the analog pulse leaving the precision ADC cards to the leading edge of the p_T trigger pulse at the output of the ICON card, was of the order of 85 nsec.

3.3.4 DAC Calibration

As previously mentioned, all thresholds - i.e. PT1, PT2, PT3, PT4 - were set by a Digital to Analog Converter module (DAC). The calibration of the DAC was done by using an electron beam of 30 GeV/c momentum. To this purpose the table on which the glass resided was moved to position the beam onto the centers of different blocks, chosen

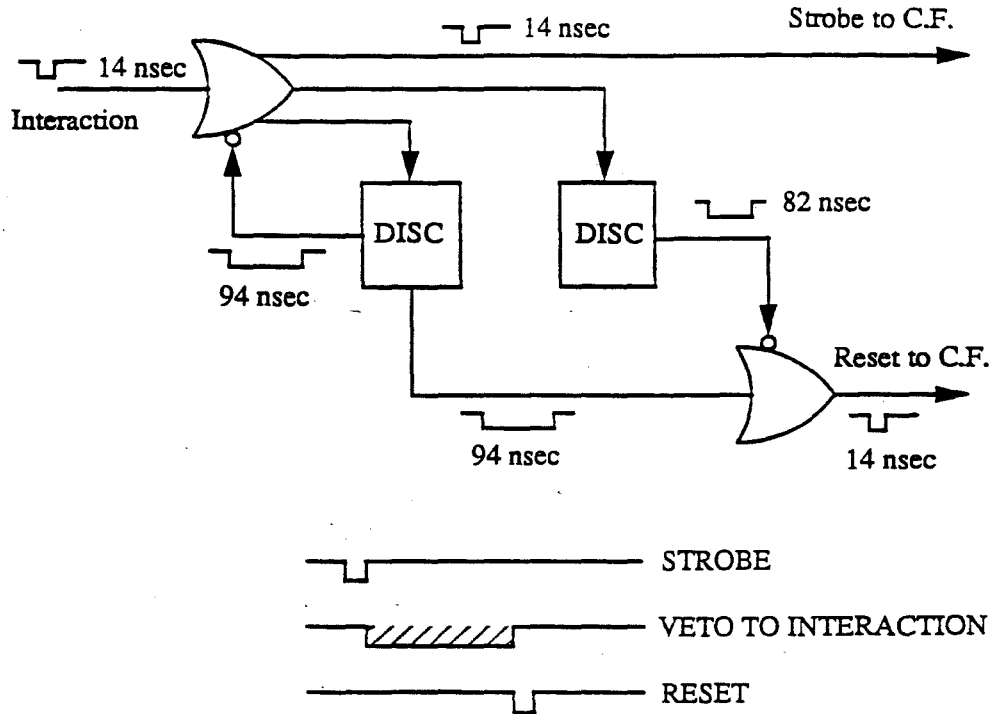


Figure 3.9 Cluster Finder strobe and reset logic.

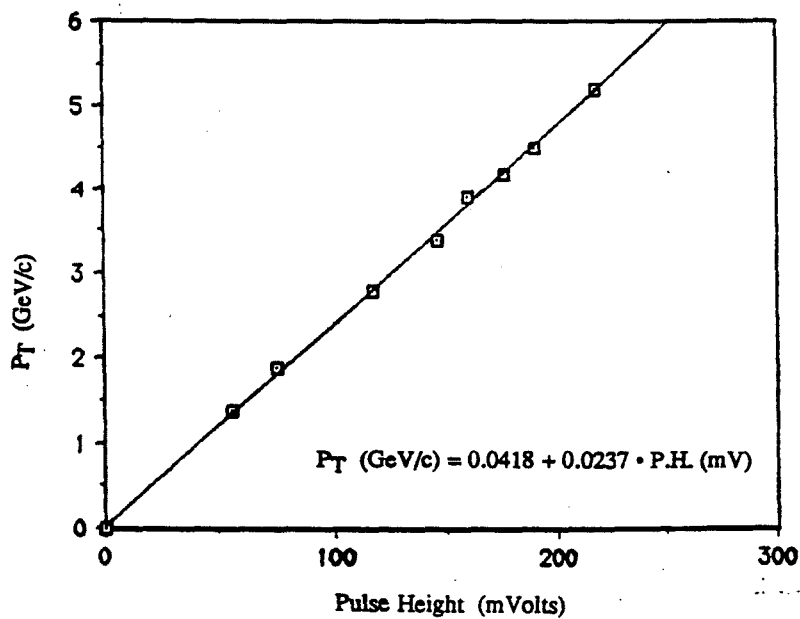


Figure 3.10 Digital to Analog Converter calibration.

in a way that the corresponding channels of the cluster finder would see different values of p_T in the interval between 0 and 6 GeV/c. For every block, the maximum value of the threshold (in mV) that let through the corresponding p_T trigger was recorded. The threshold in GeV/c versus the Pulse Height in mVolts was plotted and fitted to a straight line (figure 3.10) with the result:

$$p_T \text{ (GeV/c)} = 0.0418 + 0.0237 \cdot \text{P.H. (mV)}$$

In a similar way the correspondence between the Common Peak Threshold and pulse height was also measured and found to be:

$$\text{CPT (GeV)} = 0.0742 + 0.152 \cdot \text{P.H. (mV)}$$

The noise level in the various channels throughout the cluster finder was of the order of 10 mV, which corresponds to 280 MeV/c error in the transverse momentum threshold.

3.3.5 Monitoring

The Cluster Finder trigger processor was first used in a preliminary run in 1985 and was in full operation during the major run of E-705 which took place from July 1987 to February 1988. The data analyzed in this thesis correspond to the period from December 1987 to the end of the run.

During its operation, it was monitored by an on-line FORTRAN program which was a software simulation of the Cluster Finder. This program read the digitized signals from the precision ADC cards and the 4448 latches carrying the LPOT and p_T bits. It converted the ADC counts of each channel to energy, formed clusters in the same way as the Cluster Finder, converted their energies to transverse momenta, and compared these values with the four p_T thresholds, forming a four-bit word for every cluster. By combining the information of the LPOT and p_T latches, the program could also find which cluster hardware asserted

what p_T . Thus, the monitor could check if the hardware and software clusters as well as their asserted P_T bits were in agreement.

The suppression factors of the raw interaction rate achieved by the 3 p_T levels (PT2,PT3,PT4) and the diphoton trigger during the run were of the order of 2.5×10^{-3} , 1.2×10^{-4} , 1.1×10^{-5} and 4.5×10^{-4} respectively. Only the three highest level thresholds were used in the data acquisition, while the PT1 was only used to define the diphoton trigger. The prescaling factors for the four triggers are shown in table 3-1.

3.3.6 Trigger efficiency

The trigger efficiency was calculated using the raw p_T distributions of the triggering cluster, as they were found from the software simulation of the Cluster Finder. The distributions were measured for the largest transverse energy cluster in the events of the three photon triggers and the minimum bias (interaction) trigger. The gains of the glass blocks were corrected for drifting with time, using the LED triggers (see next chapter on calibration).

The timing of the cluster finder was very important, thus only events with the triggering cluster in time with the interaction were considered for the calculation of the trigger efficiency. The time information recorded from the TDC of each block of the triggering cluster was required to be within 10 nsec from the actual time that the event occurred, in order to remove triggers coming from pile up of interactions or from the beam halo (see Out of Time Background in chapter 5).

The trigger efficiency was calculated for different beam types and different time intervals of the run, whenever a change in the thresholds or a change in the prescalings or a change in the voltages of the glass block phototubes occurred. For the part of the run that was analyzed here, the data were divided in three eras corresponding to negative beam with

PT2 prescaling equal to 128, negative beam with PT2 prescaling equal to 512 and positive beam with PT2 prescaling equal to 512; the trigger efficiency was calculated for each era separately.

As mentioned in chapter 1, the most interesting events for the study of direct photons are the events with $p_T \geq 4$ GeV/c. Thus only the PT3 and PT4 triggers were used in the extraction of the signal while the PT2 was used to define the efficiency of the two higher trigger levels. All the trigger levels were set inclusively, i.e. if a PT3 trigger was set then the PT1, PT2 and the Interaction were also set. The trigger efficiency for a cluster of transverse momentum in the interval $[P_T, P_T + \Delta P_T]$ was defined as:

$$\varepsilon(P_T) = \frac{PT3 \cdot PR3 + PT4 \cdot PR4}{INTER \cdot PR + PT2 \cdot PR2 + PT3 \cdot PR3 + PT4 \cdot PR4} \quad (3.1)$$

where PT2, PT3, PT4 are the numbers of events of the three photon trigger types whose triggering cluster has transverse momentum in the interval being considered while the higher levels have not been set; PR2, PR3 and PR4 are their corresponding prescaling factors; INTER is the number of interaction triggers with the maximum transverse momentum cluster in the $[p_T, p_T + \Delta p_T]$ interval; PR is the interaction prescaling factor.

Figure 3.11 shows the raw p_T distributions of the triggering cluster for the sum of all four trigger types weighted by their prescaling factors (denominator of 3.1) and for the sum of PT3 and PT4 (numerator of 3.1). The ratio of the two distributions is shown in figure 3.12 for the negative and positive beam types. The errors in all plots are statistical. The function superimposed on the efficiency plots was estimated in the following way:

Assuming that the p_T seen by the cluster finder is given by the real p_T smeared by a Gaussian distribution with a variance σ , then the probability for an event with a cluster of given transverse energy P_T to pass the threshold τ will be:

$$P(P_T) = \int_{-\infty}^{\infty} dp_T^{SM} \theta[P_T + p_T^{SM} - \tau] \frac{e^{-\frac{p_T^{SM2}}{2\sigma^2}}}{\sqrt{2\pi}\sigma} \quad (3.2)$$

where $\theta(\xi)=1$ for $\xi>0$ and $\theta(\xi)=0$ for $\xi<0$, P_T is the mean transverse momentum and p_T^{SM} is the smearing of the transverse momentum as seen by the cluster finder. It follows:

$$P(P_T) = \int_{\tau-P_T}^{\infty} dp_T^{SM} \frac{e^{-\frac{p_T^{SM2}}{2\sigma^2}}}{\sqrt{2\pi}\sigma} \quad (3.3)$$

and by defining:

$$t = \frac{p_T^{SM}}{\sigma\sqrt{2}} \quad (3.4)$$

and substituting it in (3.3) we get

$$P(P_T) = \frac{1}{\sqrt{2\pi}\sigma} \sigma\sqrt{2} \int_{\frac{\tau-P_T}{\sigma\sqrt{2}}}^{\infty} dt e^{-t^2} = \frac{1}{2} \left\{ \frac{2}{\sqrt{\pi}} \int_{\frac{\tau-P_T}{\sigma\sqrt{2}}}^{\infty} dt e^{-t^2} \right\} \quad (3.5)$$

where the expression in the parenthesis is the error function.

The values for τ and for σ for the negative and positive beams were derived by fitting the error function to the data, and they were:

	<u>τ (GeV/c)</u>	<u>σ (GeV/c)</u>
negative	4.5	1.0
positive	4.7	1.0

The difference between the thresholds of the negative and the positive was due to a systematic drift of the phototube gains with time.

The calculated Cluster Finder efficiency is not necessarily the same as the trigger efficiency for pizeros and direct photons. The p_T of a photon shower can be smaller than the p_T of the corresponding cluster in the glass (because of additional energy from neighbor showers), and it also depends on the energy deposited in the active plane in front of the glass. The estimation of the trigger efficiency in the case of pizeros and single photons was done using the previously described measurement and both a Monte Carlo simulation and the data, and it is described in the next chapters.

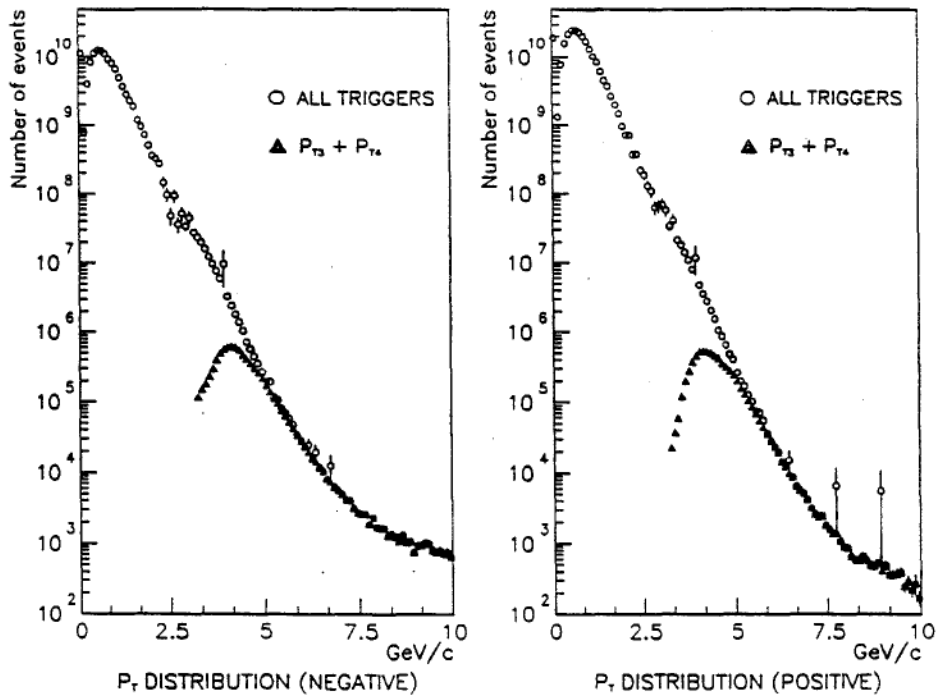


Figure 3.11 Raw P_T distributions as seen from the Cluster Finder.

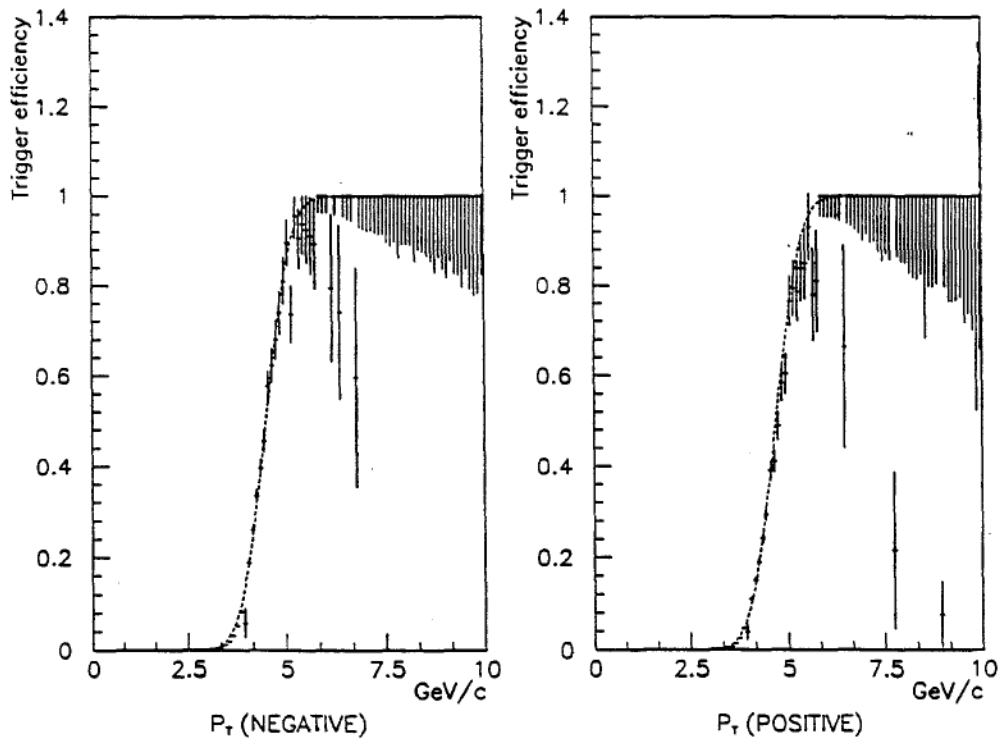


Figure 3.12 Trigger Efficiency for negative and positive data.

Chapter 4

Calibration and Event reconstruction

4.1 Introduction

The process of event reconstruction consisted of two separate steps: the electromagnetic shower reconstruction and the tracking. The former used the information from the calorimeter while the latter used the information from the proportional and drift chambers.

The calorimeter had to be calibrated before being used for measuring the energy and the position of the showers. In the first part of this chapter the calibration procedure is described, and the resulting energy and position resolutions are determined. A detailed description of the algorithm used to reconstruct the showers follows.

Only a short description of the tracking is given here, more details can be found in reference 31.

4.2 Calibration of the calorimeter

The calibration of the calorimeter was done with electron (and positron) beams of various energies specifically 2, 6, 10, 30, 60 and 100 GeV at about monthly intervals.

Figure 4.1 shows the energies of three of the beams as reconstructed from the calorimeter data following the procedure described below. A calibration run was performed sequentially centering each glass block on the electron beam. Every main array block in the LGC region and every active converter block in the GTH region was centered in front of the beam. The computerized horizontal and vertical motion of the table allowed to scan through the entire array in less than 6 hours per beam, recording to tape of about 1000 events for every main array block.

The calibration was done in two steps, one online (phototube voltage setting) and one offline (gain determination).

The high voltage in the phototubes was set with the 30 GeV electron beam in such a way that their analog pulses at the output of the ADC cards had all equal height, so that all the blocks presented the same signals to the Cluster Finder. The pulse heights were set to 100 mV for the large blocks and to 85 mV for the small blocks, in order to compensate for the lesser energy seen by the smaller area of the latter. The voltages were set with Rosie off and they were readjusted when the magnet was on to correct for the effect of the fringe magnetic field on the gains of the phototubes, which was as large as 20%. The adjustment was done comparing the magnet on/magnet off phototube response to the LED pulses. The pulse heights were adjusted before digitization inside the ADC modules, in order to set the absolute scale for the digitization in a way to optimize the following two factors: The ADC could measure a pulse height corresponding up to 32000 counts in the large scale (see section 2.11), so the smaller the gain of the photomultiplier, the higher could be the maximum measured pulse height (and therefore the deposited energy). The larger the gain, the better the resolution, because the effect of any noise in the system becomes minimum. The previous conditions are optimized if the gains are chosen as a function of the radial distance of each block from the center of the main array, since the average energy of the photons hitting the glass decreases with the distance from the beam. The array was then divided in three regions and the corresponding gains were set in accordance to:

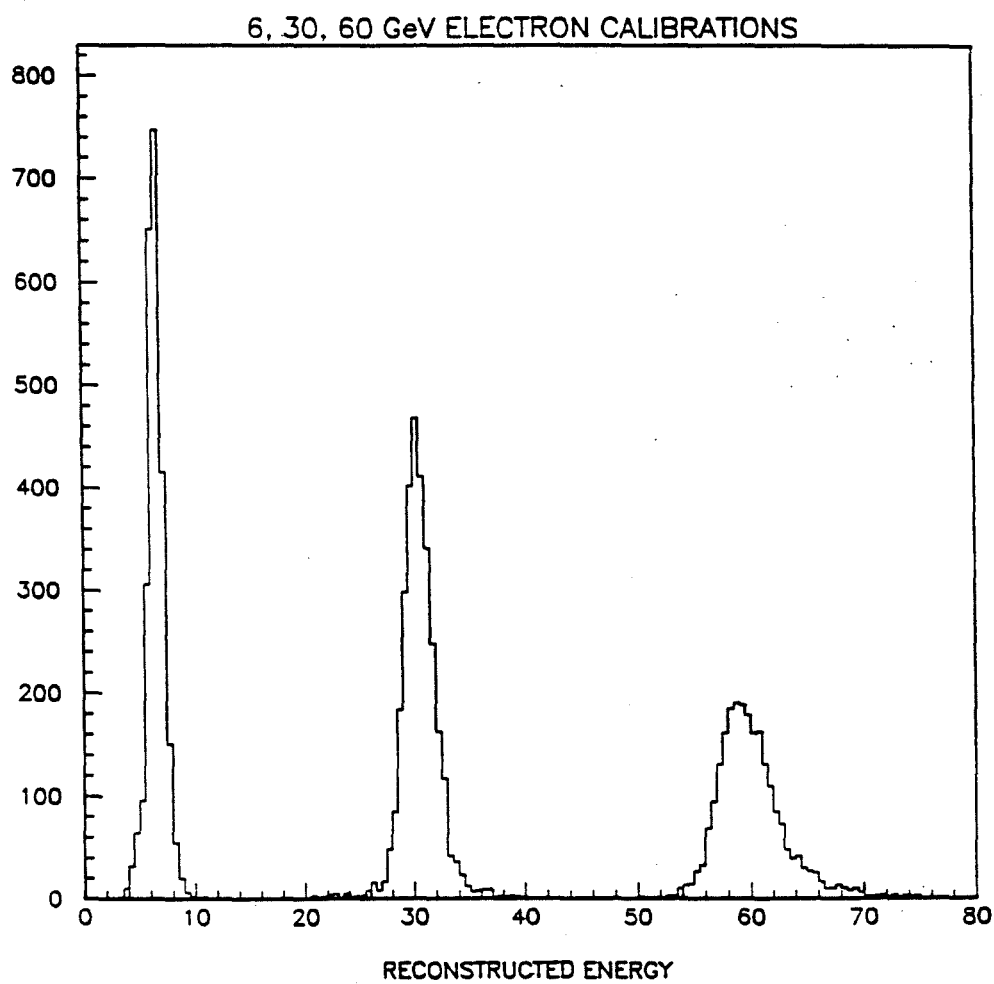


Figure 4.1 Energy distributions of electron beams as reconstructed from the calorimeter.
The vertical axis shows the number of events.

<u>Region</u>	<u>Energy / 32k counts</u>	
Small SCG1-C blocks	250 GeV	(8.3 MeV/count)
Large SCG1-C blocks	150 GeV	(5.0 MeV/count)
Large SF5 blocks	100 GeV	(3.3 MeV/count)

The off-line analysis of the data taken with the 30 GeV undeflected electron beam resulted in the more accurate determination of the gains of the three parts of the calorimeter. The off-line calibration procedure had as an objective the minimization of the width of the observed energy spectrum. For every position of the table the output of the calibration program determined the gain of the hit block in the main array and in the active plane. This was done by fitting the active and main array gain constants G for every hit block j and blocks k, l for front and back active converters in an iterative process, i.e. minimizing the quantity:

$$\chi_j^2 = \sum_{i=1}^{N_{ev}} (E_{beam} - E_{ma}^{side} - E_{ac}^{side} - G_{ma,j} P_{ma,j} - G_{ac,k} P_{ac,k} - G_{bc,l} P_{bc,l})^2$$

where E_{beam} is the beam energy, E_{ma}^{side} is the main array energy deposited in the neighbors of the hit block j , E_{ac}^{side} is the active converter energy deposited in the neighbors of the hit active converter blocks k, l (if any), $G_{ma,j}$, $P_{ma,j}$ are the gain and the pulse height for block j , $G_{ac,k}$, $P_{ac,k}$ are the gain and pulse height for the front converter block k and $G_{bc,l}$, $P_{bc,l}$ are the gain and pulse height for the back converter block l . The sum is over the number of the events N_{ev} recorded for the block j . For the situation where the block j was behind the LGC then the last two terms were replaced by the energy deposited in the LGC x tubes and the E_{ac}^{side} term is deleted. For every iteration only the gain of the hit block was determined, while the gains of the other blocks were given from the previous iteration. The nominal gains shown in the previous table were used in the first iteration.

In order to compute the energy deposited by the calibration electrons, the main array was divided in three regions, according to the type of converter encountered. If N is the

number of blocks in a cluster, defined in the same way as in the Cluster Finder, then the relation between the total energy E , the pulse heights P_i and the gains G_i is:

$$E = \sum_{i=1}^N G_i P_i$$

for the outer region, where there were no active converter blocks in front of the main array,

$$E = \sum_{i=1}^N G_i P_i + \sum_{a=1}^A G_a P_a + \sum_{b=1}^B G_b P_b$$

for the SCG1-C active converter region and

$$E = \sum_{i=1}^N G_i P_i + \sum_{l=1}^L G_l P_l$$

for the LGC region, where P_l are the corresponding pulse heights in the tubes in front of the shower and G_l the x gains. The number of blocks summed in the front (A) and in the back (B) active converter was 3. The number of LGC tubes (L) was 5.

In addition to the gains, a correction for the longitudinal development of the shower was also determined. The pulse height that was measured from the phototube viewing the glass block was determined by the light produced minus the light absorbed along the block. Consequently, the apparent energy measured was lower than the real energy deposited in the block, requiring a correction that depended on the z position at which the shower started. Having an active plane in front of the main array blocks, gave some information for the longitudinal shower development, which could be used to correct for the differential absorption. This was an advantage over other calorimeters without active converter, where there is no information about the "z-development" of the shower. It was found empirically that for this "z-correction" one could use:

$$E = E_{MA} + (1+b) E_{AC}$$

where E_{MA} , E_{AC} are the main array and active converter energies and b is a correction factor empirically determined for each main array block. The effect of the correction on the total spread in measured energies is shown in figures 4.2a (before correction) and 4.2b (after the

correction). The vertical axis is the energy measured by the active plane and the horizontal the total reconstructed energy. The uncorrected plot shows a tail towards the smaller energies for large depositions in the active plane (early starting shower). No active plane dependence can be seen on the corrected plot.

Another necessary correction, affecting the active converter block, was due to the attenuation along the block. To take into account this effect, the gains G_a of the active converter blocks were derived from the empirically determined equation:

$$E_{AC} = (D+D_0)^n G_a P_a$$

where D was the distance of the shower center from the phototube and D_0 and n were constants determined for each active converter block. To set the absolute scale of the active glass energy, it was required that the average active energy be equal to the one predicted from the EGS^[35] program for the E705 calorimeter simulation.

For the case of the LGC, the gains G_s of the strips of the y view were derived from the equation:

$$E_x = \sum_{s=1}^S G_s P_s$$

where E_x was the energy of the shower as measured from the x view of the LGC and P_s the pulse heights measured in the strips.

The calibration was done about every month, hence gain variations had to be tracked between calibrations by using the LED data. The gains used in the analysis were determined from the formula:

$$G_{data} = G_{calib} \frac{P_{LED,calib}}{P_{LED,data}} \frac{P_{PIN,data}}{P_{PIN,calib}}$$

where G_{data} and G_{calib} were the gains used for the data analysis and the ones determined from the calibration, P_{LED} and P_{PIN} were the LED and PIN diode mean pulse heights measured at the current data ("data") and at calibration ("calib"). The photomultiplier/LED system was fairly stable. Its performance can be seen on figures 4.3a and 4.3b.

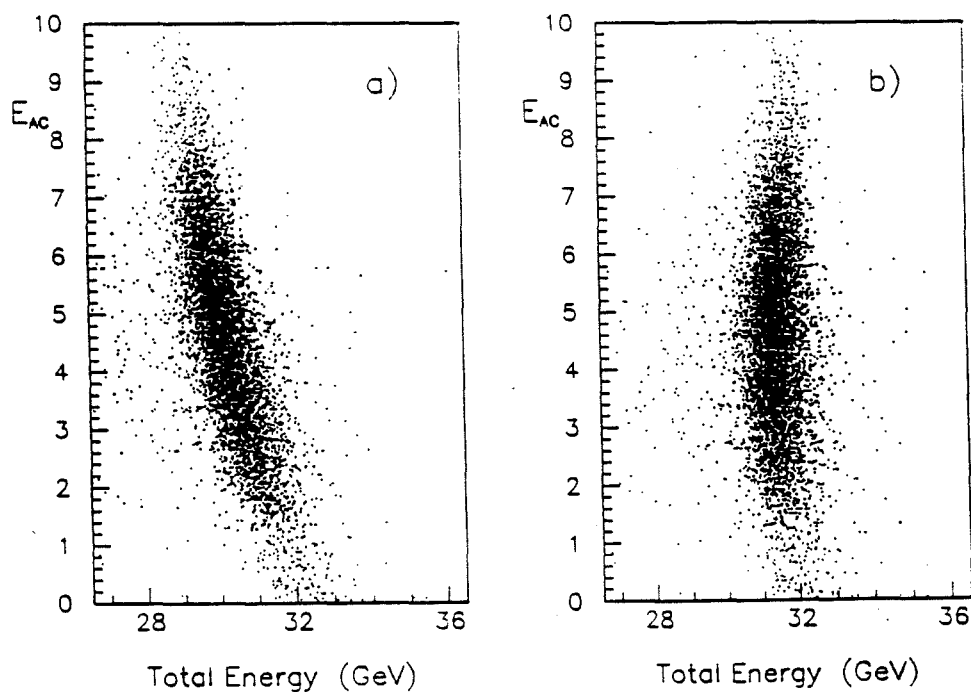


Figure 4.2 Active converter versus total energy for 31.5 GeV electrons before (a) and after (b) the "z correction".

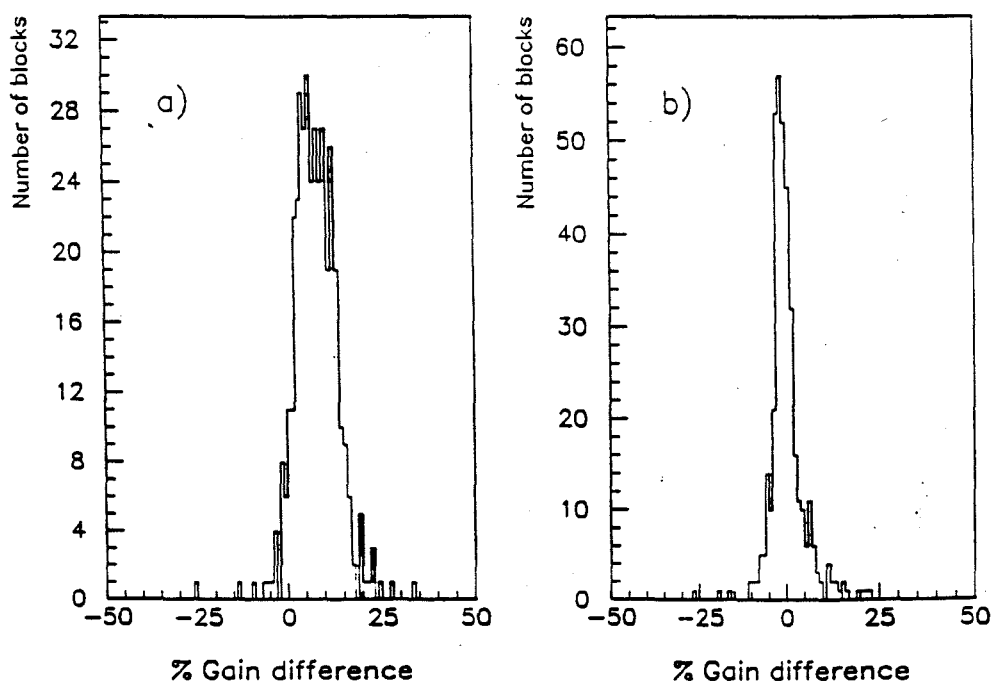


Figure 4.3 Percentage gain difference between the gains determined from the August and February calibrations before (a) and after (b) being corrected with the LED.

The former shows the difference between the gains determined from the August and February calibrations before and the latter after the LED correction (see reference 36 for a more detailed description).

4.3 Energy resolution

The energy and position resolutions are mainly due to the intrinsic detector limitations and to the statistical fluctuations in the shower development.^[37] The longitudinal development of an electromagnetic shower is a result of bremsstrahlung and pair production while the lateral development is mainly due to Coulomb multiple scattering of the electrons. In lead (scintillating) glass calorimeters the electromagnetic cascade is sampled by the production of Cerenkov (scintillation) light emitted from the relativistic e^+e^- pairs. The energy resolution σ/E is due to statistical fluctuations in the number of photoelectrons measured per unit of energy of the incident particle, resulting in a dependance of the type $\sigma/E \propto 1/\sqrt{E}$. In addition, fluctuations in the electronics and longitudinal and lateral leakage contribute by a term which, to first order, does not depend in the energy. Consequently, the energy resolution can be described by the formula:

$$\frac{\sigma}{E} = a + \frac{b}{\sqrt{E}}$$

The energy resolution for an electron shower was determined for the different types of blocks using the data from the calibration with electron beam. The results can be compared to the ones obtained from a test performed earlier by the E-705 collaboration at the Stanford Linear Accelerator Center (SLAC)^[38].

The energy determination algorithm formed clusters of 9 blocks similar to those formed by the Cluster Finder trigger, the peak block being the one hit by the electron beam. The energy of the nine blocks was then summed to give the energy deposited in the main

array. The measured energy in the active converter or in the LGC, in front of the cluster was added to the main array one, and the correction for the z-development of the shower was also applied.

The energy resolution σ was obtained from fitting a Gaussian to the energy spectrum at every energy. An example of such spectra and their fits for 6, 10, 30 and 60 GeV electrons at the SF5 blocks is shown in figure 4.4. This procedure for obtaining σ ignores the tails, taking into account only the central part of the distribution. The momentum spread of the beam was estimated to 1% and was subtracted from σ in quadrature. Figures 4.5a-c show the fractional energy resolution σ/E as a function of $1/\sqrt{E}$ for the SF5 blocks (a), the small SCG1-C behind the LGC (b) and the large SCG1-C behind the active converter (c). The resolutions have been fitted to the form $a+b/\sqrt{E}$ and the results are shown in table 4-1.

The measurement directly comparable to the SLAC results is the one for the large SCG1-C blocks behind the active converter where it was found $\sigma/E=0.64\%+3.94\%/\sqrt{E}$. The small difference from the SLAC measurement can be attributed to the difference in the material of the two hodoscopes and the 1.3 cm thick sheet of steel that was present in front of the active converter during the E705 run. The poor energy resolution of the LGC accounts for the worse resolution in that region. Previous measurements^{[39],[40]} of the SF5 resolution gave comparable results: $0.84\%+4.8\%/\sqrt{E}$.

TABLE 4-1 Energy resolution constants for various types of blocks.

Block type	a (%)	b (%)
SF5	0.54	5.1
SCG1 behind LGC	2.57	5.5
SCG1 behind AC	0.94	3.6

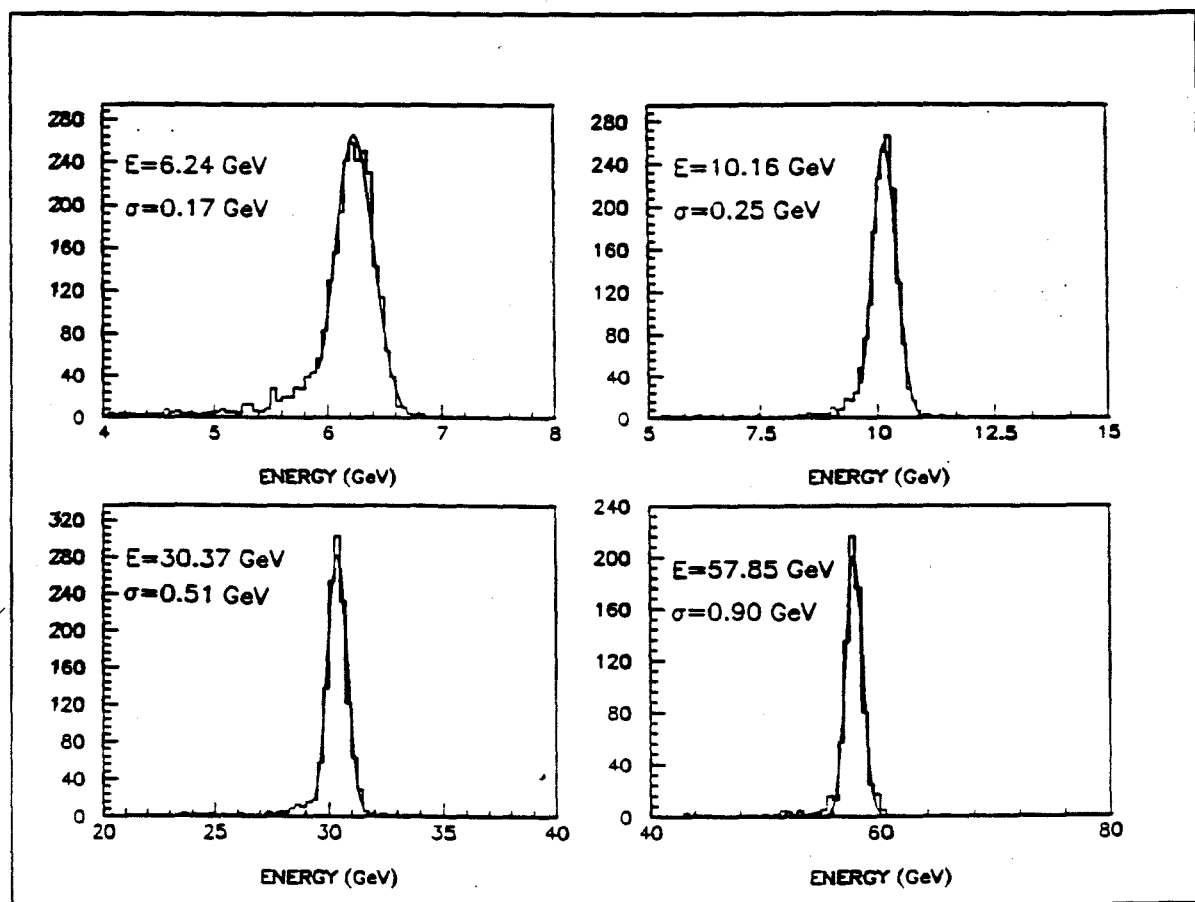


Figure 4.4 Energy distributions of electron beams and Gaussian fits for SF5 blocks.
Vertical axes show number of events per bin.

ENERGY RESOLUTION

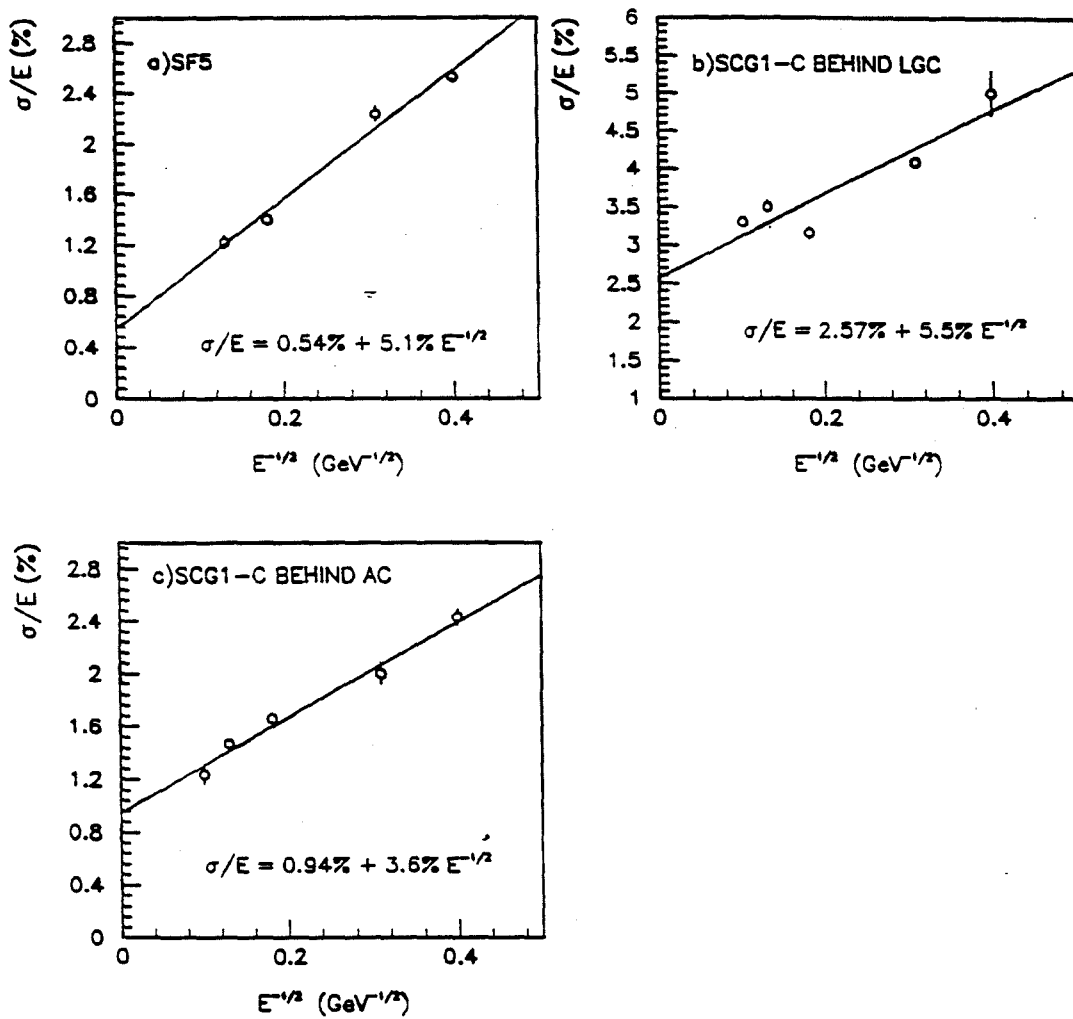


Figure 4.5 Energy resolutions for the SF5 (a), the small SCG1-C behind the LGC (b) and the large SCG1-C behind the active converter (c).

4.4 Position resolution

The position of a shower on the calorimeter was determined by the LGC in the central region and by the GTH in the wings. The projections in x and y of the position of the shower were first found by looking at the profile of the energy distribution in the tubes and strips respectively. The algorithm searched the hodoscopes within a window defined by an energy cluster in the Main Array and used a deconvolution technique to find peaks in either view. This technique was used in order to split correctly the energies deposited in the tubes by overlapped showers. Since the position determination depends on the energy measured in each tube, it is important that this energy be first shared among the showers that deposited it, before any extraction of the position is attempted. The technique applied a Fourier transformation to the input signal, then divided it by the expected pulse shape in the frequency space, transferred it back to the position space and finally extracted the peaks out of the signal. A peak was defined in the deconvolution space when a tube had a pulse height larger than that of its neighboring tubes and larger than a given threshold.

The expected shape of the shower was extracted from 30 GeV electron showers from the calibration data. It was compared to other energies, to ensure it did not depend on energy. The shape was 15 tubes (or strips) wide while the searching window was 64 tubes wide. For showers close to the borders of the hodoscopes, or when the searching window was less than 64 tubes wide, the missing tubes were set to zero.

The position resolutions of the two hodoscopes were determined by plotting the difference of the position of the shower as measured by the hodoscope and as projected from the beam track measured in the beam chambers. The distributions for the various beams were then fitted with Gaussians. The error of the beam track was subtracted in quadrature from the sigma of each distribution. The resulted sigmas were fitted to the form:

$$\sigma \text{ (cm)} = a + \frac{b}{\sqrt{E}} + \frac{c}{E} \quad (\text{E in GeV})$$

The results of the fits for the tubes and strips of the LGC and GTH are shown in figures 4.6a-d. The quadratic behavior can be attributed to overflows in the ADCs of the tubes and strips, at high electron energies ($E > 30$ GeV), which resulted in a degradation of the position resolution. The values of a, b, c are shown in table 4-2.

The energy in the LGC was calculated from an empirical formula which was derived from the calibration data, by matching the energy returned by the deconvolution to the one determined by summing up the energies of the tubes. The sum of the energies of the tubes in the shower was accurate only for isolated showers. In the case of overlapped showers (most often in high p_T pizeros) the energies deposited in the tubes had to be split between the two showers.

The estimation of the energy of each peak in the x and y views was essential not only for measuring the energy left in the converter plane, but for matching the x and y peaks to determine the position of the shower. Every peak in the x view was paired with each one in y and for each pair the following quantity was computed:

$$\text{asymmetry} = \frac{|E_x - E_y|}{|E_x + E_y|}$$

where E_x and E_y were the energies found in each peak.

TABLE 4-2 Position resolution constants for the two views of the hodoscopes.

Hodoscope view	a (cm)	b (cm•GeV ^{.5})	c (cm•GeV)
LGC tubes	0.08	0.24	3.35
LGC strips	0.04	0.20	4.02
GTH tubes	0.18	0.30	3.08
LGC strips	0.19	0.30	3.02

POSITION RESOLUTION

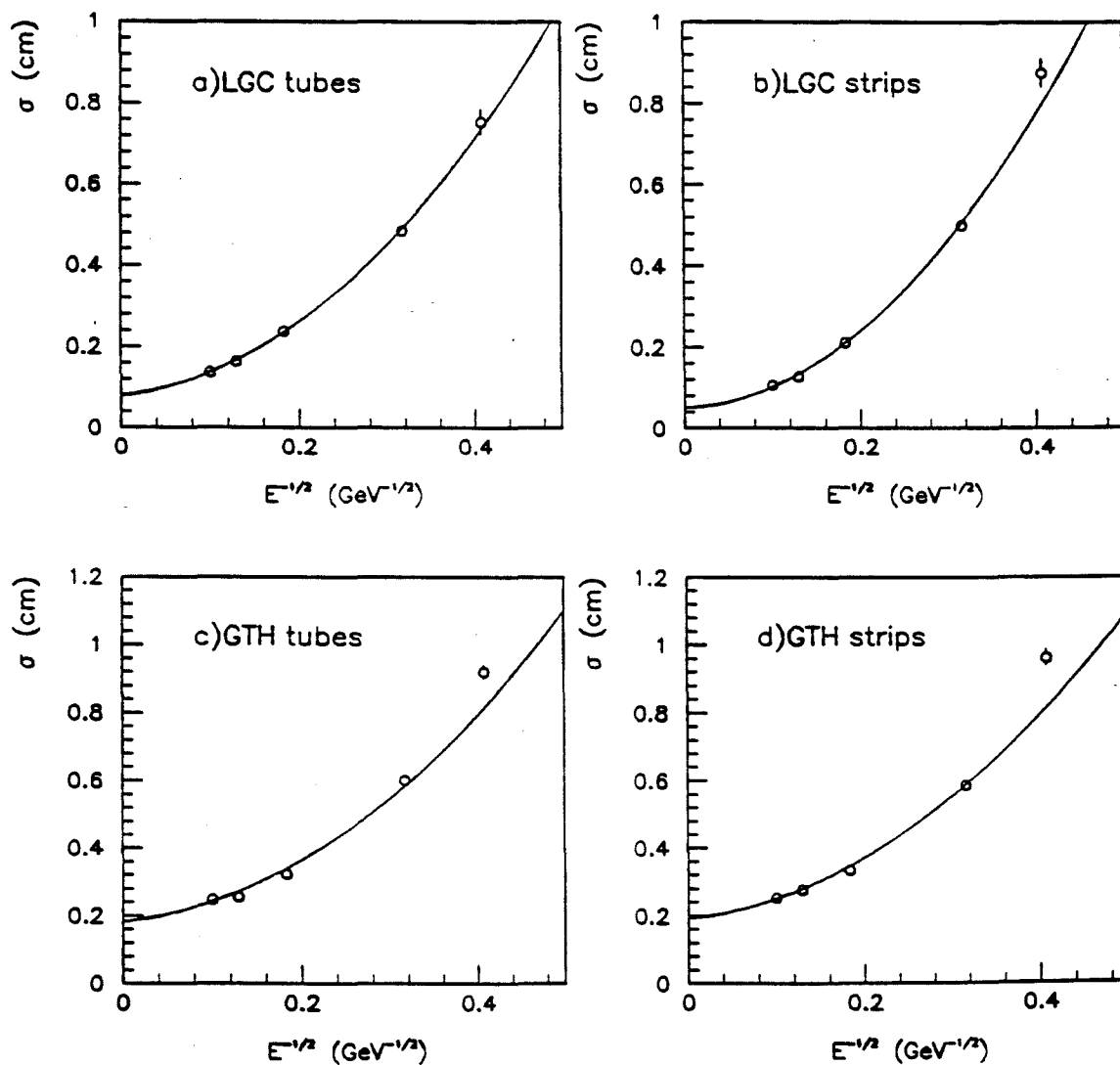


Figure 4.6 Position resolutions for the tubes (a) and strips (b) of the LGC, and for the tubes (c) and strips (d) of the GTH.

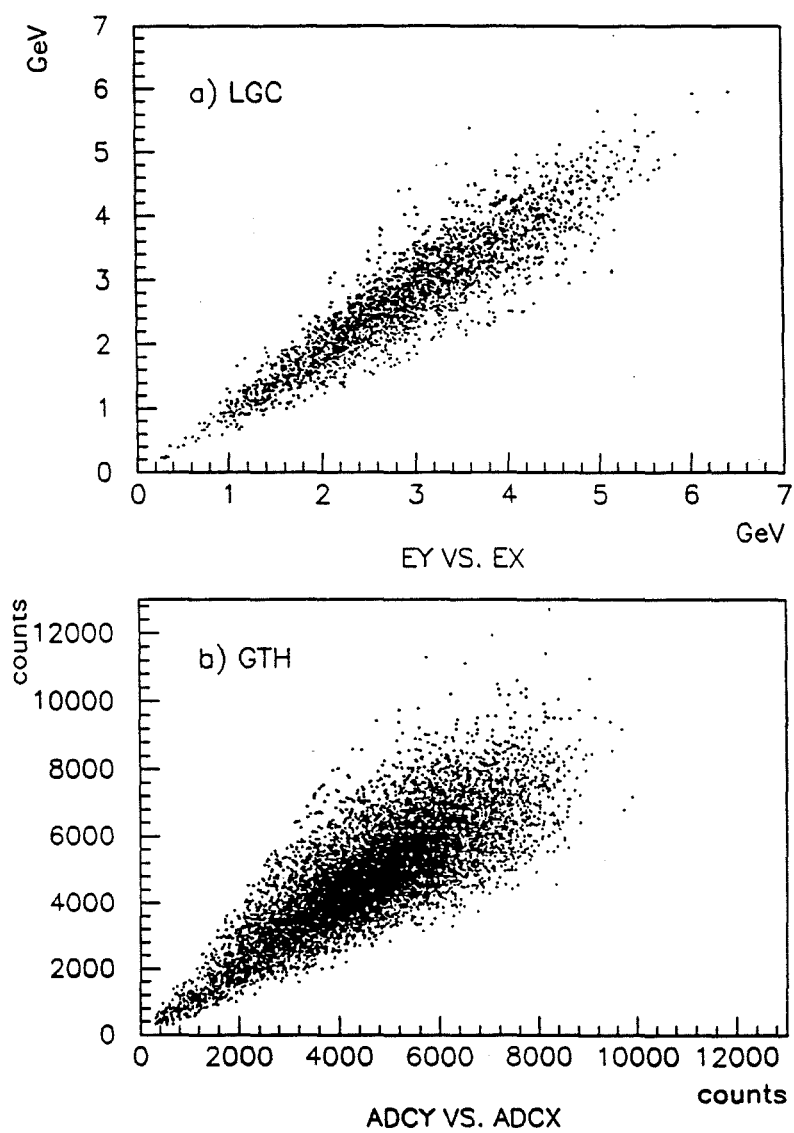


Figure 4.7 Energy correlation between the strips and the tubes of the LGC (a) and ADC counts correlation for the GTH (b), for 30 GeV electron showers.

The pair with the smallest asymmetry defined the position of the shower. The correlation between E_x and E_y for the LGC and the GTH is shown on figures 4.7a,b respectively. The width of the distribution is due to uncorrelated fluctuations in the two views.

4.5 Separation efficiency

One of the most important factors in a direct photon experiment is the capability of the calorimeter to separate showers that occur very close in space.

The main background to the direct photon signal at large p_T is coming from the pizero decay to two photons. For such a decay the mass of the pizero is given by :

$$m = [2 E_1 E_2 (1 - \cos\theta)]^{1/2}$$

where E_1, E_2 are the energies of the two decay photons and θ is the opening angle between them. This angle reaches its smallest value when $E_1 = E_2 = E/2$, where E is the energy of the π^0 . For a given energy E the angular distribution peaks at the minimum angle because of the isotropic decay of the π^0 and its Lorentz boost in the laboratory frame. It follows:

$$1 - \cos\theta_{\min} = \frac{2m^2}{E^2} \Rightarrow \sin \frac{\theta_{\min}}{2} = \frac{m}{E}$$

For small θ_{\min}

$$\sin \frac{\theta_{\min}}{2} \cong \frac{\theta_{\min}}{2} \Rightarrow \theta_{\min} \cong \frac{2m}{E}$$

Therefore the minimum opening angle decreases in inverse proportion to the π^0 energy. If the π^0 energy is high enough the two photons can get closer than the resolving power of the detector and they can be confused as one shower and a direct photon candidate.

To study the performance of the calorimeter in terms of spatial resolving power for the two views of the hodoscopes independently, a program was written to overlap two 30 GeV electron showers from the calibration data and to reconstruct them in various regions of the calorimeter. Since the shower shape in the x and y views of the hodoscopes is independent

of the energy of the incident particle for $E > 20$ GeV, the 30 GeV electron showers were a good approximation of the two photons for the pizeros of interest.

The calorimeter was divided into 8 regions, corresponding to the four quadrants of the LGC and the single/double width tube sections of the east and west wings of the GTH. About 250 electron showers were randomly selected in each region, and each shower was then overlapped with all the others. Their positions were reconstructed in each view independently, and compared to the original ones. The efficiency for separating the two showers was calculated as a function of their distance.

Figure 4.6 shows the result of such a study. The solid line on the top plot corresponds to the LGC tubes and shows about 100% separation efficiency for showers having distances greater than 1.8 cm between their projections in the x-view. The dotted and dashed lines correspond to the single and double width GTH tubes respectively. The minimum distance for the highest separation efficiency depends strongly on the width of the tubes and the width of the shower, as can be seen from the plots of figure 4.8. The widths of the showers, as found from 30 GeV electrons, are shown in table 4-3 for the different regions of the LGC and the GTH.

Figure 4.9 shows the distribution of the separation distance Δr between the two pizero decay photons on the three regions of the hodoscopes, obtained by a Monte Carlo generating pizero's with $p_T > 3$ GeV/c. The hodoscopes were built to separate these pizeros. The combination of figures 4.8 and 4.9 confirms this point.

The efficiency for separating two showers in the different views was fed to a Monte Carlo simulation, which estimated the acceptance and reconstruction efficiency of the pizeros (see chapter 6).

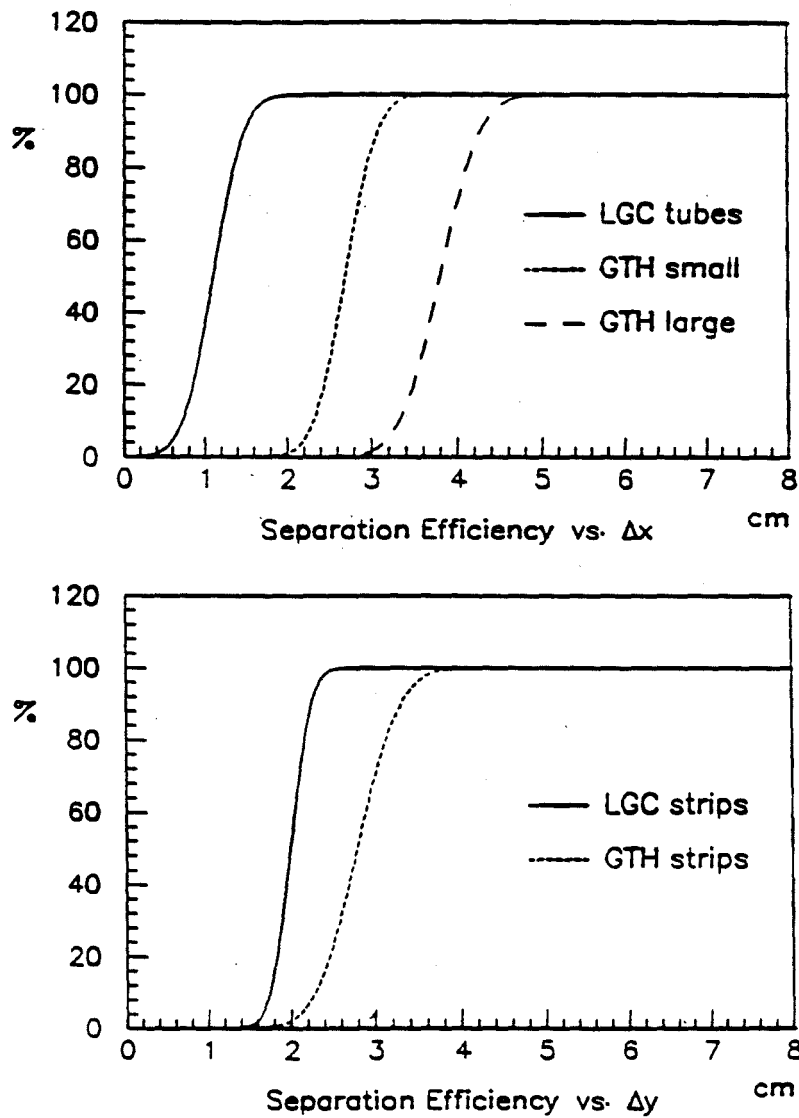


Figure 4.8 Efficiency for separating two 30 GeV electron showers in the various regions of the two hodoscopes as a function of the distance between their projections.

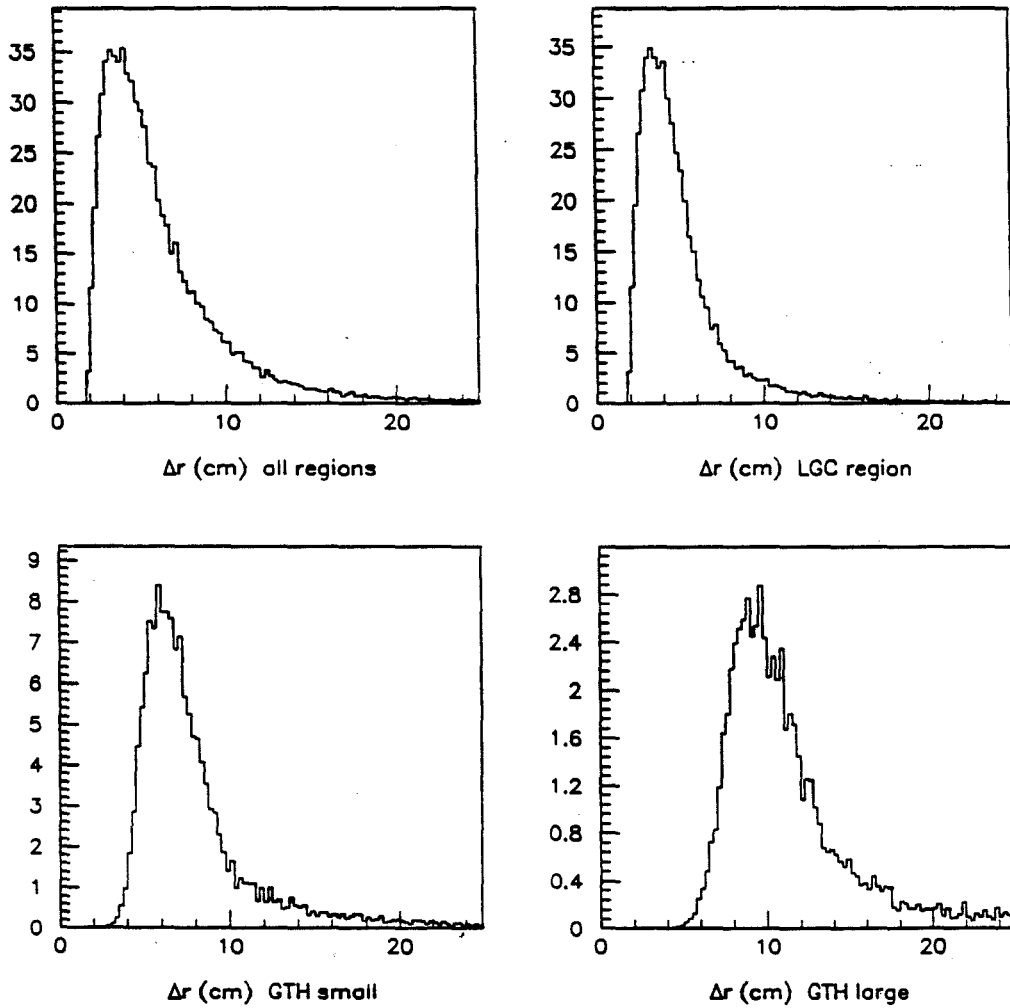


Figure 4.9 Distributions of the separation distance Δr between the two photons of $p_T > 3 \text{ GeV}/c$ pions on the hodoscopes: All regions (top, left), LGC region (top, right), GTH small tubes (bottom, left), and GTH large tubes (bottom, right). The distributions were obtained by a Monte Carlo. The units on the y axis are arbitrary.

TABLE 4-3 Shower widths in different regions of LGC and GTH.

Hodoscope region	Shower width (cm)
LGC tubes	0.8
LGC strips	1.1
GTH single tubes	1.6
GTH double tubes	2.4
GTH strips	1.8

4.6 Shower reconstruction

The program that was used to reconstruct the showers in the calorimeter was written in FORTRAN and consisted of a main routine and a large number of subroutines, each performing a specific task. The total memory used was about 1 Mbyte and the time spent to analyze a photon trigger was in average 5 sec of VAX-780 CPU time.

The showers reconstructed in the calorimeter were divided in two categories: electromagnetic and hadronic. The electromagnetic showers could be measured with high precision since they deposited all their energy in the calorimeter while the hadrons typically left in the calorimeter only a fraction of their energy. The reconstruction algorithm was tuned to maximize the number of reconstructed electromagnetic showers.

The algorithm was divided in four sections: a) Decoding of the raw data, b) Clustering, c) Energy sharing and d) Position finding.

After decoding an event, clusters of energy in the main array were identified in a similar way to the Cluster Finder. Then, the showers associated with the clusters were identified through the various steps of the code. Within a window equal to the size of the

cluster one or more showers were reconstructed, the number depending on how many x-y energy-matched peaks were found in the corresponding window in the hodoscope. If more than one pair was found within the searching window in front of the cluster, then each pair identified a shower. The original cluster was replaced by the found showers. The energy of the blocks of the original cluster was shared among the resulted showers in an iterative process. Finally the total energy of every cluster was calculated as the sum of the main array energy and the energy of the active plane corrected for the z-development of the shower.

The four sections of the code are described in more detail below:

a) The decoding.

The events were read and selected according to the trigger type. Then the information from the glass and the hodoscopes was decoded. The ADC counts for each block were pedestal subtracted and multiplied by the corresponding gain, measured from the calibration and corrected with the LED's, to give the energy deposited in the block. The pulse heights of the tubes and strips of the LGC were also converted to energy in a similar way. The information from the TDC's of the glass blocks was also decoded and converted to the difference between the time of energy deposition in a block and the time of the interaction.

The energies and the times of the glass blocks and the energies and pulse heights of the tubes and strips of the hodoscopes were saved in arrays, dimensioned to the number of channels in the corresponding detectors.

b) The clustering.

The clusters were defined in a way analogous to the Cluster Finder. The only difference was that the peak blocks selected as having energy greater than the energy of their neighbors were located in a cross shape, ignoring the energies of the corner blocks. This increased the number of clusters found and therefore the number of the candidate showers. The minimum energy threshold for a peak block was 1 GeV. While the clusters were searched for in groups of 5 blocks only, the actual clusters were assumed to consist of 3x3

blocks. The cluster energy was calculated as the sum of the energies in all the blocks and its position was initialized to the center of the peak block. The array CLBLKE containing the energies of the blocks of the cluster was defined for each cluster. The values of CLBLKE changed every time the energies of the corresponding blocks were shared among clusters.

The clusters were then classified as non-overlapping or overlapping according to the number of blocks in common (zero, greater than zero) and their partner clusters were flagged. As a starting value the energies of the common blocks were shared equally among the overlapped clusters. Finally, the clusters were ordered in descending energy.

c) The energy sharing.

In order to share the energies of the blocks among the overlapped clusters, a parametrisation of the transverse shapes of the photon showers was used.

The fraction of energy deposited by a shower into the blocks of a cluster depends on the incident particle energy, the position and angle of entrance in the glass. Patterns of energy deposition in the blocks were simulated by running the EGS program to generate photon showers in the E705 calorimeter configuration. Showers were randomly distributed in one quadrant of the calorimeter and were derived for the other three by using mirror symmetry. About 40,000 photons were generated for each energy. The quadrant was divided in 7 regions according to the types of blocks comprising the cluster. Each region was divided in $1 \times 1 \text{ cm}^2$ cells, and the patterns that corresponded to each cell were averaged, to take into account the shower fluctuations. Instead of keeping two numbers (mean, sigma) per block for each pattern the following ratios were defined:

$$\begin{aligned} r_{12} &= \frac{E_1 - E_2}{E_1 + E_2} & e_1 &= \frac{E_1}{E_1 + E_2 + E_3} \\ r_{13} &= \frac{E_1 - E_3}{E_1 + E_3} & e_2 &= \frac{E_2}{E_1 + E_2 + E_3} \\ r_{32} &= \frac{E_3 - E_2}{E_3 + E_2} & e_3 &= \frac{E_3}{E_1 + E_2 + E_3} \end{aligned}$$

where E_i was the energy in block i , with the convention that block 1 was the peak block, block 2 was the block closest to the beam hole and block 3 the block furthest from the beam hole. Only five out of the nine blocks of the cluster were used, in order to minimize the number of parameters in a pattern. The ratios were defined independently along the x and y axis of a cross shaped cluster. Thus for every position the 3 energy ratios e_i and their sigmas were stored and for every energy ratio r_{ij} the corresponding position and its sigma were also stored. A more detailed description of the simulation process leading to the definition of the patterns is given in reference 36.

An initial position for every cluster in the event was estimated using the position patterns. The ratios R_{12} , R_{13} , R_{32} were formed using the measured energies in the blocks of the cluster. A prediction of the position from each ratio R_{ij} was done by interpolating between the positions corresponding to the two pattern ratios r_{ij} closest to R_{ij} . The errors for the positions Δr_{ij} were also calculated using the sigmas from the tables. The positions in x and in y were given by the weighted average of the individual predictions:

$$x = \frac{\frac{x_{12}}{\Delta x_{12}^2} + \frac{x_{13}}{\Delta x_{13}^2} + \frac{x_{32}}{\Delta x_{32}^2}}{\frac{1}{\Delta x_{12}^2} + \frac{1}{\Delta x_{13}^2} + \frac{1}{\Delta x_{32}^2}} \quad y = \frac{\frac{y_{12}}{\Delta y_{12}^2} + \frac{y_{13}}{\Delta y_{13}^2} + \frac{y_{32}}{\Delta y_{32}^2}}{\frac{1}{\Delta y_{12}^2} + \frac{1}{\Delta y_{13}^2} + \frac{1}{\Delta y_{32}^2}}$$

The energy of each cluster was estimated by fitting the five blocks (cross shaped) of the cluster and minimizing a χ^2 defined as:

$$\chi^2 = \sum_{i=1}^5 \frac{(E_i - AP_i)^2}{\sigma_i^2}$$

where E_i were the energies in the blocks of the cluster from the array CLBLKE, P_i were the predictions for each block, given by the ratios e_i from the tables, multiplied by the measured $E_1 + E_2 + E_3$; σ_i were the corresponding statistical errors from the tables; A was a scaling constant, relative to which, the χ^2 was minimized, defined at the minimum point as:

$$A = \frac{\sum_{i=1}^5 \frac{E_i P_i}{\sigma_i^2}}{\sum_{i=1}^5 \frac{P_i^2}{\sigma_i^2}}$$

After predicting the energies and their sigmas in the 5 blocks of the cluster, the energies of the corner blocks were also predicted using the ratios from the pattern tables. The sum of the predicted energies over all the blocks of the cluster gave the total main array energy for this cluster. The energy in CLBLKE was adjusted for every block shared by clusters, in proportion to the predicted energy for these clusters, in such a way that the sum of the contributions to this block would equal the actual measured energy.

The previous process was repeated either ten times or until convergence. The latter was assumed for a cluster, if the energy CLBLKE in its blocks changed less than 5% from the previous iteration.

At the end of each iteration, the fractional energy error

$$\frac{\sum_{i=1}^5 (E_i^{\text{OUT}} - E_i^{\text{IN}})^2}{E_{\text{TOTAL}}^{\text{IN}}}$$

was estimated for every cluster (E_i^{IN} and E_i^{OUT} being the energies of the block i before and after the fitting respectively). This quantity was a criterion on how well the photon pattern matched the lateral shape of the cluster. From now on the term χ^2 will refer to this quantity, which was similar to real χ^2 except for the division by the errors. Such a quantity was chosen since the errors were very hard to estimate because of correlations among the blocks.

d) The position finding.

The position of the showers corresponding to clusters was determined from the GTH and LGC hodoscopes. The position finding algorithm was called twice for every cluster. The first call searched for cases where only one shower was associated with one cluster.

The second searched for cases where two or more showers were associated with the same cluster.

The algorithm first defined a window on the hodoscope in front of the cluster. The window, centered in the position predicted by the energy fit, had a width of 3 times the position error, but no more than 6 cm and no less than 3cm. A search for peaks was done in the x and y views independently, using the deconvolution technique. A minimum energy threshold was set to 0.2 GeV for the LGC and 300 counts for the GTH to eliminate peaks from noise. Then a one-to-one match was tried according to the absolute value of their energy asymmetry $(E_x - E_y)/(E_x + E_y)$, required to be less than 0.25 for the LGC and 0.35 for the GTH. A found peak was defined corresponding to the x-y pair with the smallest asymmetry. The pair of the peaks so correlated was eliminated from further consideration. A flag was set for every cluster if its position was derived from the hodoscope or it was a result of the fit.

Next the width of the searching window was increased to 1.5 times the size of the peak block, in order to find the positions of possible additional showers within the area of the cluster. This time the peaks returned by the deconvolution were compared not only for one-to-one matches but also for two-to-one. This took care of the cases where two peaks were so close in one view to be seen as one, while they were far enough in the other view to be recognized as two. In this case the asymmetry was defined as:

$$(E_y - E_{x1} - E_{x2})/(E_y + E_{x1} + E_{x2}) \quad \text{if the degeneracy was in y, and}$$

$$(E_x - E_{y1} - E_{y2})/(E_x + E_{y1} + E_{y2}) \quad \text{if it was in x.}$$

A two-to-one match was defined if the peaks fulfilled the following: a) Their two-to-one asymmetry was less than 0.25 for the LGC and 0.35 for the GTH, and b) Each one-to-one energy asymmetry was less than 0.5. The reason for the cut (b) and the inefficiency it introduces are discussed in section 6.2. If more than one match was found, then the original cluster was split into showers, each shower corresponding to a match. The active plane

energy for the LGC showers was given from the non-degenerate peaks, while their main array energy was derived from the sharing algorithm.

4.7 Tracking

The tracks of the charged particles of the event and the beam were reconstructed using the information of the proportional and drift chambers.

The beam tracks were reconstructed using the three beam chambers. The hits of the three planes of each chamber were combined by three (Y,U,V) to form “triplet” space points or by two (YU, YV,UV) to form “doublet” points in case triplets could not be found. The tracks were then defined by fitting these points (one for each chamber) to straight lines. The number of events with no beam tracks found was less than 5%, while 30% of the events had more than one track reconstructed. The beam track was projected to the center of the target to define the x, y coordinates of the interaction vertex. If more than one track was found, then the number of the reconstructed tracks between the target and the magnet (“upstream tracks”) intercepting a cylinder around each beam track was found. This cylinder had a radius equal to 3σ , where σ was the error of the beam projection on the target, and its length was confined inside the area of the target. The beam track with the largest number of upstream tracks intercepting it was defined as the beam track that caused the interaction.

The upstream tracks were found using the 10 proportional and 9 drift chamber planes. At first, lines (“2-D lines”) were reconstructed independently in each of the three X, U and V views, defining the XZ, UZ and VZ planes respectively. This was done by combining two hits of the same view from different chambers and search the other chambers for more points on the line joining these hits. The 2-D lines of different views were then combined to form the tracks in the three dimensional space. The tracks were accepted if they intercepted the apertures of the magnet and the target.

The z of the vertex was found using the upstream and the beam tracks. It was defined by a fit to minimize the quantity:

$$\chi^2 = \sum_{j=1}^N \left\{ \frac{(x_{\text{beam}} - x_{\text{track},j})^2}{\sigma_{x,\text{beam}}^2 + \sigma_{x,j}^2} + \frac{(y_{\text{beam}} - y_{\text{track},j})^2}{\sigma_{y,\text{beam}}^2 + \sigma_{y,j}^2} \right\}$$

where the sum is over the tracks and x, y are the x and y coordinates at the z of the vertex and σ_x, σ_y are their sigmas respectively. The subscripts “beam” and “track” refer to beam and upstream tracks respectively.

The tracking downstream of the magnet was done using the 12 planes of the rear drift chambers. At first, 2-D lines were found in the X view and they were then combined with Y lines formed by two hits at the U and V planes. The track had to point back to the magnet aperture and to be verified by hits in the CPX and CPY hodoscopes.

Finally the front and rear segments were matched at the center of the magnet with the criterion that the distance between their projections be $\Delta x < 3$ cm and $\Delta y < 6$ cm.

The momentum of the tracks was found by calculating the difference of the x slopes upstream-downstream of the magnet.

The efficiency to reconstruct a track downstream of the magnet was estimated by a Monte Carlo simulation to be about 70%.

4.8 Electron studies

The most informative source for studying the systematics of the detector is the reconstruction of electrons and positrons in the data, because it combines the tracking with the shower reconstruction. The electrons^[41] leave all their energy in the calorimeter, and being charged particles, they can be tracked by the chamber system and their momentum can be calculated from the magnetic bend of their trajectory. They are relatively easy to be

identified in an event from the ratio of their reconstructed energy E to their measured momentum p , which is 1 since their mass ($0.5 \text{ MeV}/c^2$) is negligible relative to their momentum. The other charged particles, when they interact in the calorimeter leave only a fraction of their energy so that typically $E/p < 1$. The major source of the electrons/positrons is photon conversions in the target. About 7% of the photons, from decays or directly produced, convert to an e^+e^- pair inside the Li target.

The algorithm to find electrons used the information of the tracking and shower analysis. It combined tracks with showers, by projecting the tracks on the calorimeter and finding the closest track to an electromagnetic shower within a distance of no more than 3 cm. The criteria used to define an electromagnetic shower were:

- a) A fiducial cut around the hole of the calorimeter $45 \times 45 \text{ cm}^2$.
- b) The energy of the shower to be greater or equal to 2 GeV. This requirement was established from a Monte Carlo study which showed that electrons with momentum less than 2 GeV did not reach the calorimeter because of the bend of the magnet.
- c) The ratio of the energy deposited in the active plane to the squared root of the total energy of the shower to be greater than $0.15 (\text{GeV})^{1/2}$. This cut was a result of a study of the differences between the response of the calorimeter to electrons and hadrons, done with electron and pion calibration beams (see Hadron Rejection in section 5.2).
- d) The position of the shower to be given by the hodoscopes and not from the fit.
- e) The lateral shape of the shower to be consistent with an electromagnetic shower ($\chi^2 < 2.5$). The χ^2 cut was loose because all the showers in the data were fitted with patterns of photons coming from the target, so that for the case of the electrons the incidence angle was not accounted for correctly. The cut was nevertheless good enough to reduce the hadronic background.

The absolute energy scale was set in the calorimeter with interaction trigger events recorded at low intensity (about 3KHz interaction rate). The gains, determined in the

calibration of the calorimeter, were adjusted in such a way that the mean of the E/p distribution be at 1 in the various regions of the calorimeter. The E/p distributions were also produced for the high rate photon trigger data, to ensure the stability of the scale with the interaction rate and the linear dependence of the pulse heights versus energy, since the energies of the electrons reconstructed from minimum bias trigger are relatively lower than the ones in high transverse energy events. Figure 4.10 shows the E/p distribution for all the blocks (top left) and the three types small, large SCG1-C and SF5. The hadronic background under the peaks is more evident for the scintillating glass blocks than for the SF5, since the total material in an SCG1 block is equivalent to two interaction lengths while it is only one for the SF5. The events with E/p greater than one are a result of overlapping showers with energies not properly shared and of hadrons depositing large amounts of energy close to the phototube of the glass block. The backgrounds were subtracted and the peaks were fitted to Gaussian distributions (fig. 4.11). The means were close to one in all cases, while the sigma was about 9% for the large and 10.6% for the small blocks. The electrons were defined from the ratio E/p as having $0.85 < E/p < 1.15$. Their energy distribution is shown on figure 4.10 (bottom left). The E/p distribution was also fitted for various momenta and the variation in the means was estimated to 1.0%, which defined the error of the absolute energy scale. The bottom right plot of figure 4.12 shows the E/p distribution for momenta greater than 20 GeV. The top plot shows the positions of the reconstructed electrons on the surface of the glass. The gaps in the plot show the inefficient regions of the calorimeter, mainly caused by dead tubes in the hodoscopes. The information on inefficient regions was used in the later stages of the reconstruction analysis.

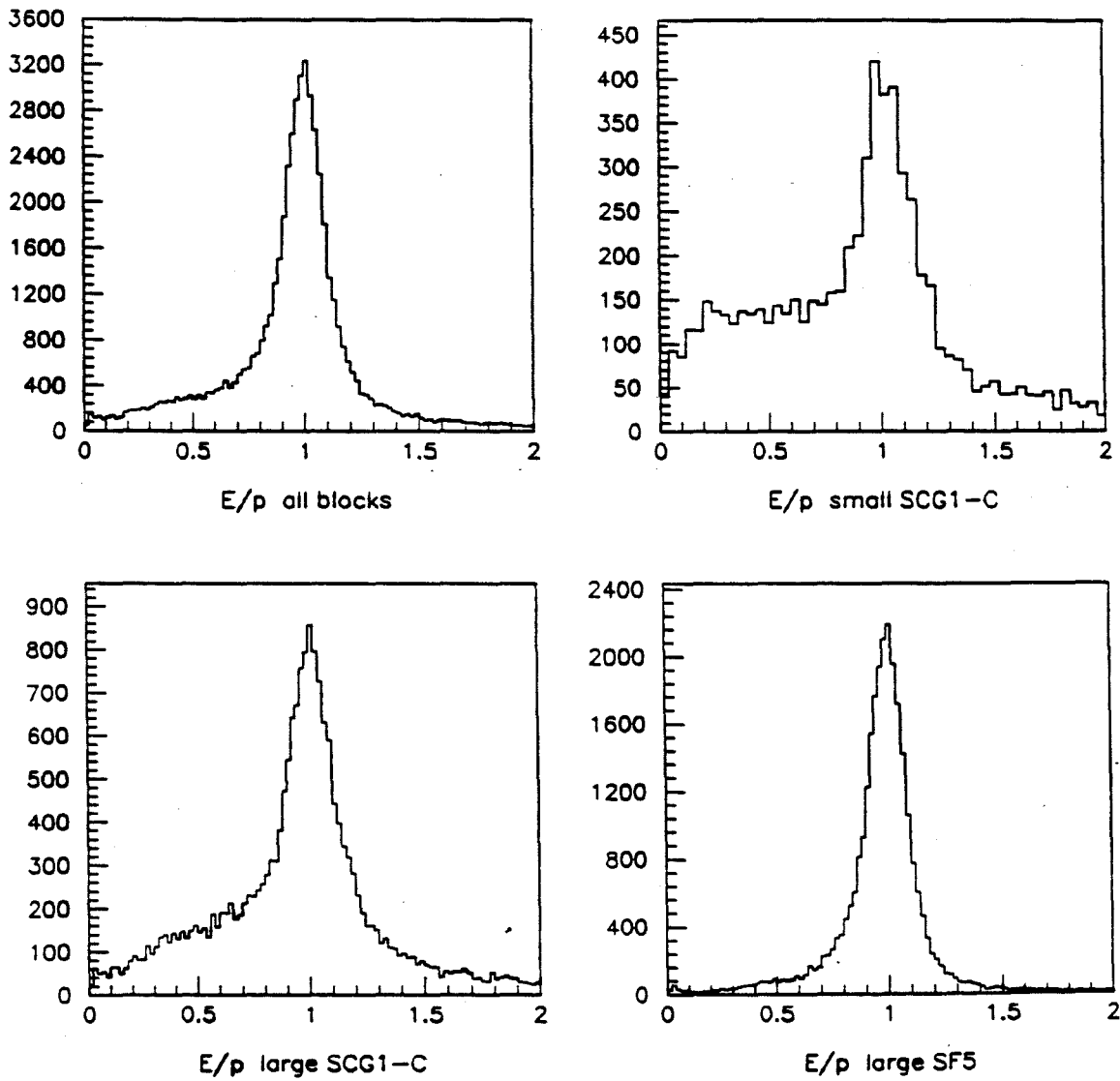


Figure 4.10 E/p distribution of showers everywhere on the glass (top left), on the small SCG1-C blocks (top right), on the large SCG1-C blocks (bottom left), and on the large SF5 (bottom right). The vertical axes show number of events.

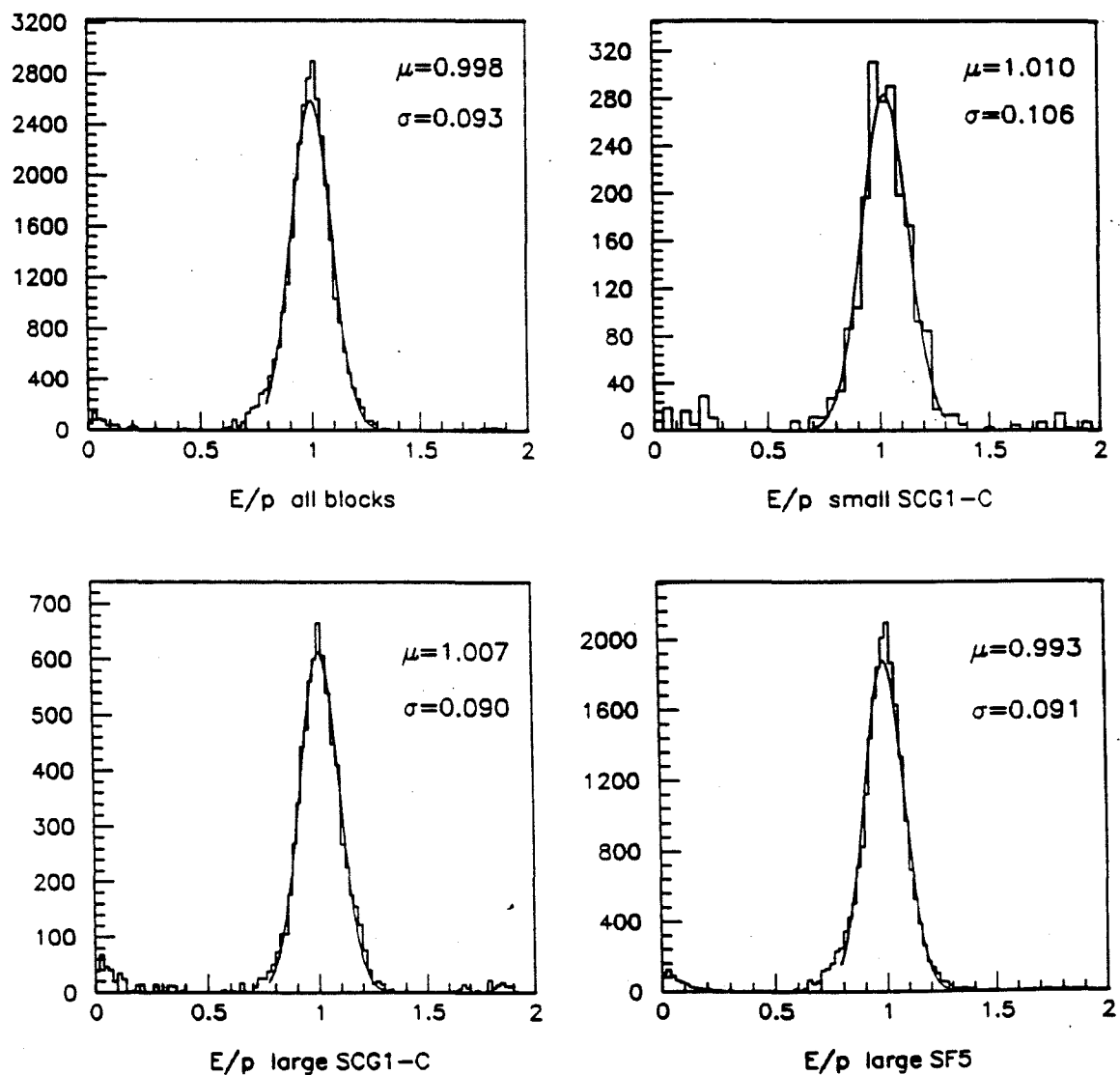


Figure 4.11 Gaussian fits to E/p distributions for electrons (background subtracted) in the entire calorimeter (top left) and in the three different region separately. The vertical axes show number of events.

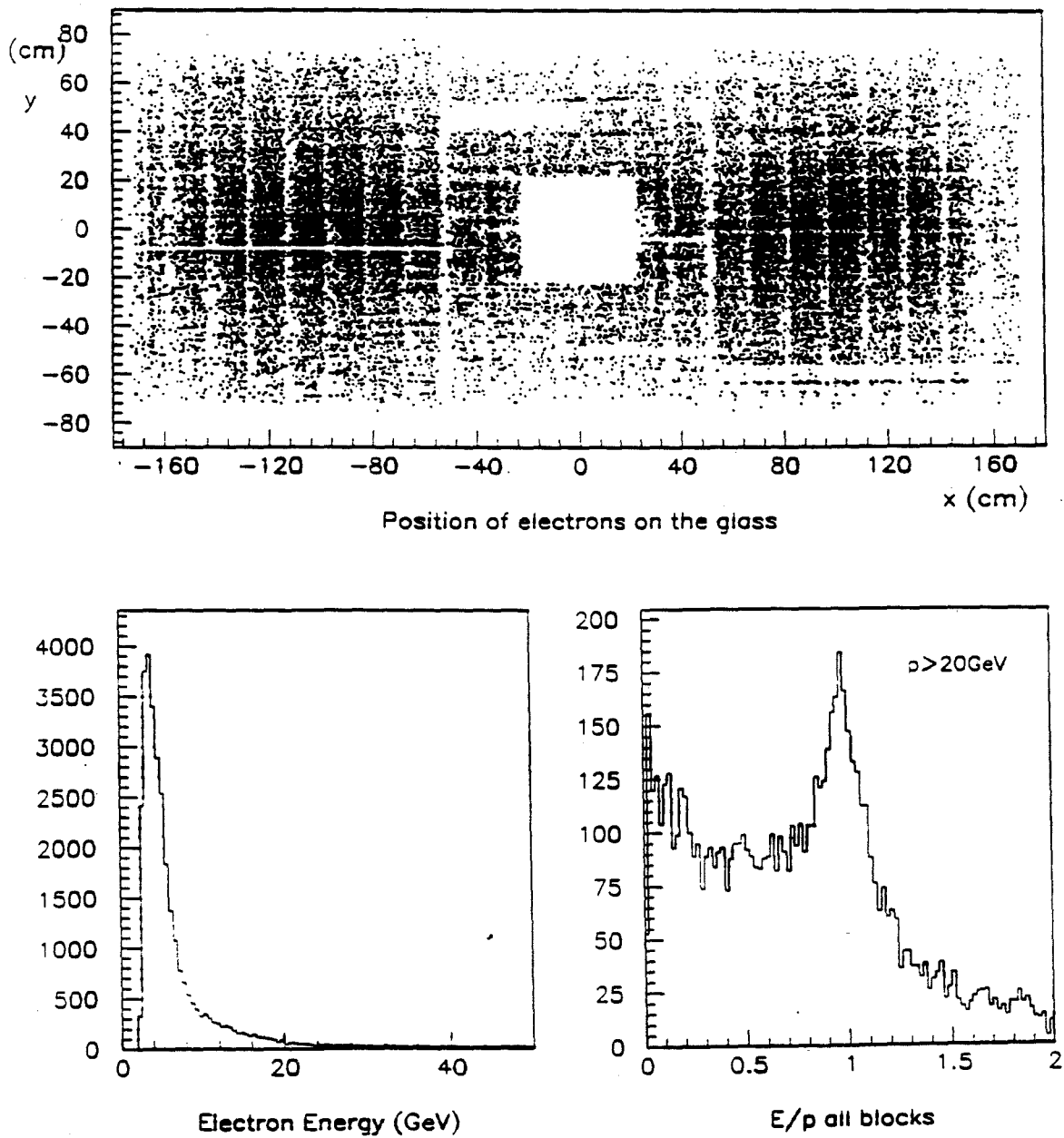


Figure 4.12 Positions of electron and positrons on the glass (top plot), their energy distribution (bottom left) and E/p distribution for $p > 20 \text{ GeV}$.

Chapter 5

Data Analysis

5.1 Overview

The purpose of the analysis was to extract the direct photon signal from the background. The background comes from hadrons interacting in the calorimeter, from out-of-time interactions, from halo muons that underwent bremsstrahlung upstream of the calorimeter, and from neutral mesons decaying to two photons which could not be properly reconstructed as such. To reduce the background to the direct photon signal and to study the systematics of the detector, the pizero signal had to be extracted first. The invariant cross section for the pizero inclusive production was then measured, as an intermediate step towards the measurement of the direct photon one.

To eliminate the background and extract the signal, the analysis process applied a series of sequential cuts to the data, based on the differences between the behavior expected of the signal and the background in the spectrometer. The reduction of the data was done in three passes, each pass performing a higher level of reconstruction and applying stronger cuts than the one before. The final analysis was done in the remaining events. The three passes are now described in more detail.

a) First pass.

This was a fast filter, executed on a microprocessor farm, the Fermilab ACP system^[42]. The data from the raw data tapes was sent from a host microVAX computer to the ACP nodes, where they were separated to three streams, according to their trigger type. The first two streams were the dimuon and the single photon triggers which were selected by filtering programs before being analyzed for track reconstruction and written to tape, while the third stream consisted of the rest of the triggers, which were written directly to a separate tape.

The fast pass algorithms had to be simple enough to fit within the memory size of the ACP system, therefore the photon filter worked with simple clusters rather than showers. The clusters were formed in the same way as done by the hardware of the Cluster Finder. A fiducial cut was applied around the hole in the center of the calorimeter, requiring the peak block of the cluster to be outside an area of $45 \times 45 \text{ cm}^2$ centered on the beam. The energy of the peak block was required to be greater than 4 GeV and the cluster to have at least one block with its hardware p_T bit set. The cluster energy was then converted to transverse energy by multiplying it by the sine of the angle between the z-axis and the line connecting the position of the cluster and the center of the target. In order to remove triggers coming from fluctuations in the thresholds of the cluster finder, the transverse energy of the formed clusters had to be greater than a threshold depending on the trigger level and set to 1.0, 2.0, 3.0 GeV for the PT2, PT3 and PT4 triggers respectively. The clusters surviving such cuts were then checked for energy in the active plane in front of them. If the position of a cluster was inside the active converter region, then the sum of the energies of the active converter blocks in front of the cluster, lying within a window of $15 \times 15 \text{ cm}^2$ centered on the position of the cluster, was formed. The total energy in the active converter was then required to be greater than 200 MeV. If the position was in the LGC region, then a window equal to three times the peak block width was used. The sums E_x and E_y of the energies of respectively the tubes and strips within the window were formed. Each was required to be greater than

200 MeV. The events that had at least one cluster fulfilling the previous requirements were further analyzed for track reconstruction and were finally written to magnetic tapes. The tracking information was also added at the end of each event.

The effect of the pass 1 cuts on the photon triggers is shown in table 5-1. The rejection was mostly due to the requirements of substantial energy deposition in the active converter. The effect of the cut for noise in the Cluster Finder was less than 1%.

TABLE 5-1 Percentage of events surviving first pass cuts.

Trigger type	Events passed (%)
PT2	49
PT3	42
PT4	38
TOTAL	42

b) Second pass.

In order to reduce the amount of tapes to be handled in the second pass, the first pass output tapes were copied to Exabyte 8-mm cassettes in a ratio of 5 tapes per cassette. The exabytes were analyzed by the second pass on workstations "VAX 3200".

The algorithm of the second pass consisted of reconstructing all the showers in an event using the shower reconstruction program described in section 4.6. The showers were ordered in descending transverse momentum and they were flagged as electromagnetic by requiring their active plane energy to be greater than 200 MeV. To be accepted, the events had to fulfill the following requirements:

i) The showers associated with the triggering cluster (having their peak block common with one of the blocks of that cluster) had to be electromagnetic. About 60% of the events passed this cut.

ii) The highest transverse momentum shower associated with the triggering cluster had to have $p_T > 2.8 \text{ GeV}/c$, or when combined with at least one other electromagnetic shower in the event, to result in total transverse momentum greater than $2.8 \text{ GeV}/c$ and invariant mass less than $1.5 \text{ GeV}/c^2$. About 30.3% and 14.5% of the events surviving the first cut, belonged to the first and second category respectively.

The events that survived the previous cuts (27% of the input events) were written to exabyte cassettes. The shower information was added at the end of the raw event, after the tracking information.

c) Third pass.

The final pass was also done on DEC workstations. Stricter cuts on the triggering shower (highest p_T shower in the event) were applied and the surviving events were condensed to two disk files, one for the negative and one for the positive beams. The third pass requirements and their effect were the following (cuts are applied in sequence, percentages refer to the surviving events):

i) The vertex reconstructed from the tracking information was restricted to the target. The z of the vertex had to be $-562 \text{ cm} < z < -505 \text{ cm}$. About 96.1% of the events survived this cut.

ii) The triggering shower had to be in-time with the interaction that produced the event. The time (measured by the glass TDCs) of every block in the shower was required to be within $\pm 20 \text{ nsec}$ of the interaction time. 70.4% of the events passed.

iii) The ratio of the energy left in the active plane to the squared root of the total energy of the shower had to be greater than $0.07 \text{ GeV}^{1/2}$. 78.7% of the events passed.

iv) The distance between the shower center and the projection of any track to the surface of the glass array had to be greater than 5 cm. About 93.4% of the events passed this cut.

v) The shower was required to have $p_T > 3.0$ GeV/c, or to combine with another electromagnetic shower to form a total $p_T > 3.0$ GeV/c. About 31.2% of the events passed the former cut and 21.4% of the remaining events passed the latter.

23.8% of the events passed these cuts.

The number of photon triggers analyzed in each pass for negative and positive beam, forming the sample of the data presented in this dissertation, is shown in table 5-2.

TABLE 5-2 Number of photon triggers analyzed in each pass.

Analysis level	Negative triggers	Positive triggers
Pass 1	2,740,000	2,557,600
Pass 2	1,150,900	1,074,200
Pass 3	310,750	290,030
Final	73,850	69,000

5.2 Hadron rejection

The hadrons that interacted in the calorimeter and left enough energy to trigger, were one of the major backgrounds to the direct photon signal.

A study of the response of the scintillation glass to 4-14 GeV/c pions was done as a part of the tests performed at SLAC^[43] and it was repeated at E705 with 30 GeV/c and 60

GeV/c pion beam. The response of the detector was compared to the one derived from 60 GeV/c electrons. Figure 5.1a shows the energy deposited in the calorimeter by 60 GeV/c pions and electrons. The scintillating and lead glass blocks were 1.96 and 1.07 interaction lengths respectively (for 30-200 GeV/c pions). The LGC and the Active Converter blocks were 0.1 and 0.33 interaction lengths respectively. This led to a probability for a pion to interact equal to 90%, 88% and 75.3% for the regions of the SCG1-C behind the Active Converter and behind the LGC and for the SF5 behind the Active Converter. The peaks near zero in fig. 5.1a-d are due to non-interacting pions and muons, which deposited an apparent energy of 1.0 GeV. The pion beam had about 8% contamination from muons. The ratios of the interacting to total number of pions in the three regions of the calorimeter, mentioned before, were calculated to be after subtracting the muon contamination 90.2%, 88.5% and 74.4% respectively, in agreement with the predicted probabilities.

The energy measured by the glass is not equal to the energy deposited in it by the hadronic shower. The "pulse height - energy" correspondence was determined by the electrons, which start depositing energy early in the glass, while the hadrons can interact and leave energy anywhere along the block. The apparent energy of interacting hadrons depends on the point of interaction. It appears to be greater than the incident hadron's energy if the hadronic shower reached its peak close to the phototube. This explains the tail at energies higher than 60 GeV in the pion distributions. Figures 5.1b-d show the energy distribution for pions interacting in the lead glass blocks, and the scintillating blocks behind the LGC and the Active Converter respectively. As one would expect, the mean deposited energy increases with the total interaction length of the material.

The cuts applied in the final analysis program in order to reduce the hadronic background were the following:

a) $E_{AC}/\sqrt{E} > 0.15 \text{ (GeV)}^{1/2}$, where E_{AC} is the energy deposited in the active plane and E is the total energy of the shower. The hadronic showers typically leave less energy in the active plane (LGC or Active Converter) than the electromagnetic showers (fig. 5.2a). This

makes the energy of the active plane a good criterion to reject the hadrons. The cut was derived from a study with photon showers simulated with the EGS program, in order to minimize the number of the rejected photons at higher energies. The presence of the square root term in the denominator reduces the energy dependence of the cut. Table 5-3 shows the effect of this cut in the three regions of the calorimeter. The lower rejection power in the Active Converter region is due to its longer interaction length (0.33 compared with 0.103 for the LGC).

b) $\chi^2 < 0.05$, where χ^2 is the chisquared obtained from the fit of the lateral shape of the shower to photon shower shapes (see section 4.6). The difference between the lateral development of the hadronic and the electromagnetic shower is another good criterion for separating the two types of showers (fig. 5.2b).

c) $\Delta r > 8$ cm , where Δr is the distance of the center of the shower from the closest track on the glass. This was done to remove charged hadrons that either interacted and gave a trigger or corrupted the energy of an electromagnetic shower occurring within such a small distance from the hadron.

The effect of the hadronic background was estimated using the PYTHIA^[44] Monte Carlo, to generate events containing high transverse momentum hadrons and then tracking them to the calorimeter with a simulator of the spectrometer. The value of p_T that the reconstruction program will assign to a charged hadron, when interpreting it as a photon, will differ from the hadron's real p_T for the following reasons; because of the analysis magnet, the apparent p_T of the charged hadrons is different from the actual value, since the p_T of the showers is calculated with the assumption that they are coming straight from the target. Moreover only some of the hadrons interact in the glass and when they do so, they leave only a fraction of their energy. To estimate such an effect, in the Monte Carlo the energy deposited by interacting hadrons was distributed according to the energy distributions of figure 5.1, obtained from the 60 GeV pion calibration events. The energies were then scaled proportionally to the energy of each produced hadron.

60 GeV PIONS

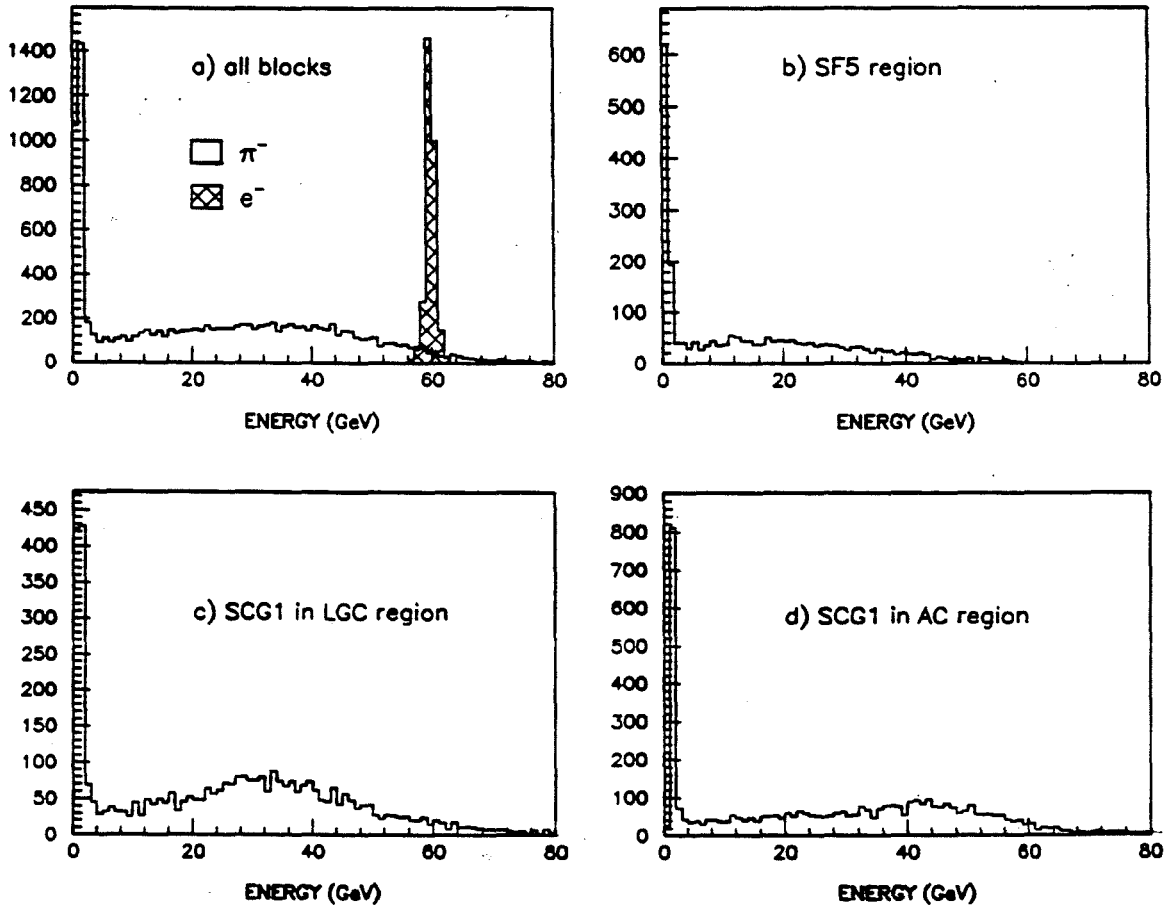


Figure 5.1 Energy distributions for 60 GeV pions measured by the calorimeter, everywhere (a), in the SF5 region (b), and in the scintillating glass blocks behind the LGC (c) and behind the Active Converter (d).

60 GeV ELECTRONS AND PIONS

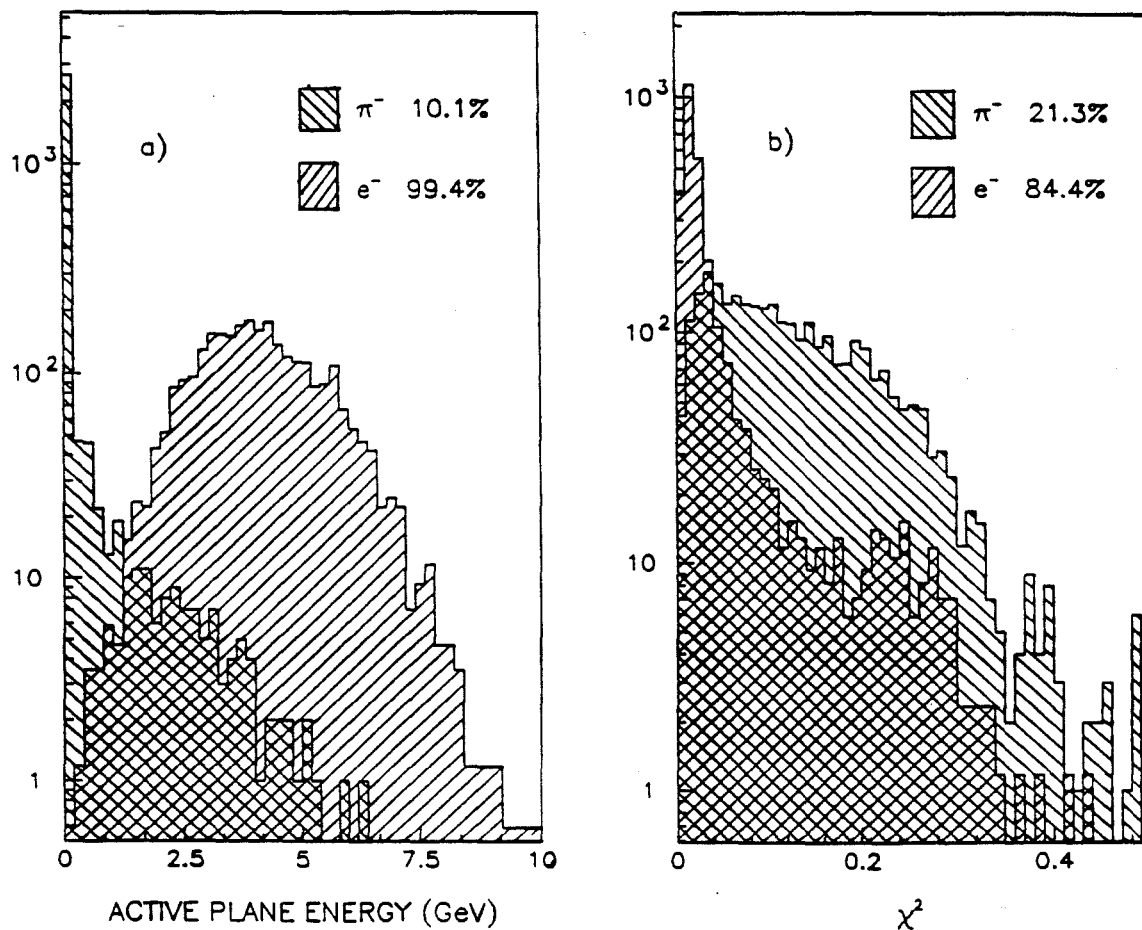


Figure 5.2 Comparison between 60 GeV electrons and pions at the LGC region. Active plane energy (a) and chisquared distributions (b). The y-axis of both histograms are in logarithmic scale to emphasize the differences between the distributions. The numbers are the percentage of surviving events after applying the $E_{AC}/\sqrt{E} > 0.15$ (a) and $\chi^2 < 0.05$ (b) cuts.

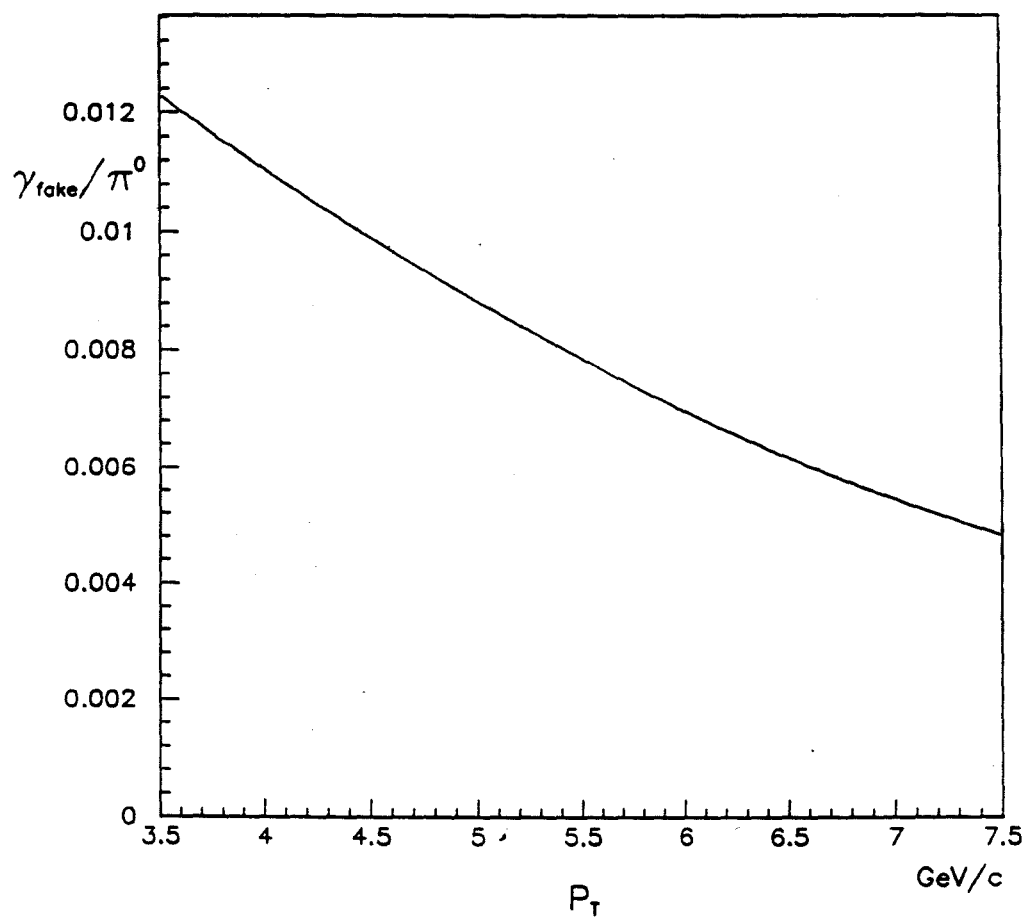


Figure 5.3 $\gamma_{\text{fake}}/\pi^0$ ratio for fake photons coming from hadronic showers versus p_T .

The photons have been corrected for the direct photon acceptance.

TABLE 5-3 Hadron acceptance (in % of initial hadrons) for various regions and cuts.

Cuts	SCG behind LGC	SCG behind AC	SF5 behind AC
$E_{AC}/\sqrt{E} > 0.15$	10.1	26.7	29.8
$\chi^2 < 0.05$	21.3	32.1	58.3
Both cuts	0.7	3.0	9.5

The scaling was checked using the 30 GeV pion data, by multiplying their energy distributions in the glass by 2 and superimposing them to the corresponding distributions obtained by 60 GeV pions. The two distributions were identical within the statistical errors. After obtaining the p_T distributions for every hadron in each of the three regions of the glass from the Monte Carlo, each distribution was multiplied by the corresponding acceptances of table 5-2; the distributions of the charged hadrons were also increased by 30% to account for the tracking inefficiency, and they were also weighted by the probability of the hadron to interact in the glass. The absorption cross sections for the π^+ , π^- , K^+ , K^- , p and \bar{p} were taken from reference 45, while the neutron cross section was taken from reference 46.

The calculated ratio of the number of fake photons from hadrons over the number of pizeros, corrected for the direct photon acceptance, is shown on figure 5.3 as a function of P_T .

5.3 Timing cuts

Given that E705 was running at an interaction rate approaching 1 MHz, it was possible for the trigger to be affected by pile-up of energy deposition. The duration of the pulses from the main array blocks was of the order of 200 nsec. Consequently, the energies deposited in

the blocks from one interaction added to the energies of another interaction, if the latter occurred less than 200 nsec from the former, increasing the energy of a cluster seen by the Cluster Finder and the calculated p_T .

In order to remove such triggers the information from the glass TDCs was used. The TDCs measured the difference between the time that energy was deposited in a block and the time that the interaction occurred, so that energy depositions occurring out of time could be easily recognized.

Figure 5.4, showing the time distribution of the glass blocks for the 30 GeV electron calibration beam, gives a measurement of the time resolution obtainable from the glass signals. All blocks are in time with the beam trigger, as expected. Figure 5.5 shows the time distribution obtained from the high p_T photon triggers. The presence of energy depositions taking place before or after the recorded interaction is quite visible. The observed structure is caused by the 53.1 MHz RF structure of the accelerator. The peaks due to out of time events are getting smaller with the distance from zero, since the closer in time the spurious interactions are to the triggering one, the more energy is left in the calorimeter and therefore the higher the probability is for them to give a photon trigger.

The showers that had, from at least one of the blocks of the cluster, a time greater than ± 10 nsec were rejected as out of time. The percentage of events surviving the out of time cut is shown in table 5-4, for the minimum bias and the p_T triggers. The probability of rejecting a direct photon or a pizero event was assumed to be equal to the probability of rejecting a minimum bias interaction trigger. A correction was done to the normalizations to account for the events lost due to the timing cut.

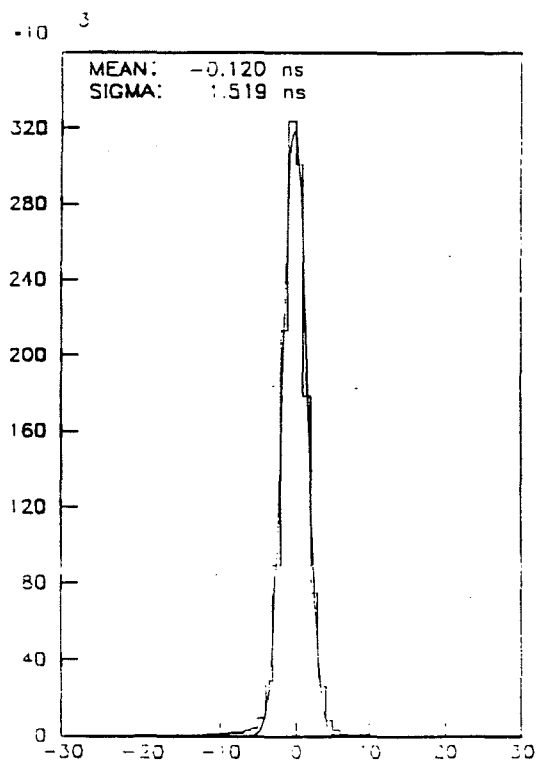


Figure 5.4 Time distribution in nsec for 30 GeV electron calibration events.

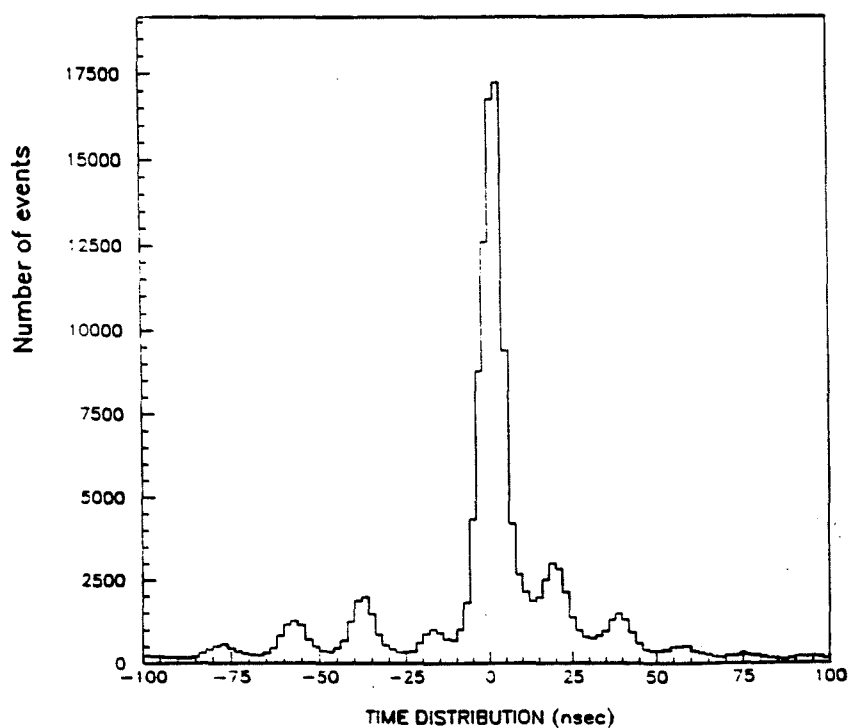


Figure 5.5 Time distribution of highest p_T shower for photon triggers. The structure corresponding to the accelerator RF is clearly visible.

TABLE 5-4 Percentage of triggers surviving the out of time cut.

Trigger type	Negative beam	Positive beam
Interaction	71.5	70.2
PT2	62.3	58.7
PT3	63.6	63.4
PT4	48.3	47.3

5.4 Muon rejection

Another important source of background to the direct photon signal was due to the muon beam halo, which, coming parallel to the beam, could radiate a photon while crossing the magnet steel and hit the calorimeter at a large impact parameter. Since the p_T was calculated assuming the shower was coming from the center of the target the apparent p_T was enough to trigger.

In order to reduce such a background, spoiler magnets were used to reduce the number of halo particles coming with the beam. Moreover, most of the interactions occurring in the presence of a halo muon were removed by the veto counters. Still, some were accepted either due to inefficiency of the counters or because they occurred in an out of time RF bucket, in spite of the timing cut described in the previous section.

The photon of the bremsstrahlung muon showers on the glass while the muon continues and hits the muon counters. The photon producing a good electromagnetic shower and having an apparent p_T more than 4 GeV/c is a single photon candidate. In order to

eliminate these events a cut was made, requiring no hit in the muon counters right behind the area of the triggering shower. The effect of this cut on the single photon candidates is shown in figure 5.6. The two plots show the p_T versus the Feynman x_F distribution of single photon candidates before and after the cut. The events at negative x_F and (unphysically) large p_T due to the photons from the bremsstrahlung muons hitting a specific region of the calorimeter, have been eliminated in the second plot.

Figure 5.7 shows a muon bremsstrahlung event as seen by the E705 Display program. The display shows the top view of the calorimeter and the muon planes. The hits in the scintillating counters of the muon planes behind the calorimeter are noted as small paddles. The blocks of the calorimeter are shown as pyramids with heights proportional to the deposited energies. The counters in all three muon planes (MU1, MU2, MU3) are lit up right behind the high p_T shower.

5.5 Neutral mesons

The neutral mesons π^0 and η were detected through their 2γ decaying modes. The branching ratios for $\pi^0 \rightarrow 2\gamma$ and for $\eta \rightarrow 2\gamma$ are 98.798 % and 38.9 % respectively.^[47]

The candidate meson invariant mass was calculated by combining the triggering shower with any other electromagnetic shower in an event using the formula:

$$m = [2 E_1 E_2 (1 - \cos\theta)]^{1/2}$$

where E_1, E_2 are the energies of the two photons as measured by the calorimeter and θ the opening angle between them. The angle θ was calculated using the measured positions of the photons from the hodoscopes and the reconstructed vertex. The pizero and eta mean lifetimes are very short ($\sim 10^{-16}$ sec) so their decays are very close ($\sim 10^{-6}$ cm) to the vertex.

The cuts applied to each one of the two showers were the following:

- a) To be within 10 nsec of the time of the interaction.

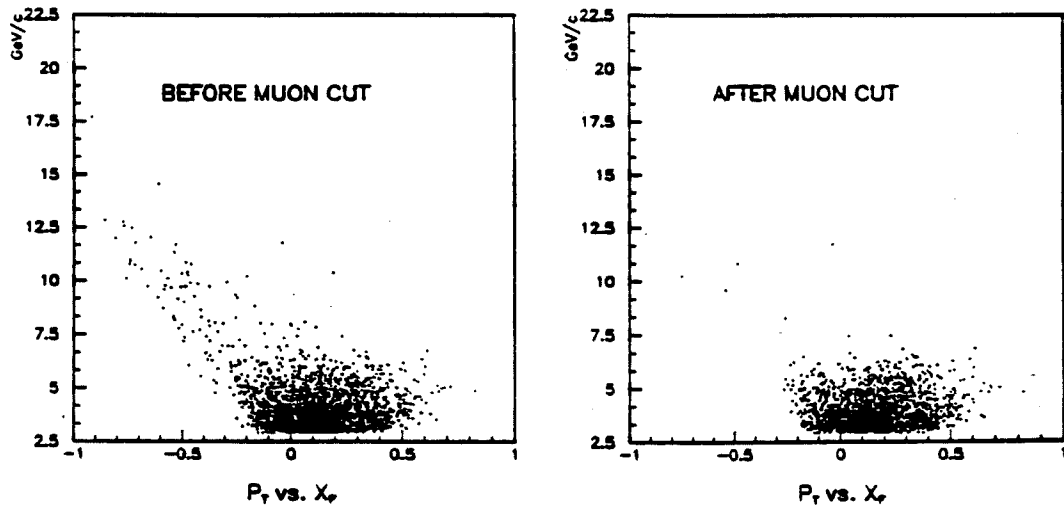
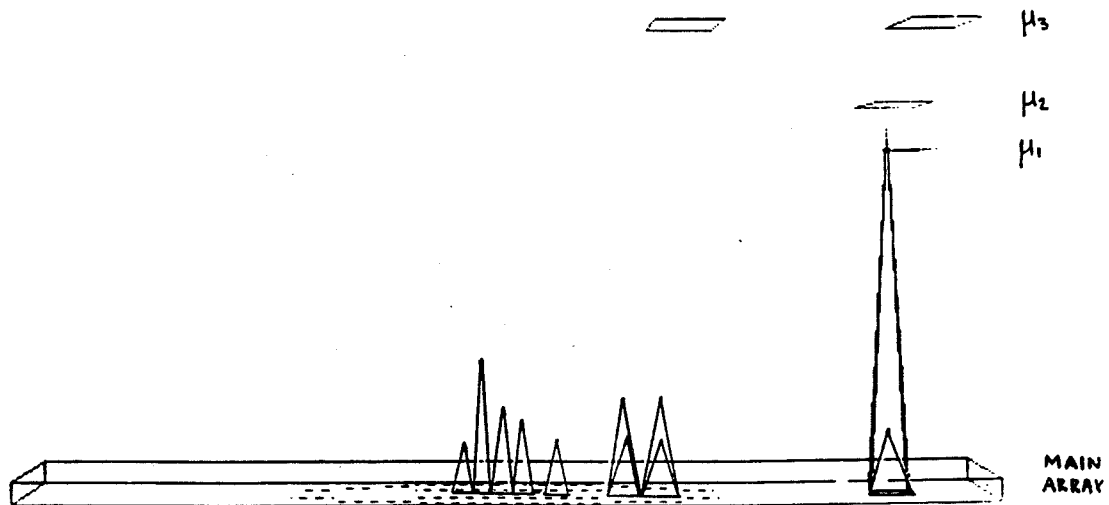


Figure 5.6 p_T versus x_F of single photon candidates before and after the muon cut.



Trigger PT4

Tape 5424

Event 3856

1/07/88 6:49

Figure 5.7 Muon bremsstrahlung event as seen by the E705 Display program.

- b) $E_{AC}/\sqrt{E} > 0.15 \text{ (GeV)}^{-1/2}$, where E_{AC} , E are the active converter and total energy respectively.
- c) Energy greater than 2 GeV.
- d) $\chi^2 < 0.05$
- e) $\Delta r > 8 \text{ cm}$, where Δr is the distance from the shower center to the closest track reconstructed.
- f) $p_T > 3 \text{ GeV}/c$ where p_T is the total transverse momentum of the pair.

Figure 5.8 shows the $\gamma\gamma$ invariant mass distribution obtained from all p_T triggers. The pizero and eta masses were fitted to a gaussian, and the background to an exponential. The results of the fits gave a mean $134.3 \pm 0.8 \text{ MeV}/c^2$ for the mass of the pizero and $542.4 \pm 3.9 \text{ MeV}/c^2$ for the eta, to be compared to the known values of 134.9626 ± 0.0039 and $548.8 \pm 0.6 \text{ MeV}/c^2$ respectively. Remembering that the energy scale had been set by the E/p ratios, the pizero mass was found in agreement with the expected value while the eta mass differed by 1.16%. Consequently, we assumed an uncertainty in the energy scale of the order of 1.0% which was included among the systematic errors (see chapter 7). The sigmas of the Gaussians were $24.3 \pm 1.0 \text{ MeV}/c^2$ and $19.5 \pm 3.2 \text{ MeV}/c^2$ respectively. The worse resolution of the pizero is not due to the energy resolution but to an intrinsic limitation of the calorimeter. When the two photons from the pizero are closer than 7 cm (inside the same large block) then the energy sharing algorithm fails to calculate the two energies and it splits them equally. The effect of such occurrences is to broaden the pizero peak and to generate a tail to it. The effect can be seen even better by looking at figure 5.9, where the so called “asymmetry” of the pizero’s, defined as $(E_1 - E_2)/(E_1 + E_2)$, is plotted. In addition to the expected flat distribution over most of the asymmetry range one also observes the unphysical peak at 0 asymmetry, due to the artificial equipartition of the shower’s energy. In the case of the eta, the minimum opening angle is four times bigger than the pizero one, and consequently the sharing algorithm fails less often.

For the purpose of event counting, a pizero was defined as an event occurring in the band between 80 and 240 MeV/c² and for the eta, between 480 and 620 MeV/c². The background for the pizero was taken in the sideband between 280 and 440 MeV/c², and between 400 to 480 and 620 to 700 MeV/c² for the eta. The background was weighted by the ratio between the background events under the pizero (eta) peak and the events in the sidebands, as predicted by the exponential fit.

5.6 Single photons

Every photon that did not combine to the π^0 or η mass with another photon of the event was defined as a single photon. The cuts applied to identify the photons were the same as the ones given in section 5.5.

The single photon candidates were obtained for each of the two p_T triggers (only PT3 and PT4 were used in the analysis) and the four beam types. The events were divided in bins of p_T and x_F in the p_T range between 4. and 7. GeV/c and the x_F range between -0.25 and 0.35. The p_T and x_F were calculated taking into account the angle of the beam with respect to the z-axis.

The trigger efficiency for the single photons was defined as the average efficiency in a p_T bin. In the following j refers to the measured p_T of the single photon and i to the p_T of the triggering cluster. For a given bin j of $N_j = 8 \cdot N_{PT3,j} + N_{PT4,j}$ entries, the distribution of the p_T of the corresponding triggering clusters was formed; if n_i is the number of entries in a given bin i of this distribution then the average efficiency was calculated as:

$$\bar{\epsilon}_j(P_{T,\gamma}) = \frac{\sum_{i=1}^{N_b} \epsilon_i n_i}{N_j}$$

where ϵ_i is the trigger efficiency for the bin i as a function of the p_T of the triggering cluster (fig.3.12); the sum is over all the bins N_b of the distribution.

A fraction of the single photon candidates was coming from hadrons interacting in the calorimeter, misidentified as photons, and from pizeros and etas with one of their two photons not reconstructed, or both photons coalesced and reconstructed as one. The background due to pizero and eta decays was estimated with the Monte Carlo described in the next chapter and was subtracted from the single photon signal, while the hadron contribution was estimated and subtracted as from the discussion of section 5.2.

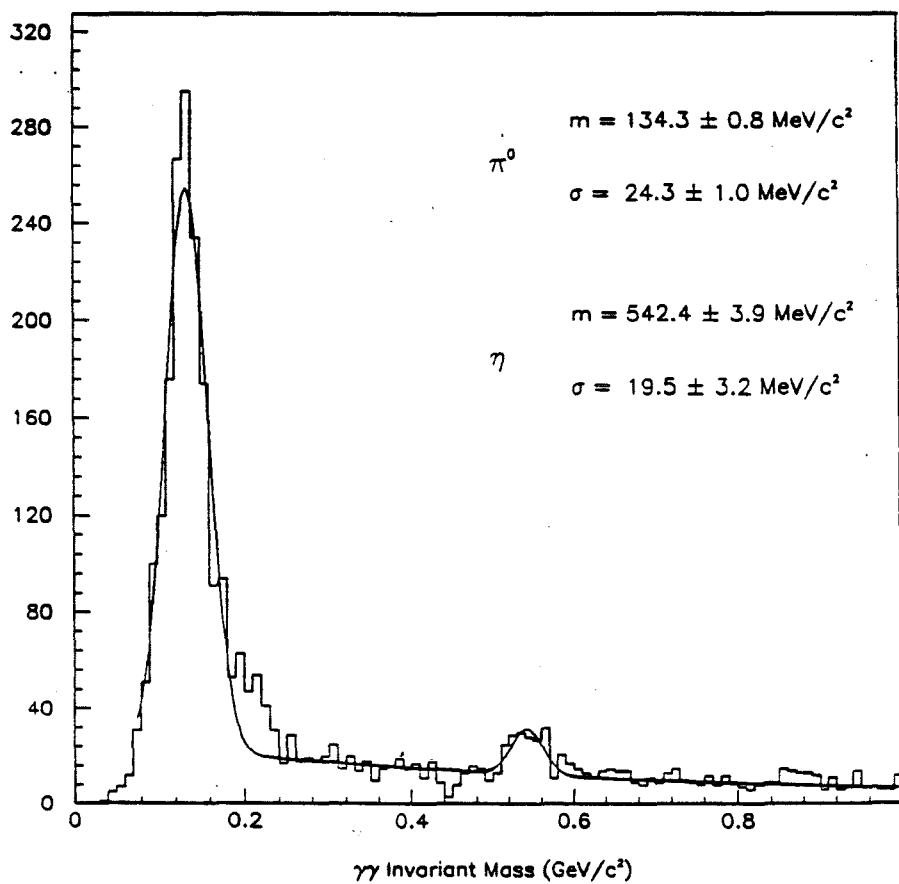


Figure 5.8 $\gamma\gamma$ invariant mass. The pizero and eta masses were fitted to gaussian distributions and the background to an exponential.

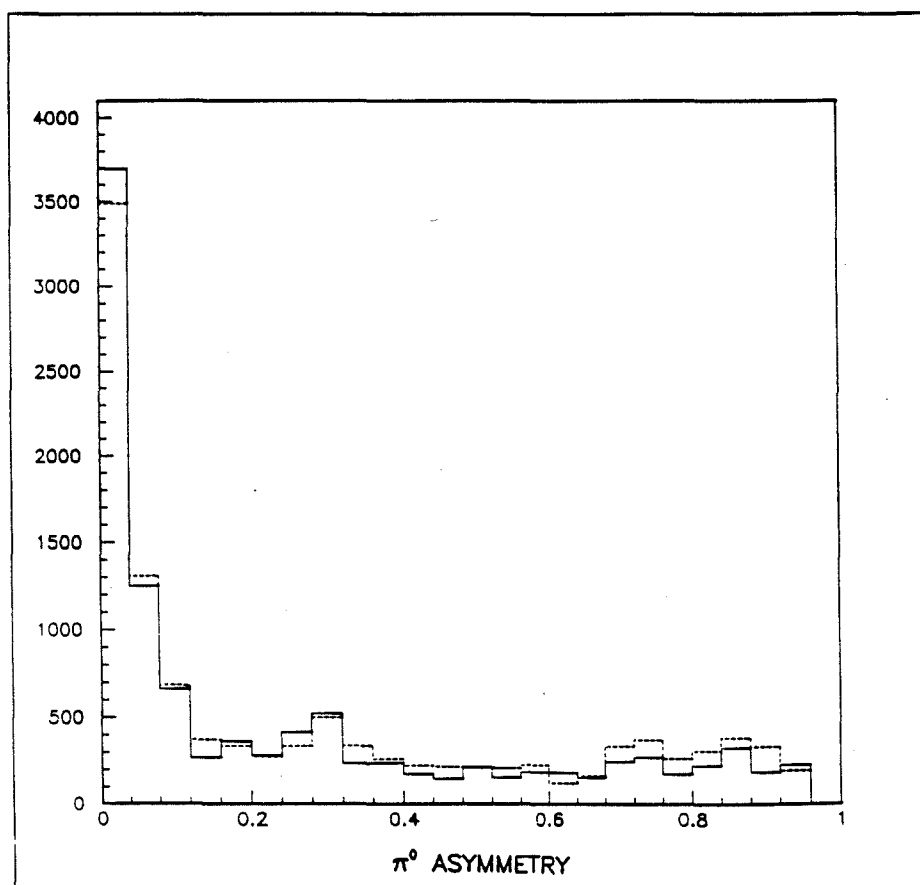


Figure 5.9 Asymmetry distribution of pizero. The dashed line is the Monte Carlo prediction.

Chapter 6

Monte Carlo

6.1 General

The geometrical acceptance of the spectrometer, the reconstruction efficiency of the analysis program and the effect of the various cuts had to be modeled in order to derive the physical kinematical distributions of the pizeros and the direct photons from the measured ones. Moreover, the background to the direct photon signal due to photons from unidentified π^0 and η decays had to be estimated. A Monte Carlo program was written to accomplish this. A general description of the program is given here, while the specific versions relative to the pizero and direct photon productions are described in the next sections.

The Monte Carlo consisted of three parts: a) The event generation and spectrometer simulation, b) The shower simulation on the calorimeter and c) The event reconstruction.

As a first step, π^0 's, η 's and direct γ 's were generated using flat p_T and x_F distributions. The π^0 's and η 's were allowed to decay isotropically in their center-of-mass to two photons. All produced particles were assigned x and y coordinates distributed in the target according to the x and y vertex distributions obtained by the E705 analysis. The z of the vertex was distributed according to an exponential taking into account the interaction length of the target. The photons were allowed to convert to an e^+e^- pair inside the target

according to a probability determined by the distance they traveled inside the target and by the radiation length of ${}^7\text{Li}$. If a photon converted then the π^0 (η) was considered lost and the other photon was allowed to contribute to the background of the direct photon signal. The non-converted photons were tracked through the spectrometer up to the calorimeter and their positions and energies were recorded. If the photons hit the coils or the steel of Rosie they were considered lost. The accepted photons were then allowed to shower in the calorimeter, the showering pattern being generated event by event by the EGS simulation program. The energies deposited in the LGC, the active converter and main array glass blocks were fed to the reconstruction program, which was the same as the one used to analyze real data. Such a procedure evaluates correctly the loss of events in a given bin of p_T and x_F , but does not estimate the possible migration of events in such bin from neighboring bins, due to the smearing of the measured energy and position. The number of migrating events depends on the distributions used initially to generate the particles. To account for such an effect, an iterative procedure was used. At the first iteration, each event was assigned a weight which was derived as being proportional to the measured cross section from experiment WA70, that was used as the best estimate. The new final and initial distributions resulting from the weighting process were divided to give the overall geometrical acceptance and reconstruction efficiency, which were used to correct the distributions from the data and to derive the cross sections. The new cross sections were then used to weight the initial and final distributions of the monte carlo, and the whole process was repeated, until the obtained cross sections differ less than 1% from the previous iteration.

6.2 Neutral meson geometrical acceptance and reconstruction efficiency

About 100,000 π^0 (η) were generated in the p_T range between 3 and 7.5 GeV/c and the x_F range between -0.35 and 0.45. Their photons were then showered on the calorimeter

with EGS and the resulting showers were fed to the analysis program. To take into account the separation efficiency of the hodoscopes, two peaks were generated in each view of the hodoscope only if the distance between them was such that they could be separated from the position determination algorithm, according to the separation efficiency obtained in section 4.5. If the two showers could not be separated in one (or both) view, only one peak was then defined in the corresponding view, with position equal to the average of the two photon positions and energy the sum of the two energies. If they could be separated, each peak was generated at the corresponding photon position, smeared according to the position resolution, with energy equal to the energy deposited in the detector by the photon shower. To account for inefficiencies of the calorimeter, the energy deposited in dead tubes or in blocks with bad phototubes was set to zero.

The events were then analyzed with the same reconstruction program as the one used on the real data, and the geometrical acceptance and the reconstruction efficiencies were determined. Tables 6-1 and 6-2 show the geometrical acceptance and the reconstruction efficiency for the pizeros in the same p_T and x_F range as the data. The geometrical acceptance is a strong function of x_F . The π^0 's with low x_F have less energy in the laboratory frame than the ones of higher x_F . The higher the energy of the pizero, the smaller the opening angle between the two photons, and therefore the smaller the probability to loose one photon outside the calorimeter. In the case of the reconstruction efficiency the opposite is true. The higher the p_T and x_F of the pizero (eta) the lower the efficiency is, since the opening angle becomes very small and the two showers can not be separated.

The loss of pizeros (etas) due to conversion in the target was 14.5%. The effects of the cuts of the reconstruction program were the following (the percentages are the remaining pizeros when the cuts are applied sequentially):

- a) 80% of the pizeros passed the active converter energy requirement: $E_{AC} > 0.2 \text{ GeV}$.
- b) 88% of the pizeros were not coalescing, i.e. two peaks were found in at least one view of the hodoscope.

c) Even if both photon peaks had been found in at least one view of the hodoscope, only 57% of the pizeros could have their positions reconstructed (see below).

d) 80% of the pizeros fulfilled the $E > 2 \text{ GeV}$ and $E_{AC}/\sqrt{E} > 0.15 \text{ (GeV)}^{1/2}$ requirements.

e) 74% of the pizeros passed the chisquared cut.

A major loss of pizeros was due to the energy asymmetry cut in the position finding algorithm described in section 4.6. In order for two peaks in the x (y) view of the hodoscope to be paired with one peak in the y (x) view, so that a cluster could be split into two showers, the energy asymmetry of each x-y peak pair was required to be less than 0.5. This cut was applied to eliminate accidental splitting of clusters when a fluctuation occurred next to a real single peak in one of the two views of the hodoscope. Unfortunately, such a necessary requirement could also lead to a loss of efficiency in reconstructing a pizero. In the case of the pizero (η), even in the case of two photons of similar total energy, the energy deposited by each photon in the hodoscope can fluctuate widely, leading to large differences in the recorded pulse heights. If the two peaks are also degenerate in one view (figure 6.1) then the cut in the asymmetry for one of the two peaks in a view with the single one in the other view could lead to its rejection as one of the two showers of the pizero (η). For all these cases, the remaining shower will contribute to the direct photon background (see next section).

The effect of the requirement that there were no charged tracks within a distance of 8 cm from the center of each shower was also estimated with the Monte Carlo, using the PYTHIA event generator. The loss due to this cut was a function of the x_F of the pizero and it increased from 0 to 15% for x_F ranging between -0.25 and 0.35.

Figures 6.2a-d show the good agreement between the Monte Carlo (solid lines) and the data (dotted lines), in the mass, separation distance, energy and χ^2 distributions of the pizero's.

TABLE 6-1 Pizero geometrical acceptance (in %) in bins of p_T (GeV/c) and x_F .

p_T x_F	-.25 : -.15	-.15 : -.05	-.05 : .05	.05 : .15	.15 : .25	.25 : .35
4. - 4.25	21.5	43.2	67.2	98.0	99.7	99.8
4.25 - 4.5	29.5	44.3	67.6	98.0	100.0	100.0
4.5 - 4.75	30.9	49.4	65.0	98.5	99.5	99.7
4.75 - 5.	30.9	49.5	67.7	96.5	99.8	100.0
5. - 5.25	38.2	42.7	66.1	96.8	100.0	100.0
5.25 - 5.5	35.6	46.8	66.5	97.7	100.0	99.9
5.5 - 5.75	39.4	44.4	69.7	96.0	100.0	100.0
5.75 - 6.	35.8	50.0	67.5	95.7	99.6	99.6
6. - 6.25	39.5	50.1	66.6	94.7	100.0	99.8
6.25 - 6.5	40.2	49.8	68.0	94.3	100.0	100.0
6.5 - 6.75	43.8	52.5	67.0	94.3	99.7	100.0
6.75 - 7.	41.4	51.1	67.5	94.9	99.6	99.9

TABLE 6-2 Pizero reconstruction efficiency (in %) in bins of p_T (GeV/c) and x_F .

p_T x_F	-.25 : -.15	-.15 : -.05	-.05 : .05	.05 : .15	.15 : .25	.25 : .35
4. - 4.25	26.8	38.5	27.7	20.0	23.9	20.5
4.25 - 4.5	27.9	39.9	27.5	20.9	24.6	23.5
4.5 - 4.75	33.2	37.7	28.3	20.0	23.4	22.2
4.75 - 5.	36.6	37.1	26.1	20.8	21.2	23.1
5. - 5.25	31.3	42.5	26.7	20.6	20.0	20.8
5.25 - 5.5	36.3	36.0	26.3	21.2	17.4	22.1
5.5 - 5.75	35.5	37.6	24.8	21.6	16.8	21.3
5.75 - 6.	39.1	32.1	26.8	21.7	16.3	20.5
6. - 6.25	38.6	32.4	27.0	20.7	16.9	19.0
6.25 - 6.5	37.6	32.7	26.0	20.1	16.5	18.5
6.5 - 6.75	37.6	33.1	26.4	20.7	16.3	17.4
6.75 - 7.	41.2	34.4	26.1	21.3	16.4	15.5

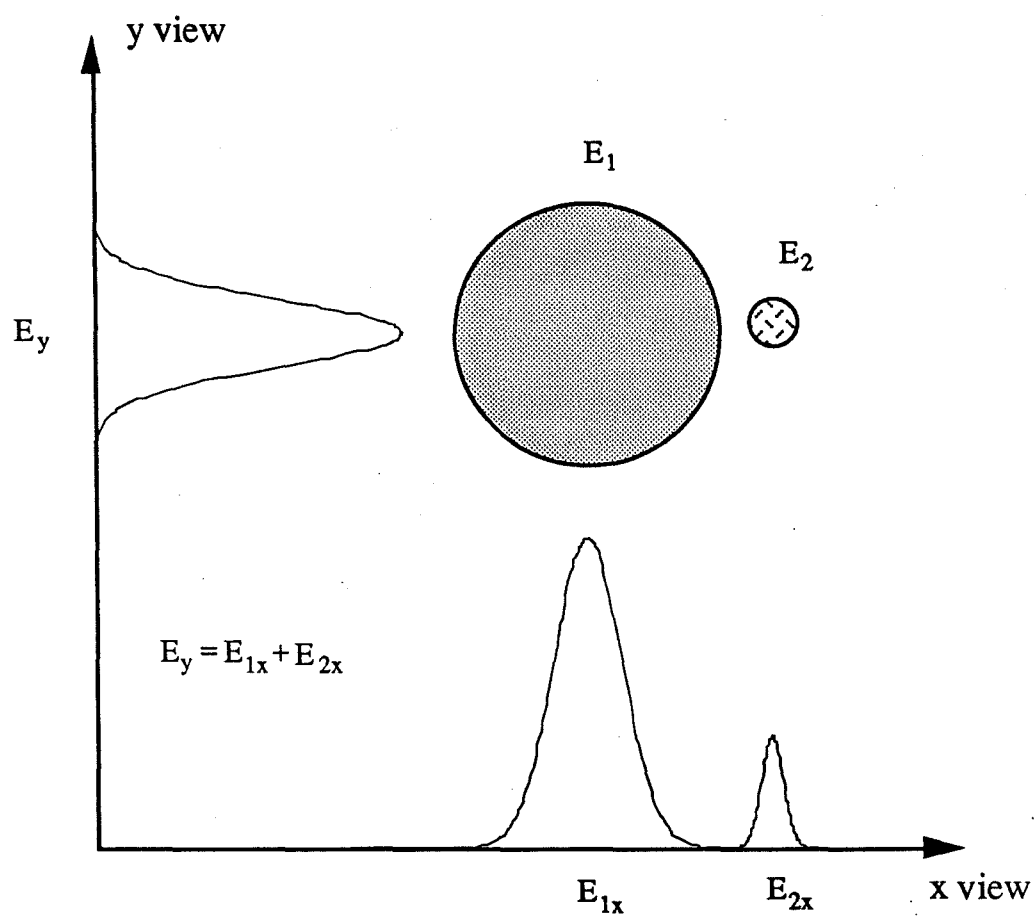


Figure 6.1 Two photon showers of a pizero decay on the LGC. The two showers degenerate into a single peak in the y view. E_1 and E_2 are the shower total energies and E_{1x} and E_{2x} the energies they deposited in the LGC.

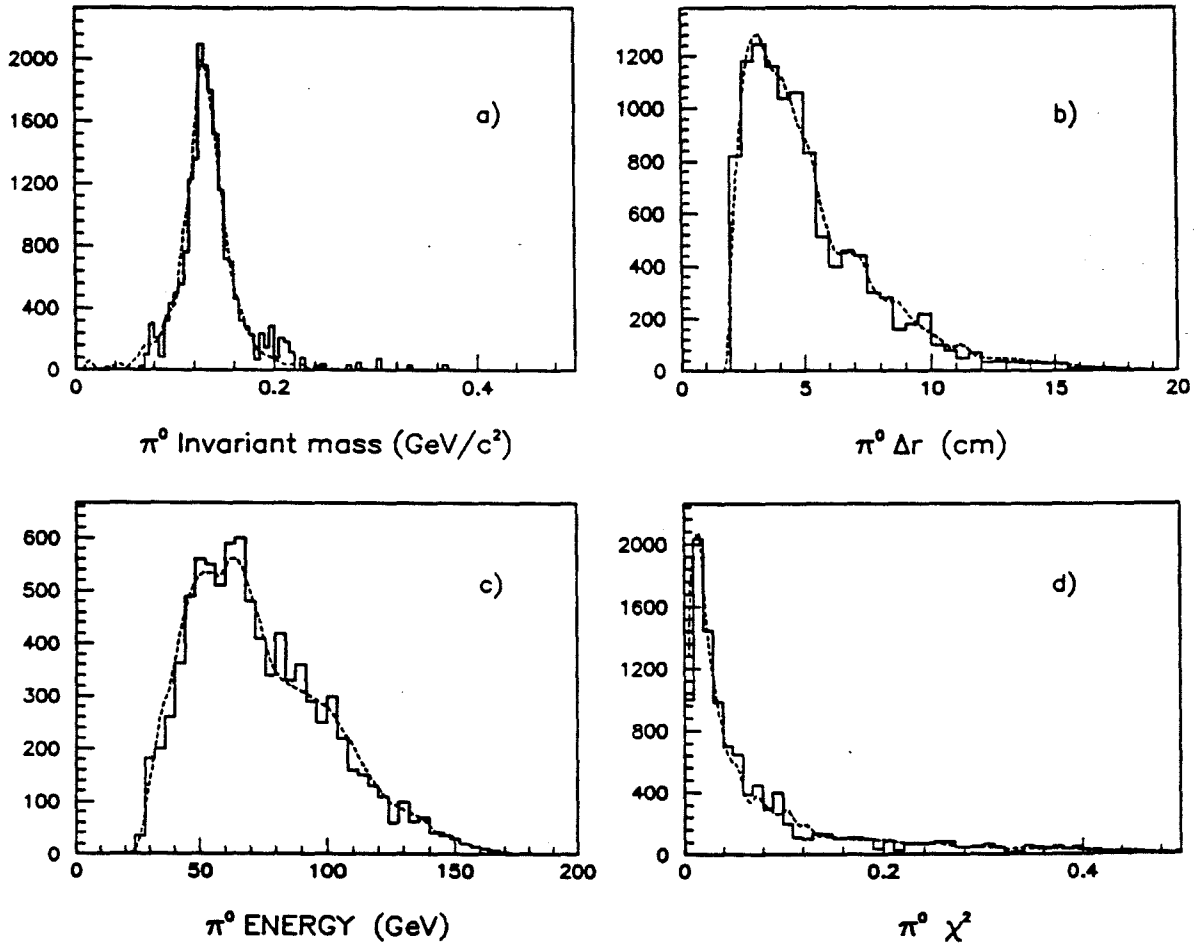


Figure 6.2 Comparison between the Monte Carlo predictions (dotted lines) and the measured π^0 distributions (solid lines). The plots show the mass (a), separation distance of the two photons on the hodoscopes (b), energy (c) and χ^2 distributions (d).

6.3 Single photon background from neutral meson decays

The major background to the direct photon signal came from the pizero and eta decays in which only one of the two photons was reconstructed, the loss of the other photon occurring in any of the ways described in the previous sections. The contribution to the background from other particles decaying to photons (η' , ω ...) was less than 1%, because of the branching ratios of these decays and the limited phase space.

Figure 6.3 shows the ratio of the fake photons from non-reconstructed pizeros and etas over the number of produced pizeros (solid line (a)) as a function of p_T .

The low energy photons of asymmetrically decaying pizeros could miss the calorimeter when the other photon hit it. The accepted photon contributed to the direct photon background mostly at low p_T (dotted line (e) in fig. 6.3).

The photons of high energy pizeros (high p_T , high x_F) had small opening angles resulting in small separation distance on the hodoscope. If the photons were coalesced in both views of the hodoscope, they were reconstructed as a single shower. Not all of these cases contributed to the direct photon background. When dealing with a coalescing π^0 , the energy deposited in the glass blocks behind the hodoscope does not fit in general the lateral energy distribution of a single shower. A cut in the chisquared of the reconstructed shower reduced considerably such a background (figure 6.4). The contribution of the coalesced showers to the direct photon background is shown in figure 6.3 (dashed line (c)).

The highest contribution to the background of the direct photons came from pizeros which lost one photon because of conversion to an e^+e^- pair in the target, or because of reconstruction cuts, like the minimum energy requirement of 2 GeV and the energy asymmetry cut in the matching of two peaks of the hodoscope (dashed-dotted line (b) in fig. 6.3).

The sum of all possible contributions from the eta decay to two photons is also shown in figure 6.3 (dashed line (d)). The overall effect is much smaller than the one of the pizero,

mostly because of the smaller cross section for η production (48% of the pizero cross section^[48]) and the lower branching ratio of the η decay to two photons (38.9%).

6.4 Single photon acceptance and reconstruction efficiency

The single γ acceptance and reconstruction efficiency were estimated with a procedure similar to the one executed for the study of the pizeros. Single photons were generated with flat p_T and x_F distributions. The photon showers on the calorimeter were simulated with EGS. The events were generated in bins of p_T and x_F , from 3 to 7.5 GeV/c in p_T and -0.35 to 0.45 in x_F . The events were then reconstructed by the analysis program and the geometrical acceptance and reconstruction efficiencies were studied.

The geometrical acceptance for the region of p_T and x_F over which events were generated was about 98%. Figures 6.5a-c show the effect of various cuts as a function of p_T . Figure 6.5d shows the overall acceptance and reconstruction efficiency.

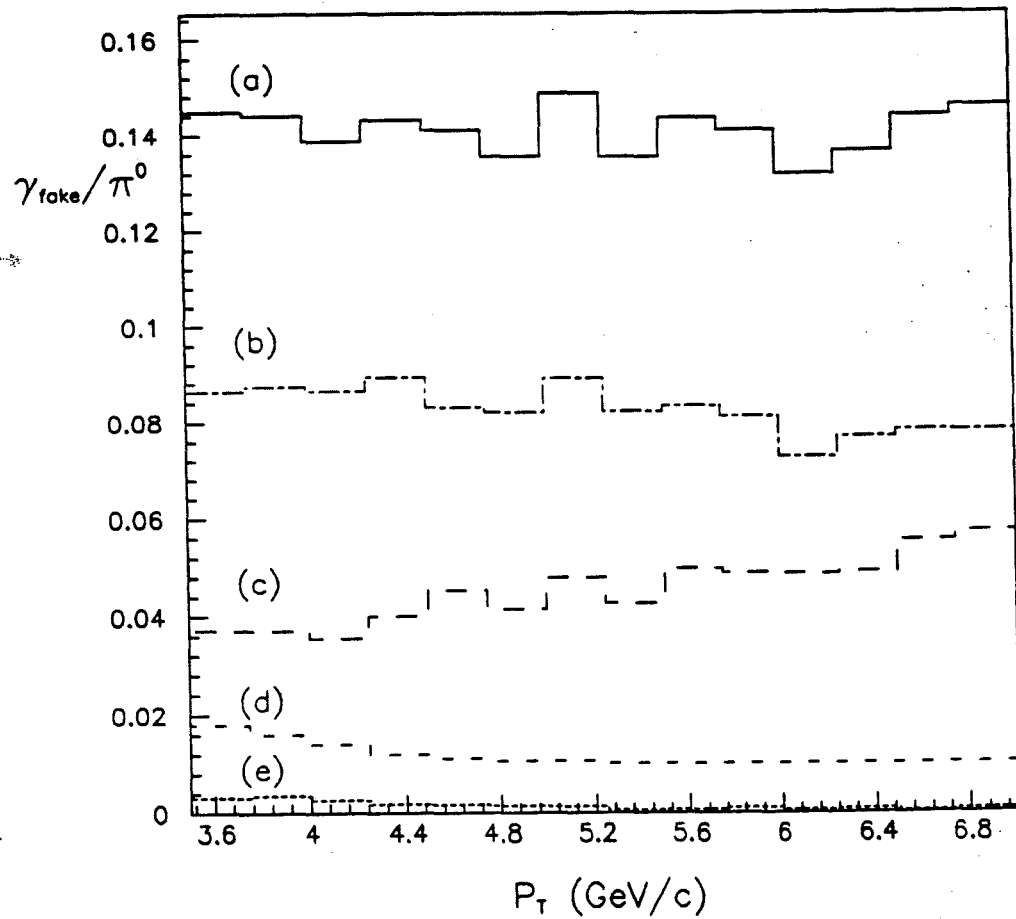


Figure 6.3 Direct photon background from pizeros and etas. The solid line (a) is the total $\gamma_{\text{fake}}/\pi^0$ ratio as a function of p_T . The other lines are the contributions to the overall background due to geometrical acceptance (e), coalescing pizeros (c), reconstruction cuts (b), and the eta decays to two photons (d).

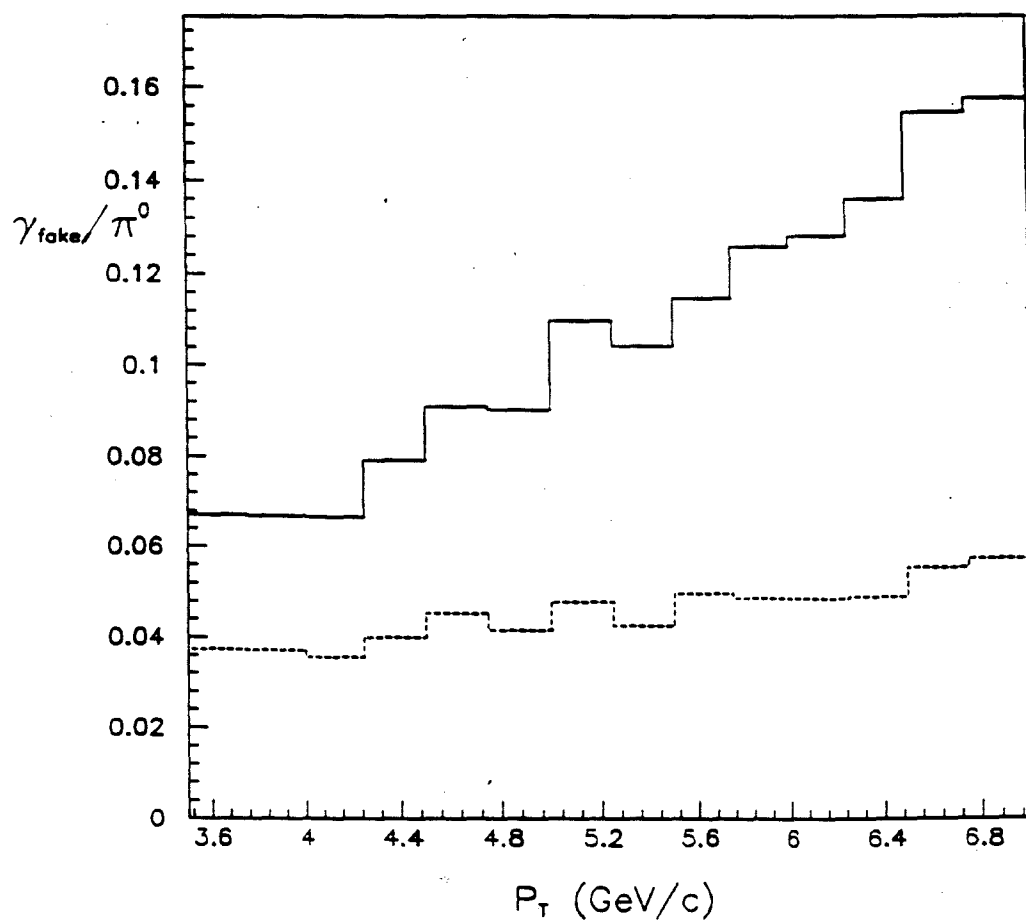


Figure 6.4 $\gamma_{\text{fake}}/\pi^0$ ratio for coalescing pizeros, before (solid line) and after (dotted line) the chisquared cut.

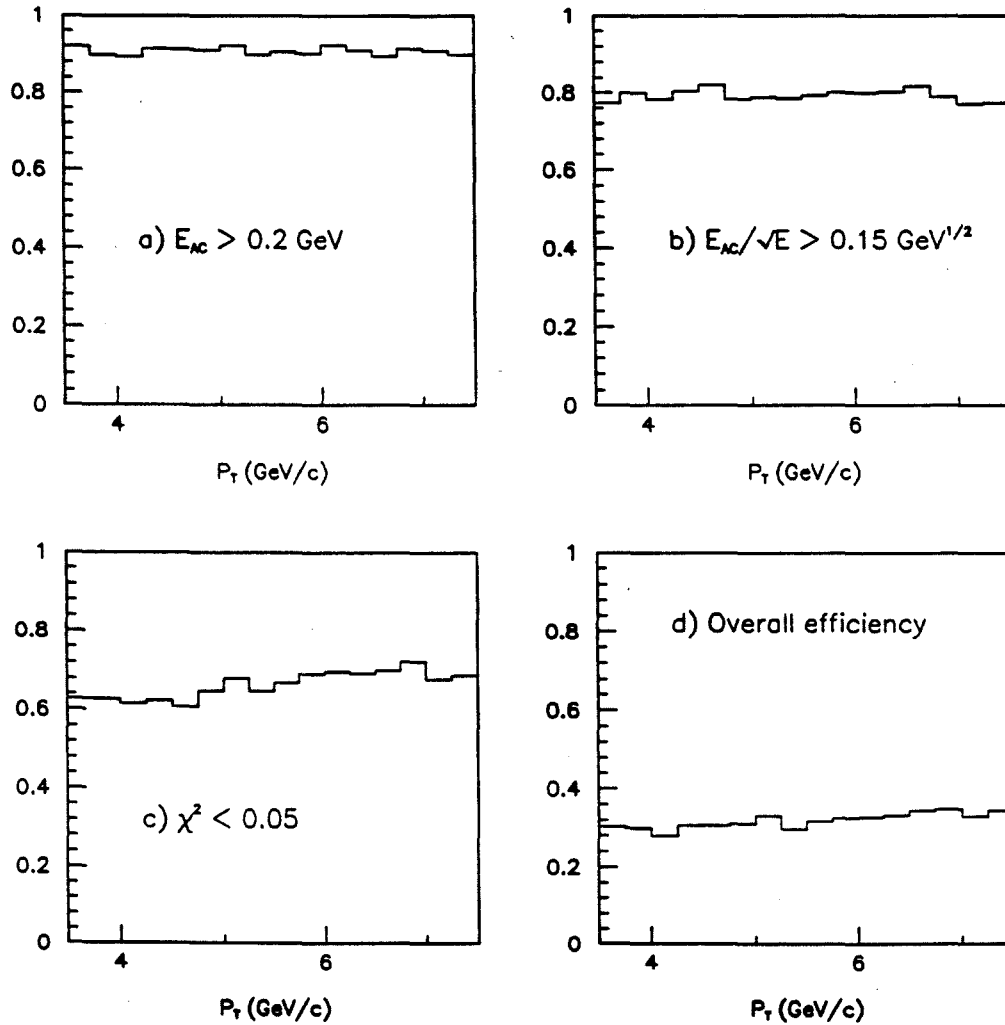


Figure 6.5 Reconstruction efficiency for single photons as a function of p_T after the active converter energy E_{AC} greater than 0.2 GeV cut (a), the $E_{AC}/\sqrt{E} > 0.15$ (GeV)^{1/2} cut (b), and the $\chi^2 < 0.05$ cut (c). The total reconstruction efficiency, after all cuts, is shown on plot (d).

Chapter 7

Results and conclusion

7.1 Cross section normalizations

The invariant cross section per nucleus for the inclusive production of a particle X of the type beam+target \rightarrow X+anything is given by:

$$E \frac{d^3\sigma}{dp^3} = \frac{A}{N_B N_A \lambda (1 - e^{-\ell\rho/\lambda})} \frac{N_i}{p_T \Delta p_T \Delta p_z \Delta\phi}$$

which becomes in terms of p_T and x_F

$$E \frac{d^3\sigma}{dp^3} = \frac{A}{N_B N_A \lambda (1 - e^{-\ell\rho/\lambda})} \frac{N_i x_0}{p_T \Delta p_T \Delta x_F \Delta\phi} \quad x_0 = \sqrt{x_T^2 + x_F^2}, \quad x_T = \frac{2p_T}{\sqrt{s}}, \quad x_F = \frac{2p_z^*}{\sqrt{s}}$$

where:

- A is the atomic weight of the target.
- N_A is the Avogadro's number .
- ℓ is the length of the target.
- λ is the absorption length of the target.

- ρ is the target's density.
- N_B is the number of the incident beam particles corrected for the various dead times.
- N_i is the number of observed particles (π^0 , single photons) corrected for geometrical acceptance, trigger and reconstruction efficiencies in the volume element of the phase space $\Delta p_T \Delta x_F \Delta \phi$.
- p_T, p_z^* are the components of the momentum of the particle in the center of mass of the interaction.
- \sqrt{s} is the total energy of the interaction in the center of mass.

The values of the first six factors for the negative and positive pion beams are shown in table 7-1.

The number of incident beam particles was determined in the intervals in which the experiment was “live” (“live beam”). The “live” beam was defined as the beam particles that did not coincide: a) with hits in the veto counters (see section 3.2), b) with the digitization, the read-out and the clearing of the electronics. The “live” pions and protons were corrected for the probability for two particles to occupy the same bucket and for the sagging in the electronics of the beam logic at high beam rates. The sum of the counts of the individual BY2 counters was linear with the beam rate, as determined from special studies done online during the run. Figures 7.1a,b show the number of π^- and π^+ per spill versus the sum of the BY2's. The linear part of the plot was fitted to a straight line, and then the measured pion flux was corrected to fall on the resulted line. This increased the live beam from 3.628×10^{11} to 4.717×10^{11} with an uncertainty of $\pm 7\%$ for the negative and from 3.5215×10^{11} to 3.8288×10^{11} with an uncertainty of $\pm 2.6\%$ for the positive. The live pions and protons were also corrected spill-by-spill for the dead time of the Cluster Finder strobe. The beam was also multiplied by 71.5% (negative) and 70.2% (positive) to correct for the interactions that were rejected due to the timing cut (see section 5.3).

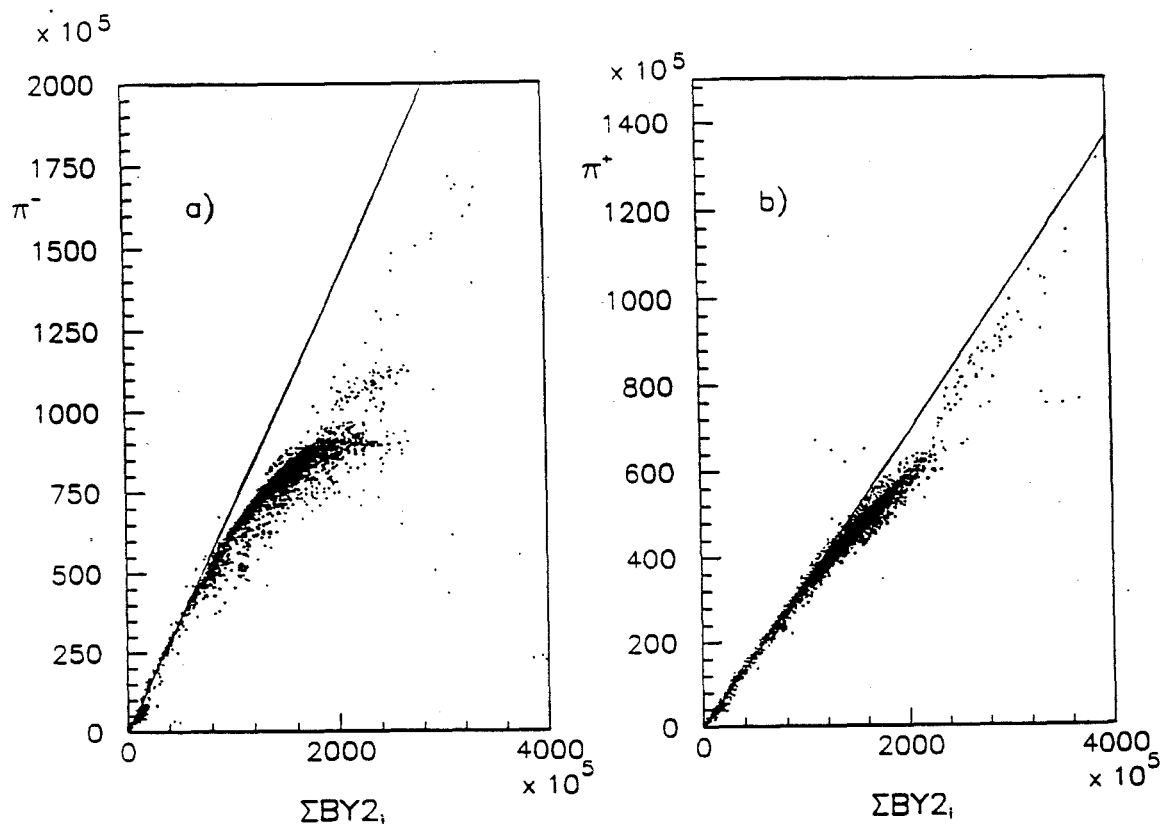


Figure 7.1 Number of π^- (a) and π^+ (b) per spill versus the algebraic sum of the BY2 counters.

TABLE 7-1 Cross section normalization factors.

Factor	π^-	π^+
A	6.94	6.94
N_A	$6.022 \times 10^{23} \text{ mol}^{-1}$	$6.022 \times 10^{23} \text{ mol}^{-1}$
ℓ	32.918 cm	32.918 cm
ρ	0.534 g/cm ³	0.534 g/cm ³
λ	100.46 g/cm ²	99.89 g/cm ²
Live beam	3.3727×10^{11}	2.634×10^{11}
$A/N_B N_A \lambda (1 - e^{-\ell \rho / \lambda})$	2.1189 pbarn	2.7144 pbarn

The contamination of the positive pion flux from kaons (see section 3.2) is estimated to be 10%. The π^0 inclusive cross section induced from kaons is 0.8 of the π^+ induced cross section^[49], which leads to an additional correction of 2.04%.

The results presented in this chapter were obtained from the analysis of about 20% of the data obtained by E705 over the whole running period.

7.2 Systematic errors

The principal systematic error in the determination of the pizero and direct photon invariant cross sections was due to uncertainty in the p_T scale. Small shifts in the p_T scale can lead to large shifts in the absolute normalization, due to the steep fall of the p_T distribution.

The error in the p_T scale can be calculated using the formula $p_T = E \sin \theta$, or, for small θ angles, $p_T = Er/z$. One then has:

$$\left(\frac{\Delta p_T}{p_T} \right)^2 = \left(\frac{\Delta E}{E} \right)^2 + \left(\frac{\Delta r}{r} \right)^2 + \left(\frac{\Delta z}{z} \right)^2$$

where r is the radial distance of the shower from the center of the glass and z is the distance of the position hodoscopes from the vertex. The estimated error of the energy scale was 1% (see section 5.5). The error of the z of the vertex is of the order of ± 1 cm which gives a $\Delta z/z$ ratio less about 0.1%. The error in the position of a shower due to the resolution of the hodoscope is of the order of ± 0.5 cm which leads to an average $\Delta r/r$ of about 1%. Consequently the percent error in the p_T scale is 1.4%.

The invariant section can be parametrized (see next section) as:

$$E \frac{d^3 \sigma}{dp^3} \propto \frac{1}{p_T^b}$$

which leads to a percent error of:

$$\left| \frac{\Delta \left(E \frac{d^3\sigma}{dp^3} \right)}{E \frac{d^3\sigma}{dp^3}} \right| = \frac{b \Delta p_T}{p_T}$$

where the exponent b was found to be 9.6 from a fit to the pizero data. Therefore the percent error in the cross section due to the uncertainty in the p_T scale was 13.4%.

Another source of systematic error in the cross section was the energy resolution of the calorimeter. Because of the steep fall of the cross section with p_T , the energy smearing due to the resolution moves more events from lower p_T to higher p_T than vice versa. This results in a change in the overall normalization, which can be corrected by taking the energy resolution into account in the Monte Carlo. The uncertainty in the energy resolution contributes by 12% to the systematic error of the cross section, as estimated by the Monte Carlo.

The error in the beam flux (see section 7.1) introduces an error of 7% and 2.6% in the negative and positive cross sections respectively.

So the overall systematic error in the cross sections, summing the errors of the previous effects in quadrature, was 19.3% for the π^- and 18.2% for the π^+ beam.

The systematic errors affect by the same amount both the pizero and the direct photon cross sections and consequently they cancel out in the ratio of γ/π^0 .

7.3 Pizero inclusive cross section

The invariant cross section per nucleon was calculated as a function of p_T and x_F , averaged over the p_T and x_F bins. The values of the cross section for $\pi^- + \text{Li} \rightarrow \pi^0 + X$ and for $\pi^+ + \text{Li} \rightarrow \pi^0 + X$ are shown in tables 7-2 and 7-3 respectively.

To calculate the cross sections per nucleon, the cross sections were scaled by $A^{1.1}$ where $A=6.94$ is the atomic weight for ${}^7\text{Li}$ and the 1.1 value for exponent was derived from the measurement of Fermilab experiment E629.[50]

The cross sections were fitted using the phenomenological form:

$$E \frac{d^3\sigma}{dp^3} = C \frac{(1-x_D)^n}{p_T^m} \quad (7.1)$$

where:

$$x_D = [x_T^2 + (x_F - x_0)^2]^{1/2} \quad \text{and} \quad x_F = \frac{2p_z}{\sqrt{s}}, \quad x_T = \frac{2p_T}{\sqrt{s}}$$

The values of the parameters C , n , m , x_0 of the fit and the chisquared per degree of freedom are shown in table 7-4.

Figure 7.2 shows the invariant cross section for $\pi^- + \text{Li} \rightarrow \pi^0 + X$ averaged over the whole x_F region as a function of p_T . Figure 7.3 shows the invariant cross section as a function of x_F for different p_T intervals. Figure 7.4 shows the invariant cross section for $\pi^+ + \text{Li} \rightarrow \pi^0 + X$ averaged over the whole x_F region as a function of p_T . The solid curves are the fitted functions averaged over the same p_T and x_F regions as the data.

The ratio of the cross section per nucleon for the π^+ and π^- beams is shown in figure 7.5. The expectation for the ratio to be independent of p_T because of isospin invariance is confirmed by the data, within the uncertainty due to the experimental errors.

Figures 7.6 and 7.7 show a comparison of the π^0 cross section with the corresponding results of experiments NA24^[51], WA70^[52], and NA3 for π^- and π^+ beams respectively. NA24 and E705 were running at the same center of mass energy ($\sqrt{s}=23.75$ GeV) and they seem to be in good agreement, while WA70 and NA3 were running at \sqrt{s} equal to 22.9 and 19.4 GeV respectively and their cross sections appear to be lower, as expected. Both data from E705 and NA3 were scaled down by $A^{1.1}$ to account for nuclear effects. To compare the data from different energies the invariant scale variable $x_T (=2p_T/\sqrt{s})$ can be used. Figures 7.8 and 7.9 show the invariant cross sections multiplied by $p_T^{9.6}$ versus x_T for the π^- and π^+ beams respectively. The dotted line is the fit to E705 data from (7.1).

TABLE 7-2 Inclusive cross section in pbarn/GeV²/nucleon for $\pi^0 + \text{Li} \rightarrow \pi^0 + X$ as a function of p_T (GeV/c) and x_F .

p_T min p_T aver p_T max	-0.2	-0.1	x_F 0.0	0.1	0.2	0.3
4.00	± 150.1	± 202.3	± 248.2	± 338.2	± 283.8	± 228.9
4.11	229.36	824.34	1314.70	1710.79	1559.80	914.22
4.25	± 44.3	± 159.1	± 253.7	± 330.2	± 301.0	± 176.4
4.25	± 142.4	± 129.8	± 136.0	± 176.2	± 155.0	± 135.1
4.36	151.14	475.94	563.31	696.48	842.60	499.68
4.50	± 29.2	± 91.9	± 108.7	± 134.4	± 162.6	± 96.4
4.50	± 72.6	± 81.1	± 112.8	± 128.3	± 100.7	± 78.9
4.61	162.12	352.36	460.17	503.09	263.66	184.95
4.75	± 31.3	± 68.0	± 88.8	± 97.1	± 50.9	± 35.7
4.75	± 45.7	± 52.5	± 72.4	± 72.5	± 82.1	± 62.7
4.86	96.72	127.34	160.79	116.36	330.58	113.28
5.00	± 18.7	± 24.6	± 31.0	± 22.5	± 63.8	± 21.9
5.00	± 20.4	± 28.3	± 24.3	± 21.8	± 26.6	± 17.8
5.20	54.94	119.97	77.82	71.52	57.26	43.79
5.50	± 10.6	± 23.2	± 15.0	± 13.8	± 11.1	± 8.5
5.50	± 15.3	± 6.3	± 15.9	± 13.2	± 7.6	± 14.0
5.70	12.80	12.52	25.69	28.23	10.44	12.28
6.00	± 2.5	± 2.4	± 5.0	± 5.4	± 2.0	± 2.4
6.00	± 3.2	± 3.1	± 0.8	± 4.4	± 0.9	± 1.0
6.32	3.60	5.22	2.12	0.81	1.19	0.37
7.00	± 0.7	± 1.0	± 0.4	± 0.2	± 0.2	± 0.1

<p>statistical error</p> <p>cross section</p> <p>systematic error</p>

TABLE 7-3 Inclusive cross section in pbarn/GeV²/nucleon for $\pi^+ + \text{Li} \rightarrow \pi^0 + X$ as a function of p_T (GeV/c) and x_F .

p_T min p_T aver p_T max	-0.2	-0.1	x_F 0.0	0.1	0.2	0.3
4.00 4.11 4.25		± 177.6 406.38 ± 74.8	± 332.2 1008.45 ± 185.7	± 538.8 2690.46 ± 495.2	± 397.3 1812.34 ± 333.6	± 343.6 805.30 ± 148.2
4.25 4.36 4.50	± 184.6 319.72 ± 58.8	± 117.5 315.76 ± 58.1	± 232.8 740.45 ± 136.3	± 302.2 1045.49 ± 192.5	± 260.0 826.53 ± 152.1	± 187.3 674.02 ± 124.1
4.50 4.61 4.75	± 138.7 310.23 ± 57.1	± 93.4 136.04 ± 25.0	± 143.3 477.01 ± 87.8	± 184.5 760.55 ± 140.0	± 133.9 337.80 ± 62.2	± 124.2 46.36 ± 8.5
4.75 4.86 5.00	± 83.9 145.28 ± 26.7	± 65.1 152.27 ± 28.1	± 86.5 244.61 ± 45.0	± 102.1 387.01 ± 71.2	± 127.3 74.74 ± 13.7	± 89.6 105.25 ± 19.4
5.00 5.20 5.50	± 20.4 33.94 ± 6.3	± 29.3 90.09 ± 16.5	± 33.2 79.55 ± 14.6	± 24.6 68.83 ± 12.7	± 38.7 21.22 ± 3.9	± 26.2 66.84 ± 12.3
5.50 5.70 6.00	± 2.2 3.82 ± 0.7	± 19.3 47.16 ± 8.7	± 20.3 54.43 ± 10.0	± 7.8 17.17 ± 3.2	± 2.8 6.19 ± 1.2	± 21.2 52.88 ± 9.7
6.00 6.32 7.00	± 3.6 4.89 ± 0.9	± 0.6 0.84 ± 0.2		± 1.0 2.64 ± 0.4	± 1.0 1.92 ± 0.4	

statistical error
cross section
systematic error

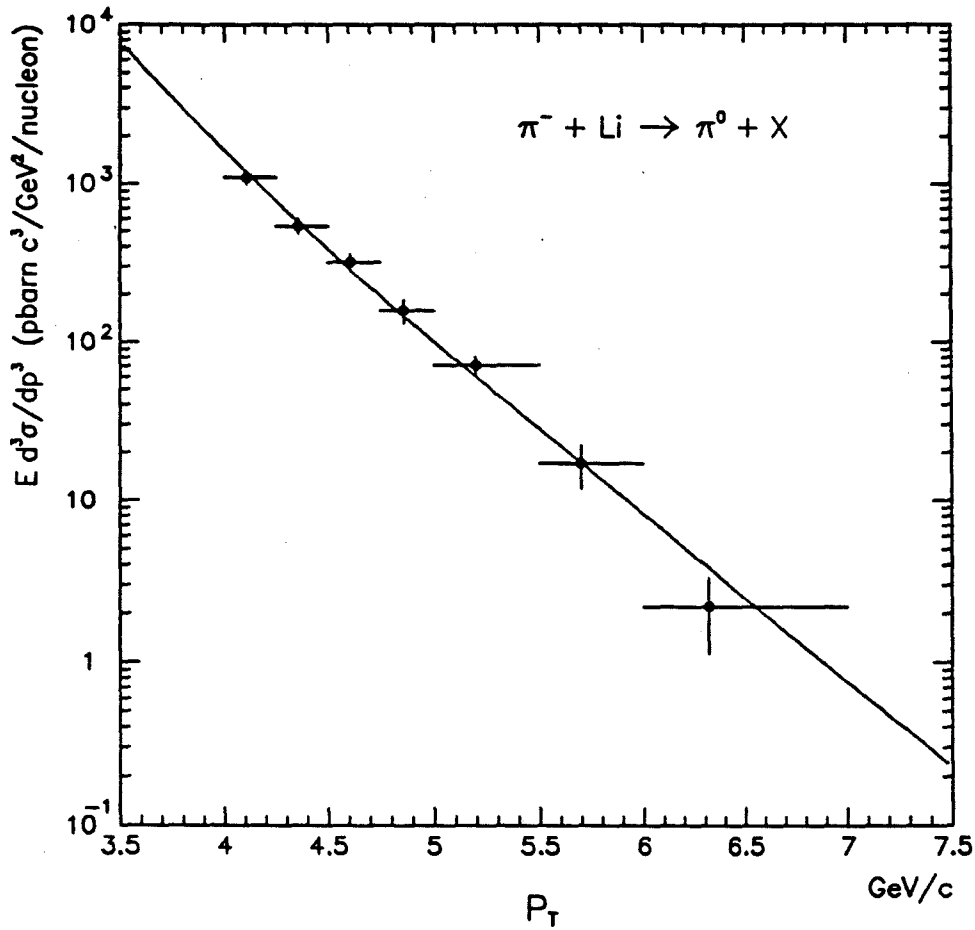


Figure 7.2 Invariant cross section for $\pi^- + \text{Li} \rightarrow \pi^0 + X$ as a function of p_T averaged over the full x_F range. Only the statistical errors are shown. The solid line is the fitted function averaged over the full x_F range.

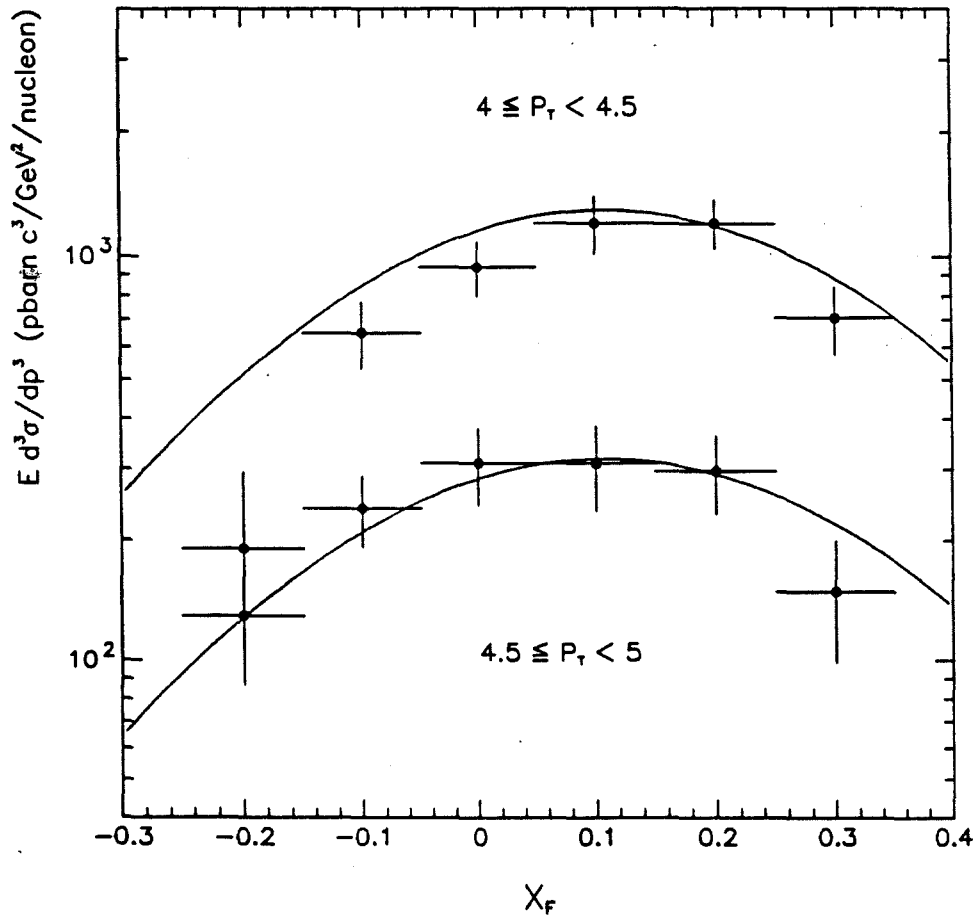


Figure 7.3 Invariant cross section for $\pi^- + \text{Li} \rightarrow \pi^0 + X$ as a function of x_F averaged over two ranges of p_T . Only the statistical errors are shown. The solid line is the fitted function averaged over the corresponding p_T ranges.

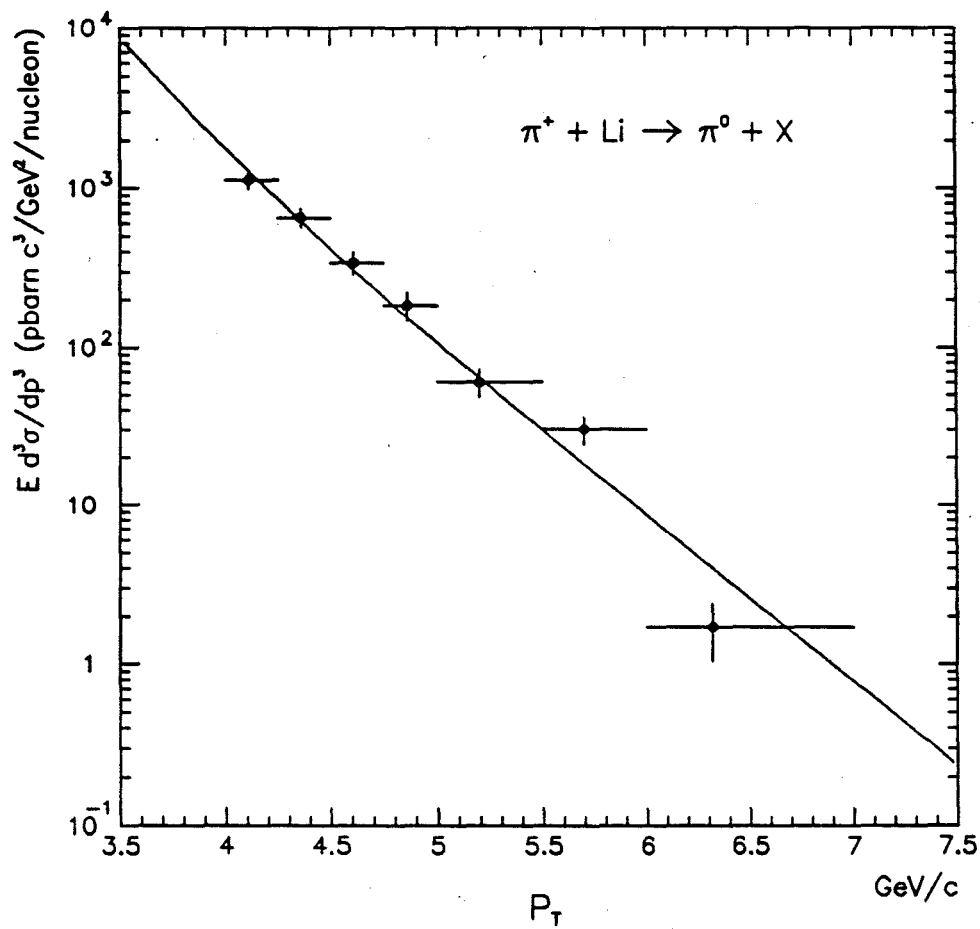


Figure 7.4 Invariant cross section for $\pi^+ + \text{Li} \rightarrow \pi^0 + X$ as a function of p_T averaged over the full x_F range. Only the statistical errors are shown. The solid line is the fitted function averaged over the full x_F range.

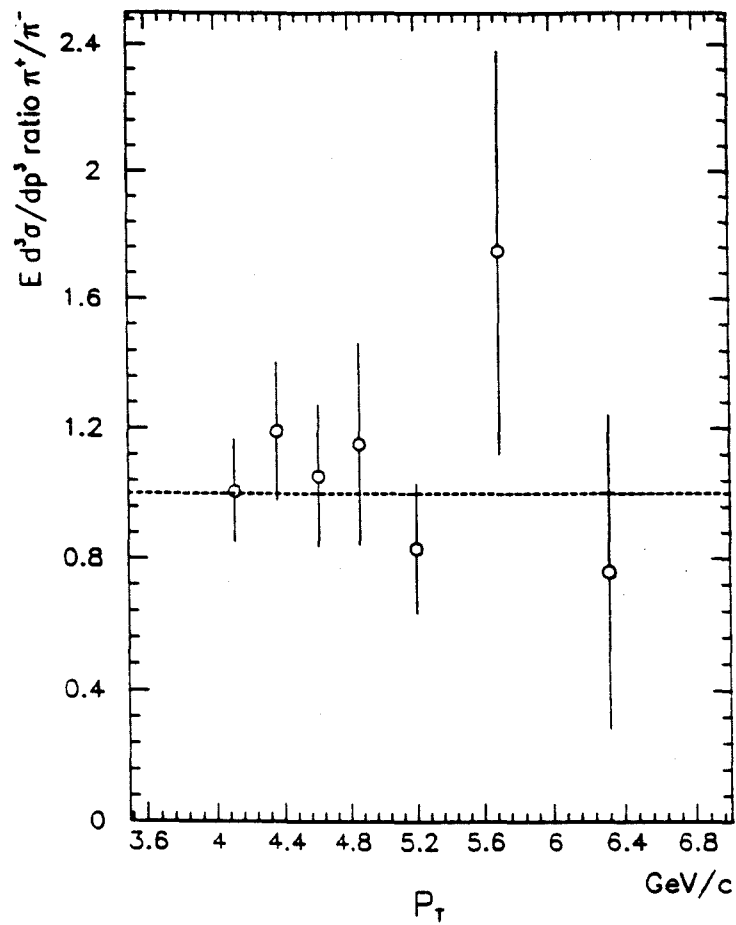


Figure 7.5 Ratio of π^+/π^- invariant cross sections of pizero production versus p_T .

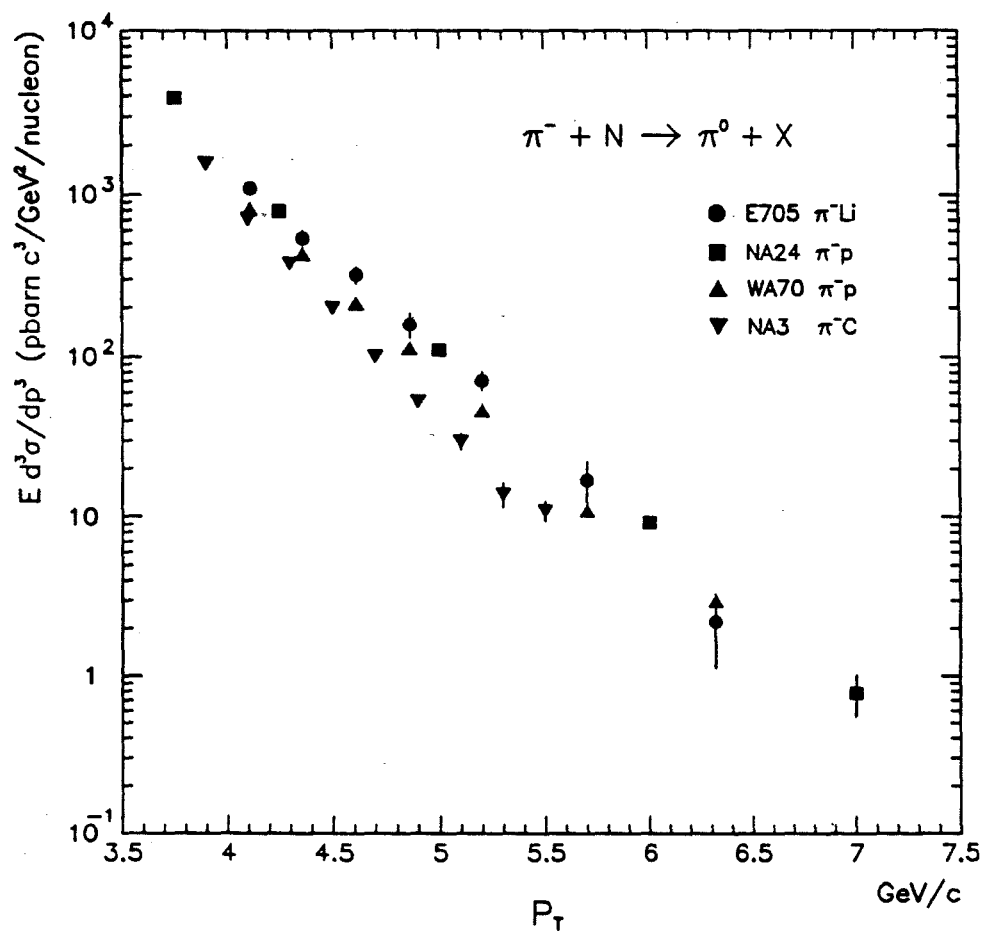


Figure 7.6 Comparison of the E705 $\pi^- \text{Li} \rightarrow \pi^0 X$ results with other published data. Cross sections from nuclear targets have been scaled by $A^{1.1}$.

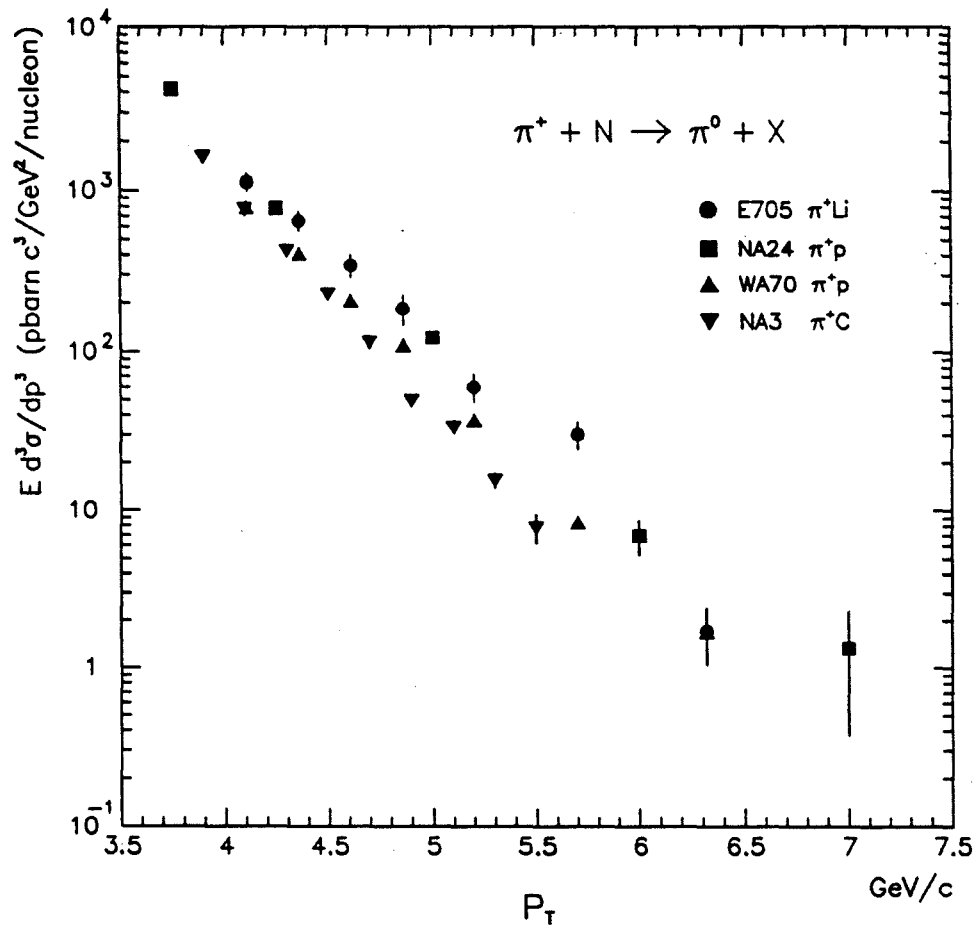


Figure 7.7 Comparison of the E705 $\pi^+ \text{Li} \rightarrow \pi^0 X$ results with other published data. Cross sections from nuclear targets have been scaled by $A^{1.1}$.

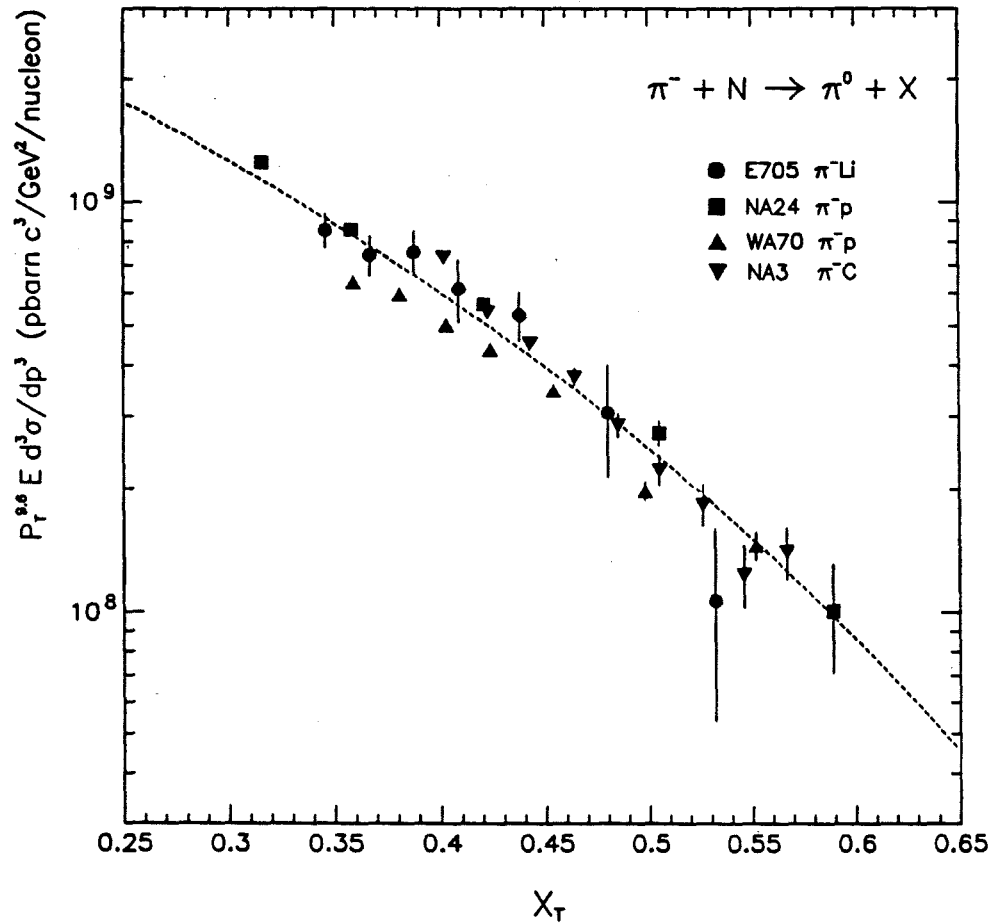


Figure 7.8 Pizero cross sections as a function of x_T , for π^- interactions. Cross sections from nuclear targets have been scaled by $A^{1.1}$. The line represents the fit of (7.1).

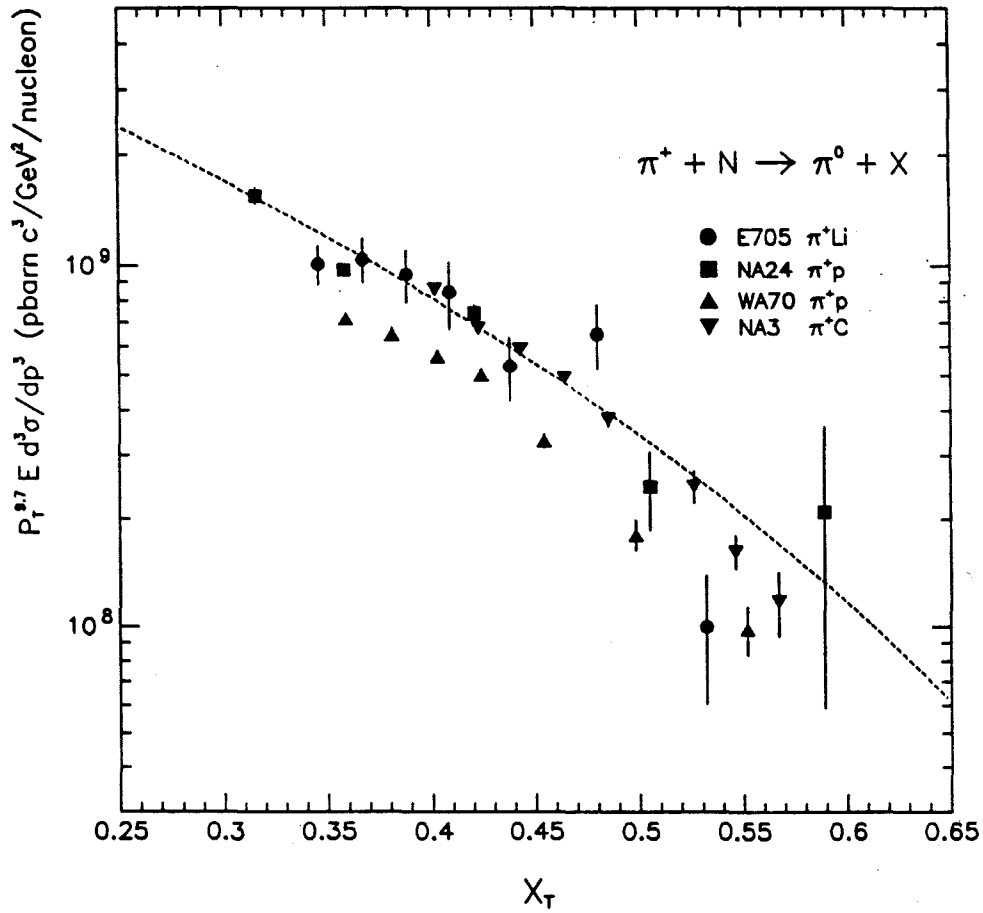


Figure 7.9 Pizero cross sections as a function of x_T , for π^+ interactions. Cross sections from nuclear targets have been scaled by $A^{1.1}$. The line represents the fit of (7.1).

TABLE 7-4 Parameters of the fit of the pizero invariant cross section.

	C (mb/GeV/nucleon)	n	m	x_0	χ^2/dof
$\pi^- + \text{Li}$	10.5 ± 4.2	4.8 ± 0.6	9.6 ± 0.3	0.11 ± 0.01	2.1
$\pi^+ + \text{Li}$	13.2 ± 7.1	4.8 ± 0.9	9.7 ± 0.4	0.10 ± 0.2	2.5

7.4 Direct photon cross section

The ratio of the direct photon to the pizero cross sections was estimated in bins of p_T according to :

$$\frac{\gamma}{\pi^0} = \frac{\epsilon_{\pi^0} e_{\pi^0}}{\epsilon_\gamma e_\gamma} \frac{N_{\gamma, \text{cand}}}{N_{\pi^0, \text{cand}}} - \frac{1}{\epsilon_\gamma} \left[\frac{N_{\gamma, \text{fake}}^{\pi^0}}{N_{\pi^0}} + \frac{N_{\gamma, \text{fake}}^\eta}{N_{\pi^0}} + \frac{N_{\gamma, \text{fake}}^{\text{hadr}}}{N_{\pi^0}} \right]$$

where ϵ_γ , ϵ_{π^0} are the geometrical acceptance and reconstruction efficiency for direct photons and pizeros respectively; e_γ , e_{π^0} are the trigger efficiencies for direct photons and pizeros respectively; $N_{\gamma, \text{cand}}$, $N_{\pi^0, \text{cand}}$ is the number of candidate direct photons and pizeros in the same data sample; the ratios in the parenthesis are the ratios of fake single photons from pizero, eta decays and interacting hadrons to produced pizeros, determined via the procedures previously described and shown in figures 6.2 and 5.3.

The background-subtracted production ratio γ/π^0 for the $\pi^- \text{Li}$ interactions is shown in figure 7.10. It is increasing with p_T as expected. The reason for this increase is that the π^0 is produced from the fragmenting partons and therefore its transverse momentum is a fraction of the parton transverse momentum, while in the case of direct photon no fragmentation is involved and all the transverse momentum characterizing the interaction among partons is carried by the outgoing photon. Consequently, the direct photon yield becomes higher and higher than the pizero one as the transverse momentum increases.

The direct photon cross section can then be derived by multiplying the production ratio γ/π^0 by the pizero inclusive cross section. The values of the ratio and of the invariant cross section are shown in table 7-5. Figure 7.11 shows the direct photon invariant cross section as a function of p_T . The lines are the predictions of the optimized scale calculation, with the Duke and Owens structure functions sets 1 (solid line) and 2 (dotted line). The statistical errors are large at this point (about 20% of the data have been analyzed) and it is not possible to see which one of the two sets is favored by the data. The predictions with the "natural" scale were not available at this moment, but a comparison with our data is anticipated in the future.

7.5 Conclusion

The E705 measurement of the pizero inclusive cross section appears to be in agreement with the previous measurements made by other experiments under similar conditions. The cross sections derived from the π^- and π^+ beams on the Li target were parametrized in terms of p_T and x_F . The ratio of the cross sections from the π^+Li and π^-Li interactions is in agreement with unity, which ensures the validity of the normalization scales and the understanding of the systematics of the experiment.

The Monte Carlo prediction of the single photon background, due to π^0 , η decays and hadronic interactions in the calorimeter, is smaller than the single photon signal measured from the data. The difference is attributed to the direct production of single photons. The systematic rise in the background-subtracted γ/π^0 ratio with increasing p_T is also observed and it is attributed to the photons being produced directly rather than as the result of parton fragmentation, as in the case of the pizero's. The fragmentation function smears the available p_T carried by the parton resulting in a lower p_T for the pizero.

The hadronic production of direct photons can be calculated, with several uncertainties within the framework of QCD, as was discussed in chapter 1. One of these uncertainties is the choice of the gluon structure functions. The E705 measurement of the direct photon inclusive cross section from π^- -Li interactions is compared in figure 7.11 to two theoretical predictions obtained by the "optimized" scale technique and corresponding to two sets of structure functions. The functions used in the two sets for the gluon content of protons and pions are of the form:

$$xG_{g/p}(x, Q_0=4 \text{ GeV}^2/c^2) \propto (1+9x)(1-x)^6$$

$$xG_{g/\pi}(x, Q_0=4 \text{ GeV}^2/c^2) \propto (1+6x)(1-x)^{3.11} \quad \text{for set 1 ("soft" gluon) and}$$

$$xG_{g/p}(x, Q_0=4 \text{ GeV}^2/c^2) \propto (1+9x)(1-x)^4$$

$$xG_{g/\pi}(x, Q_0=4 \text{ GeV}^2/c^2) \propto (1+6x)(1-x)^{2.89} \quad \text{for set 2 ("hard" gluon)}$$

The low statistics of the data that have been analyzed so far, does not allow us to distinguish with confidence between the two sets. However, the completed analysis should provide some better estimate for the gluon structure functions.

The high statistics that will be obtained from the π^+ data analysis will allow us to subtract the π^+ from the π^- direct photon cross section, in order to calculate the contribution of the annihilation process alone to the direct photon cross section.

Finally, when the theoretical predictions of the inclusive direct photon cross section with the "natural" scale technique are available, we will be able to do a comparison between the "natural" and "optimized" techniques.

TABLE 7-5 γ/π^0 ratio and direct photon invariant cross section for π^- Li.
The errors are statistical only.

p_T range (GeV/c)	$p_{T,aver}$ (GeV/c)	γ/π^0	$E d^3\sigma/dp^3$ (nb/GeV ² /nucleon)
4.00 - 4.25	4.11	0.10 ± 0.03	109.20 ± 38.23
4.25 - 4.50	4.36	0.13 ± 0.06	69.96 ± 32.30
4.50 - 4.75	4.61	0.16 ± 0.08	51.37 ± 25.68
4.75 - 5.00	4.86	0.18 ± 0.10	28.35 ± 15.75
5.00 - 5.50	5.20	0.20 ± 0.10	14.18 ± 7.09
5.50 - 6.50	5.83	0.27 ± 0.16	3.15 ± 1.87

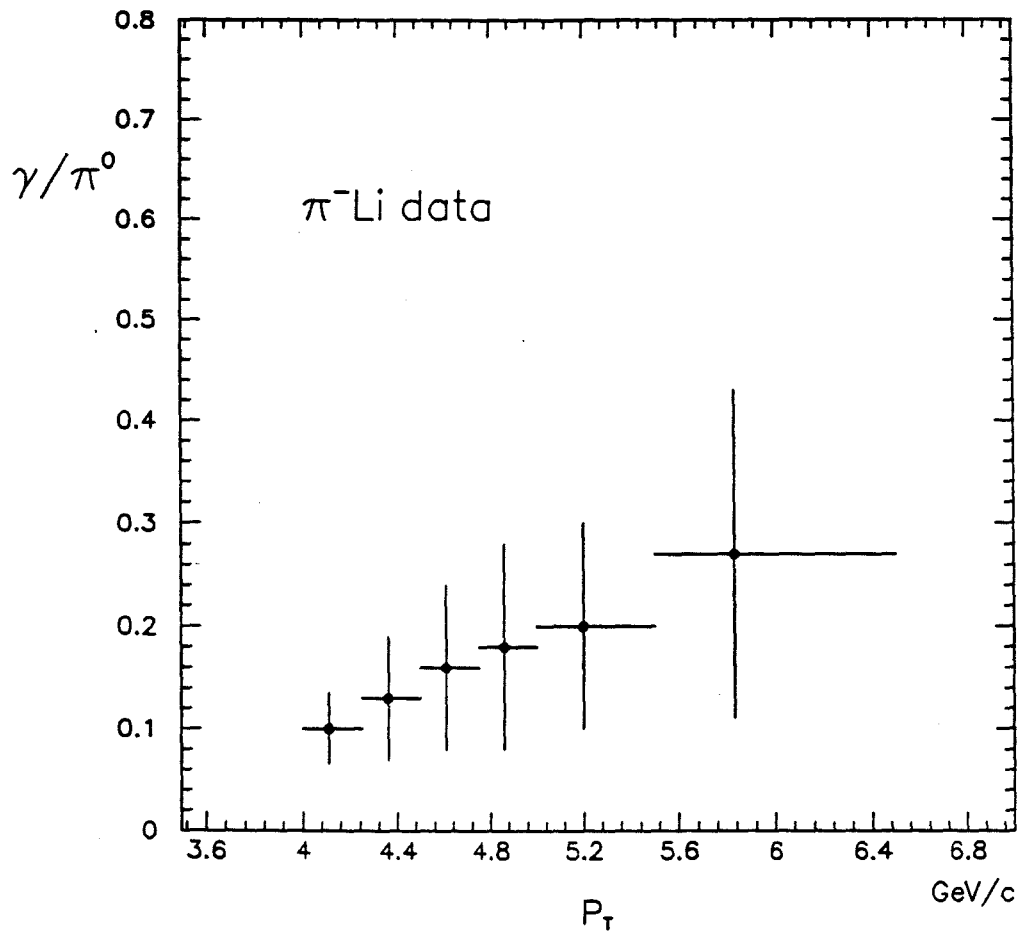


Figure 7.10 Production ratio of γ/π^0 for the π^-Li data as a function of p_T . The errors are statistical only.

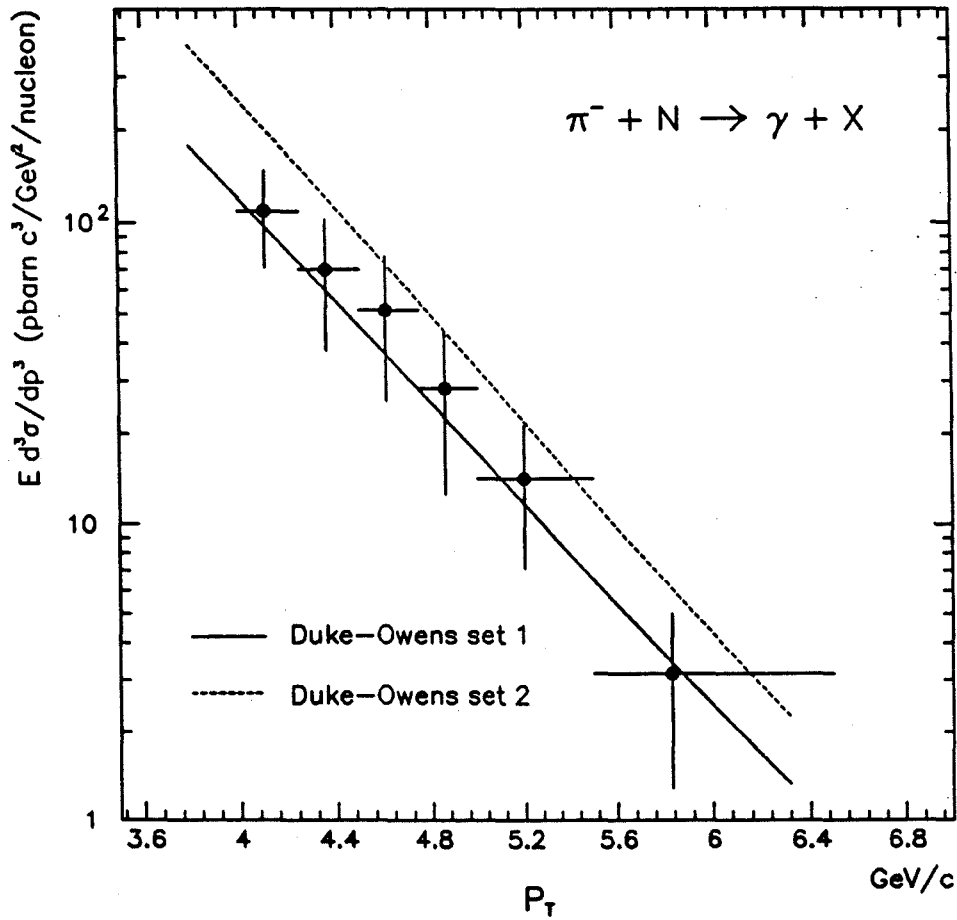


Figure 7.11 Direct photon inclusive invariant cross section for the π^- -Li data as a function of p_T averaged over x_F . The errors are statistical only. The solid and dotted lines are the QCD predictions with optimized scales and the Duke and Owens sets 1 and 2 structure functions respectively.

References

- 1 M.R.Pennington, "Cornerstones of QCD", Rep. Prog. Phys., 46 (1983) 393.
- 2 W.M.Geist et al., "Hadronic Production of Particles at Large Transverse Momentum: Its Relevance to Hadron Structure, Parton Fragmentation and Scattering", CERN/EP 89-159, Dec. 1989.
- 3 M.Gell-Mann, "A Schematic Model of Baryons and Mesons", Phys. Lett. 8 (1964) 214.
- 4 O.W.Greenberg, "Spin and Unitary-Spin Independence in a Paraquark Model of Baryons and Mesons", Phys. Rev. Lett., 13 (1964) 598.
- 5 M.Breidenbach et al., "Observed Behavior of Highly Inelastic Electron-Proton Scattering", Phys. Rev. Lett., 23 (1969) 935.
- 6 J.D.Bjorken, "Asymptotic Sum Rules at Infinite Momentum", Phys. Rev., 179 (1969) 1547.
- 7 R.P.Feynman, "Very High-Energy Collisions of Hadrons", Phys. Rev. Lett., 23 (1969) 1415.
- 8 H.Deden et al., "Experimental Study of Structure Functions and Sum Rules in Charge Changing Interactions of Neutrinos and Antineutrinos on Nucleons", Nucl. Phys., B85 (1975) 269.
- 9 J.F.Owens, "Large Momentum Transfer Production of Direct Photons, Jets, and Particles", Rev. Mod. Phys. 59 (1987) 465.
- 10 P.Aurenche et al., "Prompt Photon Production at Large p_T ", Nucl. Phys., B297 (1988) 661.
- 11 P.M.Stevenson, "Optimized Perturbation Theory", Phys. Rev., D23 (1981) 2916.

- 1 2 H.D.Politzer, "Stevenson's Optimized Perturbation Theory Applied to Factorization and Mass Scheme Dependence", Nucl. Phys., B194 (1982) 493.
- 1 3 P.M.Stevenson and H.D.Politzer, "Optimized Perturbation Theory Applied to Factorization Scheme Dependence", Nucl. Phys., B277 (1986) 758.
- 1 4 A.P.Contogouris et al., "Direct Photon by Positive and Negative Pion Beams", Phys.Rev., D32 (1985) 1134.
- 1 5 D.Atwood et al., "Conventional versus Optimization Procedures and Large- p_T Direct Photon Production", Proceedings of 11th Annual Montreal-Rochester-Syracuse-Toronto Meeting, Syracuse 1989.
- 1 6 P.Darriulat et al., "Large Transverse Momentum Photons from High-Energy Proton-Proton Collisions", Nucl. Phys., B110 (1976) 365.
- 1 7 E.Amaldi et al., "Search for Single Photon Direct Production in pp Collisions at $\sqrt{s}=53.2$ GeV", Phys. Lett., 77B (1978) 240.
- 1 8 T.Ferbel and W.R.Molzon, "Direct Photon Production in High Energy Collisions", Rev. of Mod. Phys., 56 (1984) 181.
- 1 9 L. Camilleri, 19th Symposium on Multiparticle Dynamics, Arles, France, June 1988, World Scientific Pub. Co.
- 2 0 M.Bonesini et al., "High Transverse Momentum Prompt Photon Production by π^- and π^+ on protons at 280 GeV/c", Z.Phys., C37 (1988) 535.
- 2 1 D.W.Duke, J.F.Owens, "Q²-dependent parametrizations of parton distribution functions", Phys. Rev., D30 (1984) 49; J.F.Owens, "Q²-dependent parametrizations of pion parton distribution functions", Phys. Rev., D30 (1984) 943.
- 2 2 J.Badier et al., "Direct Photon Production from Pions and Protons at 200 GeV", Z.Phys., C31 (1986) 341.
- 2 3 C.DeMarzo et al., "Measurement of Direct Photon Production at Large Transverse Momentum in π^-p , π^+p , and pp Collisions at 300 GeV/c", Phys. Rev., D36 (1987) 36.

- 24 A.Bernasconi et al., "Direct Photon Production in Proton-Antiproton Interactions at $\sqrt{s}=24.3$ GeV", Phys. Lett., B206 (1988) 163.
- 25 P.Gutierrez et al., "Inclusive Production of Pizero, Eta, and Direct Photons at Large p_T ", Proceedings of the XXVth Rencontres de Moriond, Les Arcs, Savoie, France, March 11-17 1990, ed. Frontieres.
- 26 S.Conetti et al., "Performance of 0.75-mm pitch MPWCs Operating at High Rate", IEEE Trans. on Nuclear Science, Vol.38, p.375, Feb.1990.
- 27 S.W.Delchamps et al., "Precision Charge Amplification and Digitization System for a Scintillating and Lead Glass Array", IEEE Trans. on Nuclear Science, Vol.38, p., Feb.1990.
- 28 L.Spiegel et al., "Performance of a Lead Radiator, Gas Tube Calorimeter", IEEE Trans. on Nuclear Science, Vol.38,p., Feb.1990.
- 29 C.M.Jenkins et al., "Results from the E-705 Electromagnetic Shower Position Detector", IEEE Trans. on Nuclear Science, Vol.38,p. ,Feb.1990.
- 30 S.Conetti et al., "A Smart Crate Controller for Fast CAMAC Data Acquisition", IEEE Transactions of Nuclear Science, NS-32 (1985) 1326.
- 31 A.Simard, "A measurement of the hadronic production of J/Ψ 's", March 1990, M.Sc. Thesis, McGill University.
- 32 H.Areti et al., "A Fast Processor for Dilepton Triggers", NIM, 212 (1983) 135-144.
- 33 L.Spiegel private communication.
- 34 G.Zioulas et al., "An Online Trigger Processor for Large Transverse Energy Events", IEEE Trans. on Nuclear Science, Vol.38,p.117, Feb.1990.
- 35 Electron Gamma Shower (EGS) is a Monte Carlo program that simulates the transport of the electrons and photons through matter in an arbitrary geometry. For more information see: W.Nelson et al, "The EGS4 Code System", SLAC-Report-265, Dec. 1985.

- 3 6 T.G.Turkington, "Precise Measurement of Photons from the Interactions of 300 GeV/c Hadrons on a Lithium Target", 1989, Ph.D. Thesis, Duke University.
- 3 7 C.Fabjan, "Calorimetry in High Energy Physics", Techniques and Concepts of High Energy Physics-III, T.Ferbel, ed. Plenum Pub. Corp., 1985.
- 3 8 D.E.Wagoner et al., "A measurement of the energy resolution and related properties of an SCG1-C scintillation glass shower counter array for 1-25 GeV positrons", NIM, A238 (1985) 315-320.
- 3 9 J.E.Brau et al., "The Lead Glass Columns: A Large Shower Detector at the SLAC Hybrid Facility", NIM, 196 (1982) 403-413.
- 4 0 J.A.Appel et al., "Performance of a Lead-Glass Electromagnetic Shower Detector at Fermilab", NIM, 127 (1975) 495-505.
- 4 1 The word electrons is used here meaning both electrons and positrons to avoid repetition.
- 4 2 Advanced Computer Program (ACP) is a system of CPU modules for data crunching. For more information see: T.Nash et al, "A Site Oriented Supercomputer for Theoretical Physics: The Fermilab Advanced Computer Program Multi Array Processor System (ACPMAPS)", FERMILAB-Conf-89/58 (1989).
- 4 3 B.Cox et al., "A Measurement of the Response of an SCG1-C Scintillation Array to 4-14 GeV/c Pions", NIM, A238 (1985) 321-327.
- 4 4 H.Bengtsson and T.Sjostrand, "The Lund Monte Carlo for Hadronic Processes: PYTHIA Version 4.8", Comput.Phys.Commun., 46 (1987) 43.
- 4 5 A.S.Carroll et al., "Absorption Cross Sections of π^\pm , K^\pm , p and \bar{p} on Nuclei Between 60 and 280 GeV/c", Physics Letters, 80B (1979) 319.
- 4 6 T.J.Roberts et al., "Neutron-Nucleus Inelastic cross sections from 160 to 375 GeV/c", Nuclear Physics, B159 (1979) 56-66.
- 4 7 Particle Data Group, "Review of Particle Properties", Physics Letters, 204B (1988) 1.

- 4 8 M.Bonesini et al., "High Transverse Momentum η Production in π^-p , π^+p , and pp Interactions at 280 GeV/c", CERN-EP/88-178, Dec. 1988.
- 4 9 J.Badier et al., "Inclusive High p_T π^0 Production from π^\pm and Protons at 200 GeV/c", Z. Phys., C30 (1986) 45-50.
- 5 0 J.Povlis et al., "Nuclear Enhancement of π^0 and η Mesons Produced at Large Transverse Momenta", Phys. Rev. Lett., 51 (1983) 967.
- 5 1 C.DeMarzo et al., "Measurement of π^0 Production at Large Transverse Momentum in π^-p , π^+p and pp Collisions at 300 GeV/c", Phys.Rev., D36 (1987) 16.
- 5 2 M.Bonesini et al., "High Transverse Momentum π^0 Production by π^- and π^+ on protons at 280 GeV/c", Z. Phys., C37 (1987) 39.